FHWA-NJ-2025-006

Innovative Pothole Repair Materials and Techniques Phase II – Concrete Crack Repair, Ultrasonic Testing, and Automated Repair and Inspection

Final Report
December 2025

Submitted by

Hao Wang, PhD
Professor of Engineering

Husam Najm, PhD
Professor of Engineering

Perumalsamy Balaguru, PhD
Distinguished Professor of Engineering

Alissa Persad
Graduate Student

Jay Shah and Tianjie Zhang
Postdoctoral Associate

Xiao Chen and Xiaoyu Zhang
Graduate Student

Center for Advanced Infrastructure and Transportation (CAIT)
Rutgers, the State University of New Jersey
100 Brett Road, Piscataway, NJ 08854

NJDOT Research Project Manager
Giri Venkiteela

In cooperation with

New Jersey
Department of Transportation
Bureau of Research
And
U. S. Department of Transportation
Federal Highway Administration

DISCLAIMER STATEMENT

TECHNICAL REPORT DOCUMENTATION PAGE

1. Report No. FHWA NJ-2025-006	**2. Government Accession No.**	**3. Recipient's Catalog No.**

4. Title and Subtitle Innovative Pothole Repair Materials and Techniques, Phase II - Concrete Crack Repair, Ultrasonic Testing, and Automated Repair and Inspection	**5. Report Date** December 2025 **6. Performing Organization Code**
7. Author(s) Hao Wang, Husam Najm, Bala Balaguru, Alissa Persad, Jay Shah, Tianjie Zhang, Xiao Chen, and Xiaoyu Zhang	**8. Performing Organization Report No.**
9. Performing Organization Name and Address Center for Advanced Infrastructure and Transportation Rutgers, The State University of New Jersey 100 Brett Road Piscataway, NJ 08854	**10. Work Unit No.** **11. Contract or Grant No.** NJDOT Task Oder 408
12. Sponsoring Agency Name and Address Federal Highway Administration (SPR) 1200 New Jersey Avenue, SE Washington, DC 20590 New Jersey Department of Transportation (SPR) 1035 Parkway Avenue, P.O. Box 600 Trenton, NJ 08625.0600	**13. Type of Report and Period Covered** Final Report, 11/1/2023 – 11/1/2025 **14. Sponsoring Agency Code** FHWA, NJDOT

15. Supplementary Notes

Conducted in cooperation with the U.S. Department of Transportation, Federal Highway Administration.

16. Abstract

Extending the life span of concrete pavements and bridge decks can save costs and significantly reduce interruptions to traffic. This research focused on enhancing the filler material as well as exploring effective injection methods to save time and reduce traffic disruption. The repair formulations were evaluated based on two main criteria: workability and injection into the crack using appropriate delivery method. Three formulations were selected. Formulation A mixes have Portland cement, Micro fly ash, very fine sand (No.100), and superplasticizer. Formulation B mixes use CTS Cement All and Quikrete Fastset Cement component available in the NJDOT QPL list with added polymer and superplasticizer. Formulation C mixes are GeoPolymer based mixes and include metakaolin, micro fly ash, zirconium sand, iron oxide and superplasticizer. These formulations were tailored for different crack widths and geometries. This research investigated ultrasonic testing (UT) based non-destructive methods for crack characterization and repair evaluation. Laboratory tests were conducted on brick specimens to establish the initial properties of ultrasonic signals. Further tests were conducted on concrete beams after fatigue loading and reinforced concrete slabs with varying crack profiles. An UT methodology was developed that relied on general pristine behavior of concrete rather than point specific pristine profiles. Crack depth evaluation was conducted by comparing time of arrival. The signals from the cracked state were used as the reference and the shifts in time of arrival towards the pristine trend, along with amplitude gain relative to the cracked state, were used to assess repair quality. In addition, the feasibility of automated inspection and repair of potholes are investigated. By integrating high-resolution laser scanning with SLA-based 3D printing, customized patch geometries were successfully generated from artificial pothole models. A low-cost 3D image scanning system was developed for pavement pothole inspection. Laboratory experiments were conducted on artificially created potholes with different depths, areas, and surface roughness levels. Validation through benchmarking against a high-precision laser scanner demonstrated that the system achieves comparable geometric accuracy.

17. Key Words crack repair, injection, macro cracks, micro cracks, inorganic	**18. Distribution Statement** No restrictions.

19. Security Classif. (of this report) Unclassified	**20. Security Classif. (of this page)** Unclassified	**21. No. of Pages** 126	**22. Price**

Form DOT F 1700.7 (8-72) Reproduction of completed page authorized

ACKNOWLEDGEMENTS

This project was sponsored by the New Jersey Department of Transportation (NJDOT) and the Federal Highway Administration. The authors acknowledge the guidance provided by the Research Project Manager, Dr. Giri Venkiteela, and the project panel members: Yong Zeng, Emanuel Bassey, Sadime Absolam, Nicholas Colangelo, Jeff Evanylo, Roger Estivalletti, and Dale Deluca from NJDOT. The authors also acknowledge Derek Shum, Nicholas Moscarella, Samuel Guimarello, Eugene Yu, Alexander Stefaniak, and Jordan Jules from Rutgers University for their help and assistance working on this project.

TABLE OF CONTENTS

LIST OF FIGURES.. iv

LIST OF TABLES ix

EXECUTIVE SUMMARY 1

BACKGROUND 3

OBJECTIVES 5

LITERATURE REVIEW ON CONCRETE CRACK REPAIR 6

- Concrete Repair Methods 6
- Crack Characterization and Repair 18

LABORATORY TESTING OF CONCRETE CRACK REPAIR 25

- Crack Repair Formulations 25
- Injection Procedures 31
- Pull Off Tests 34
- Conclusions and Recommendations 36

LITERATURE REVIEW ON ULTRASONIC TESTING OF CONCRETE 38

- Fundamentals of Wave Propagation Techniques 38
- Vertical Crack Imaging 48

ULTRASONIC TESTING ON CONCRETE CRACK AND REPAIR 53

- Laboratory Experiment Setup and Specimen 53
- Laboratory Experiment Results 53
- Field Testing of Concrete Slabs 66
- Field Ultrasonic Testing Results 68
- Schmidt Hammer Tests 88
- Conclusions and Recommendations 93

FEASIBILITY OF AUTOMATED REPAIR AND INSPECTION OF POTHOLE 96

- Introduction 96
- Literature Review on 3D Printing for Pavement Crack and Pothole Repair 97
- Literature Review on 3D Scanning of Pothole 101
- Experimental Trials on Pothole Repair with 3D Printing 102
- Low-Cost Imaging Scanning of Pothole Specimens 109
- Conclusions and Recommendations 119

REFERENCES 122

LIST OF FIGURES

Figure 1. Typical operations of the crack repair process: a) blowing surface with air,

b) sand blasting, c) shot blasting, d) bottle application, e) caulk gun application, f) pump injection, g) flood application, h) sand casting on surface (3).

Figure 2. Core showing crack depth (left) and petrographic scan showing penetration of crack sealant (right) (3).

Figure 3. Key elements of a concrete deck crack (1)

Figure 4. Vacuum assisted injection for barrier (14) https://www.tecvacinc.net/untitled-sitepage_9)

Figure 5. Vacuum assisted injection for wall 14) (https://www.tecvacinc.net/untitled-sitepage_9)

Figure 6. Vacuum assisted grout injection for a concrete deck (15) https://www.balfourbeatty.com/what-we-do/expertise/specialist-services/specialist-structural-repair-and-maintenance/

Figure 7. Mix A1 just before pouring it into injection tube.

Figure 8. MixA1 being poured into thin plates for flexural testing

Figure 9. Artificial 1/8 in and 1/4 in cracks cut into concrete blocks

Figure 10. Slices cut from the injected concrete block with 1/8 in crack width

Figure 11. Mix B1-RS after mixing and being poured into plastic mold

Figure 12. Coating of a 4 in x 2 in concrete surface using Mix 9 of Formulation C

Figure 13. Concrete crack 14 in long, 2mm wide, and 2 in deep created in the lab

Figure 14. Battery-powered caulk gun

Figure 15. Vertical injection of 14 mm long crack with a crack width of 3mm

Figure 16. Vertical injection of half-concrete cylinder with irregular surface

Figure 17 Pull-off PosiTest® AT-M Manual Adhesion Tester

Figure 18. Half cylinder specimen with 20 mm cores (left), 20 mm glued dollies (right)

Figure 19. Pull-off completed tests (left), 20 mmm dollies after pull-out tests (right)

Figure 20. (a) Different configurations for sensor placement (T: Transmitter; R: Receiver) and (b) Direct wave transmission showing restoration of signal amplitude when the crack is healed [14]

Figure 21. (a) Typical ToF approach using indirect wave transmission and (b) BS: 1881 method

Figure 22. (a) Multiple transducer configuration and (b) transducer configuration when the crack is near the edge

Figure 23. (a) Transmission of surface wave across the crack and (b) shift in the cut-off frequency of the spectral ratio (solid/dashed curve – experimental/numerical results)

Figure 24. (a) Dependency of transmission function shape on frequency, (b) signal consistency variation of transmission function in undamaged case, (c) finalized integral limits based on signal consistency index, and (d) Correlation between spectral energy ratio and crack depth

Figure 25. Energy diffusion profile in concrete for excitation of (a) 300 kHz and (b) 500 kHz signal

Figure 26. (a, b) Concept figures showing the effect of crack on the wave propagation and transmitted signal in (c) undamaged specimen and (d) cracked specimen

Figure 27. (a) The concept of identifying ATME and (b) The variation of ATME with crack notched and cracked samples

Figure 28. (a) Experimental high frequency (HF) and low frequency (LF) signals, (b) ATME and LF amplitude variation, and change in Δt for (c) no crack and (d) 5.5 cm crack

Figure 29. (a) Schematic showing the imaging concept in 2-D, and (b) sectional image highlighting the crack depth (darker region)

Figure 30. Crack tip imaging using (a) SAFT and (b) TRFT method.

Figure 31. (a) Schematic showing the half-skip time focused method and (b) ellipse profiles showing scattering ‘p’ at its interaction, and (c) image showing the extent of the crack.

Figure 32. (a) Cross section divide into meshes and (b) SIBIE map for vertical crack.

Figure 33. Experimental setup

Figure 34. (a) Pristine specimen, and (b) cracked specimen

Figure 35. Transmitted signals relative to the signal transmission in the specimen obtained with (a) 70 kHz and (b) 140 kHz signals, and their corresponding shift in the time of arrival of their first peaks at (c) 70 kHz and (d) 140 kHz inspection

Figure 36: Repaired specimen

Figure 37. Transmitted signal in the repaired specimen relative to its pristine state for (a) 70 kHz (b)140 kHz inspection, and time of arrival of (c) 70 kHz signal and (d) 140 kHz signal

Figure 38. dB drop trend across different crack depths obtained using (above) 70 kHz and (below) 140 kHz signals

Figure 39. Recovery trend in dB loss across different crack depths obtained using (a) 70 kHz and (b) 140 kHz signals

Figure 40. Correlation coefficient of specimen with 1.5 in. deep crack obtained using (a) 70 kHz and (b) 140 kHz signals

Figure 41. Correlation coefficients before and after crack repair for (a, b) a 1 in. crack and (c, d) a 0.5 in. crack using different frequencies

Figure 42. Crack repair process

Figure 43. Gradual change in the amplitude recovery of the signal transmission across different time windows using a 70 kHz signal

Figure 44. Gradual change in the amplitude recovery of the signal transmission across different time windows using a 140 kHz signal

Figure 45. Trend of correlation coefficient change across different time windows for the 70 kHz signal

Figure 46. Trend of correlation coefficient change across different time windows for the 140 kHz signal

Figure 47. Partial crack filling procedure

Figure 48. Signal strength recovery for a partially filled crack obtained using (a) 70 kHz and (b) 140 kHz signals

Figure 49. Variability of the pristine signal shape for a 70 kHz signal across different specimens

Figure 50. (a) Schematic for the concrete specimen, (b) wooden mold for pouring the concrete, and (c) final form of the concrete slab

Figure 51. (a) Three-point bending test setup, and (b) generated crack reaching up to a minimum depth of the rebar

Figure 52. Schematic of ultrasonic testing configuration for (a) concrete slab, (b) concrete beam, and (c) the ultrasonic testing setup

Figure 53. Signal transmission trend for 2" transmission distance

Figure 54. Signal transmission trend for different specimens at 4" transducer separation

Figure 55. Signal transmission trend for different specimens at 6" transducer separation

Figure 56. Signal transmission trend for different specimens at 6" transducer separation

Figure 57. Trends of amplitudes across three different rows in pristine conditions for different transmitter-receiver separations

Figure 58. Crack size measurements on the top and the side surface of concrete beams

Figure 59. Signal transmission across (a) Beam 1, (b) Beam 2, and (c) Beam 3 in their pristine and cracked state

Figure 60. Time of arrival trend with different crack depths for a straight crack

Figure 61. Time of arrival trend with different crack depths for a 30° inclined crack

Figure 62. Variation in the average time of arrival with crack depth for both the straight and inclined cracks

Figure 63. Time of arrival trend obtained at different time intervals post-repair of the straight crack regions with crack depth of (a) 0.5", (b) 1", (c) 1.5", and (d) 2"

Figure 64. Time of arrival trend obtained at different time intervals post-repair of the inclined crack regions with crack depth of (a) 0.5", (b) 1", (c) 1.5", and (d) 2"

Figure 65. Transmitted signal amplitudes obtained at different time intervals post-repair of straight crack regions with crack depth of (a) 0.5", (b) 1", (c) 1.5", and (d) 2"

Figure 66. Trend of transmitted signal amplitude obtained at different time intervals post-repair of the inclined crack regions with crack depth of (a) 0.5", (b) 1", (c) 1.5", and (d) 2"

Figure 67. Time of arrival of the surface wave for the crack touching the rebar

Figure 68. Changes in the (a) time of arrival (not normalized to the same scale) and (b) signal amplitude (normalized to the same scale) of the transmitted signal for a repaired crack extending up to the rebar depth

Figure 69. Correlate the RN number generated from the hammer test to a specific compressive strength for normal concrete.

Figure 70. Crack locations in concrete slab specimens and the location of sound concrete where baseline readings were taken

Figure 71. Markings showing locations where readings were taken for each crack.

Figure 72. Automated 3D printing system without detection system

Figure 73. Automated pavement crack sealing system based on 2D image

Figure 74. Automated pavement crack sealing system based on laser scanning

Figure 75. Movable 3D printing robot

Figure 76. Asphalt 3D printer

Figure 77. UAV equipped with 3D asphalt printing device

Figure 78. In-situ concrete pothole repair

Figure 79. Artificial concrete potholes

Figure 80. Laser scanner

Figure 81. 3D model of: (a) Shallow pothole, (b) Deep pothole

Figure 82. 3D-printed frame for shallow artificial pothole: (a) inner surface, (b) outer surface

Figure 83. Fitting conditions of the frame: (a) for shallow pothole, (b) for deep pothole

Figure 84. Artificial potholes after grinding: (a) shallow pothole, (b) deep pothole

Figure 85. Scanned model of artificial potholes after grinding: (a) shallow pothole, (b) deep pothole

Figure 86. 3D-printed solid patching material: (a) for shallow pothole, (b) for deep pothole

Figure 87. Fitting conditions of solid patching materials: (a) for shallow pothole, (b) for deep pothole

Figure 88. Comparison of scanned models between 3D printed materials and potholes: (a) for shallow pothole, (b) for deep pothole

Figure 89. Triangulation principle between 2 cameras and the 3D world

Figure 90. Chessboard images from different angles

Figure 91. 3-camera system and remote control

Figure 92. Image processing results

Figure 93. Corresponding points of two stereo pairs

Figure 94. 3D point cloud of the pothole

Figure 95. The outliers to be removed

Figure 96. The flattened pothole region

Figure 97. The pothole region surface and top plane

Figure 98. SimScan42 and the scan result for the same pothole

LIST OF TABLES

Table 1 Simplified table of the Florida DOT crack disposition tables in Section 400 of FDOT Specifications (5)

Table 2 Use of four (4) sealant types in various states (6)

Table 3 Crack sealing criteria based on crack width from several DOT's (6)

Table 4 Number of times in which each of the listed crack repair option was considered in deciding on cracking repair from responding State DOT's (1)

Table 5 Number of times in which each of the listed crack repair method and material was considered in deciding on cracking repair from responding State DOT's

Table 6 Summary of decision matrix for crack remediation options for different crack width and crack density combinations at bridge deck age between 0 and 2 years (1)

Table 7 Summary of decision matrix for crack remediation options for different crack width and crack density combinations at bridge deck age of 5 years (1)

Table 8 Summary of decision matrix for crack remediation options for different crack width and crack density combinations at bridge deck age of 10 years (1)

Table 9 Crack widths for epoxy injection (10)

Table 10 Crack sealing criteria based on crack width from several DOT's (6)

Table 11 Crack width range for Do-Nothing Action (10)

Table 12 Classification of cracks 'Insignificant', 'Moderate', and 'Wide' (11)

Table 13 NJTP Concrete cracking, definitions, and recommendations (12)

Table 14 Various trial mixes for Formulation A

Table 15 Materials used in formulations with composition and particle size

Table 16 Workability observations for Formulation A

Table 17 Trial mixes for Formulation B

Table 18 Workability observations and setting times for Mixes B

Table 19 Trail Mixes for Formulation C (Geopolymer-based mixes)

Table 20 Poll-off test results for different formulations

Table 21 Measured RN numbers and the corresponding compressive strength

Table 22 Measured RN numbers and the corresponding compressive strength for vertical crack location

Table 23 Measured RN numbers and the corresponding compressive strength for inclined crack location

Table 24 Statistics comparison of scanned models between 3D printed materials and potholes

Table 25 Camera Parameters

Table 26 Comparison of Proposed System vs. Ground Truth

EXECUTIVE SUMMARY

Concrete decks mainly develop surface cracks due to demanding operational and environmental loads. These defects compromise structural integrity and expose internal elements such as reinforcing bars in reinforced concrete to degrading environments. Timely evaluation and repair of such defects are critical to achieving the intended service life of the infrastructure. There are several crack repair methods currently used by State DOT's including: gravity polymer crack chasing, pressure-injected epoxies, flood coating or 'healer-sealer' of the deck, and thin polymer overlays, latex-modified concrete (LMC), and ultra-thin high-performance concrete (UHPC). Proper formulations, surface preparation, and the compatibility between repair material and the substrate including modulus of elasticity, are critical for long-lasting repair. Review of crack repair methods, repair materials and repair specs shows that crack repair is a major issue for state DOT's and other agencies. Few studies have addressed this issue and made recommendations based on lab testing and field data. Other studies focused on how cracks are repaired and how maintenance strategies are selected. Decision making and guidance on crack repair methods, frequency, and materials varied significantly among various agencies.

This research focused on enhancing crack filler material, where they can be applied, when they should be applied as well as exploring effective injection methods to save time and reduce traffic disruption. The repair formulations were evaluated based on two main criteria: workability and injection into the crack using appropriate delivery method. Three formulations were selected. Formulation A mixes have Portland cement, Micro fly ash, very fine sand (No.100), and superplasticizer. Formulation B mixes use CTS Cement All and Quikrete Fastset Cement component available in the NJDOT QPL list with added polymer and superplasticizer. Formulation C mixes are GeoPolymer based mixes and include metakaolin, micro fly ash, zirconium sand, iron oxide and superplasticizer. These formulations were tailored for different crack widths and geometries. Formulation A was effective for crack widths of 1/4 in (6 mm) and 1/8 in (3 mm). Formulations B1 and B2 were effective in filling 1/8 in (3 mm) and 3/16 in (2 mm) cracks. Formulation C can be applied as coating to micro and nano cracks. Formulations A and B were easy to inject all the way into 1 in deep cracks up to 9 in. vertically and they bonded well with the substrate. Microscope images of Formulation C coatings showed no cracks in the coating after 3 months. Mechanical injections using cordless caulk guns were very effective in injecting 1/8 in and 1/4 in cracks vertically up to 9 in. All three formulations can also adapt to gravity injection or coating with sufficient impregnation to seal ultra-thin cracks.

Non-invasive methods are imperative for successful characterization of cracks in concrete. This research investigated ultrasonic testing (UT) based non-destructive methods for crack characterization and repair evaluation. Laboratory tests were conducted on brick specimens to establish the initial properties of ultrasonic signals. A consistent delay in signal arrival, amplitude decay and poor similarity relative to the pristine signal was observed with increasing crack size. Upon crack repair, a gradual recovery in signal amplitude was noted, approaching the original pristine state. Further tests were conducted on concrete beams after fatigue loading and reinforced concrete slabs with varying crack profiles. In summary, an ultrasonic testing methodology was developed that relied on the general pristine behaviour of concrete rather than point specific pristine profiles. Crack depth evaluation was conducted by comparing time of arrival. The signals from the cracked state were used as the reference and the shifts in time of arrival towards the pristine trend, along with amplitude gain relative to the cracked state, were used to assess repair quality. The identified strategy proved to be highly adaptable to field conditions and offered time efficient ultrasonic testing results. Despite advantages, it remains crucial to establish reliable UT methods in field condition.

In addition, the feasibility of automated inspection and repair of potholes are investigated. By integrating high-resolution laser scanning with SLA (Stereolithography) based 3D printing, customized patch geometries were successfully generated from artificial pothole models. Surface grinding was found to improve geometric compatibility, yet its applicability in real-world practice requires careful evaluation due to additional time and labour. Several technical and practical barriers were discussed, including scanning efficiency under various environments, the influence of complex surface geometries, and mechanical performance of printable materials and potential mismatch from pothole evolution over time. In addition, this study presents a low-cost 3D image scanning system for pavement pothole inspection. It utilizes a three-GoPro camera configuration to provide enhanced stability and broad view for mobile data acquisition. To thoroughly test the system accuracy and its ability to handle various conditions of pavement surface damage, laboratory experiments were conducted on artificially created potholes with different depths, areas, and surface roughness levels. Validation through benchmarking against a high-precision laser scanner demonstrated that the system achieves comparable geometric accuracy while offering significant advantages in speed, real-time application capabilities, and cost-effectiveness.

BACKGROUND

Extending the life span of concrete bridge decks and pavements can save costs and significantly reduce lane closures and interruptions to traffic. Bridge engineers and contractors design and build bridge decks to last for many years with minimum maintenance. However, cracks in concrete bridge decks can form and as these cracks increase and become wider, further deterioration occurs leading to needed maintenance and repairs. Concrete decks and pavements mainly develop surface cracks due to demanding operational and environmental loads. These defects compromise structural integrity and expose internal elements such as reinforcing bars in reinforced concrete to degrading environments. Timely evaluation and repair of such defects are critical to achieving the intended service life of the infrastructure.

Bridge deck preservation is to do long lasting repair of cracks and/or applying an overlay over the deck. There are several crack repair methods, deck sealing, and deck overlay applications currently used by State DOT's. These include gravity polymer crack chasing, pressure-injected epoxies, flood coating or 'healer-sealer' of the deck, thin polymer overlays, hot-mixed asphalt with waterproofing membrane, latex-modified concrete (LMC), and ultra-thin high-performance concrete (UHPC).

Given the wide variety of crack repair materials and deck overlays and the application methods, there is to systematically evaluate these repair materials and application techniques. An automated repair process can save time and reduce disruption to traffic. In addition to the proper surface preparation and the needed flow for the material, the compatibility properties between repair material and concrete including modulus of elasticity, shrinkage, and preparation methods are critical for long-lasting repair.

Crack repair of concrete structures is an integral part of maintenance of transportation infrastructures. NJDOT has established procedures and methods for repairs. However, there is always room for improvement of the type of repair and protective material as well as the repair techniques. Using the best technique at the appropriate time for treatment and accelerating the process, and with the compatible materials, the preservation and repair practices will provide an effective solution that will extend the service life of bridge decks and make them safer, less costly, and reduced disruption to traffic.

Evaluation of crack depth and repair using non-destructive testing (NDT) can provide valuable information for bridge deck maintenance. The information of crack depth is important for selection of repair material or method. On the other hand, the quality of crack repairs needs to be assessed, and quality control of repair is required in the field. Challenges emerge when evaluating the efficacy of crack repair methods, particularly for deeper crack as common assessments are often limited by surface inspections. This necessitates development of non-destructive methodologies capable of accurately determining the quality of crack repair. The application of NDT to monitor crack repair will contribute to advancing the understanding of the interaction between crack filler material and base structure, leading to the development of more efficient and durable repair materials techniques.

Among current non-destructive testing methods, ultrasonic testing is a highly sought after technique due to its versatile application to both concrete and steel structures. However, the effectiveness of ultrasonic testing is often dependent on comparisons with a pristine baseline of the structure, which is typically not available in field conditions. It is needed to develop a practical methodology for field application of ultrasonic testing in assessing cracks and evaluating the quality of crack repair in reinforced concrete structures.

OBJECTIVES

The first objective of this research is to enhance the crack repair process of concrete structural members to extend their service life by focusing on three major components: 1) innovative inorganic formulations that achieve repair compatibility and longevity for macro and micro-cracks, 2) effective placement and injection methods, and 3) quality assurance focusing on repair integrity and durability.

The second objective is to investigate the feasibility of using ultrasonic testing to evaluate concrete crack depth and repair quality. The effects of signal frequency, crack depth, and steel rebar on testing results are investigated based on laboratory specimens and reinforced concrete slabs.

The third objective is to investigate the feasibility and challenges of applying additive manufacturing, particularly 3D printing, to pothole repair in concrete pavements. Along with this objective, a low-cost, vehicle-mountable 3D scanning system is developed for rapid 3D reconstruction and quantification of potholes.

LITERATURE REVIEW ON CONCRETE CRACK REPAIR

The literature review of crack repair methods, repair materials and repair specs shows that crack repair is a major issue for state DOT's and other agencies. Several research studies have addressed this issue and made recommendations based on lab testing, field testing and survey data, service life modeling, and life cycle cost analysis. Other studies focused on how cracks are repaired and how maintenance strategies are selected. Decision making and guidance on crack repair methods, frequency, and materials varied significantly among various agencies. Survey data from these studies showed some states do not address crack maintenance in their manuals. Others provide limited guidance in their specifications. Very few states provide comprehensive guidance for repairing cracks. The literature review also showed variation in DOT specifications on materials and methods. The study by WJE (1) provided decision making matrices for crack repair and repair materials service life models based on crack width crack density, and age of deck. Another study (2) investigated the performance of various crack sealers in the field and provided recommendations for MnDOT for their crack repair program. However, the literature review showed that there is a lack of data from field evaluation on the quality of the repair, its longevity, bond strength, and the effects of freeze-thaw and chlorides on repaired cracks. There is also a need to better understand the performance of the repair materials and when and where they should be applied. Some materials have good bond strength but have high viscosity making them unsuitable for narrow cracks such as epoxy sealers. While MMA, HMWM, and Polyurethanes have very low viscosity making them more suitable for narrow crack but do not have high bond strength. Research on effective repair materials is also lacking. There is a lack of data on multiple repairs and correlation between lab data and filed data.

Concrete Repair Methods

Bridge engineers and contractors design and build bridge decks to last for many years with minimum maintenance. However, cracks in bridge decks can form and as these cracks increase and become wider, further deterioration occurs leading to needed maintenance and repairs. Cracks can also develop in substructure elements such as abutment walls, retaining walls, columns, bent caps, as well as exposed pile caps. There are many factors that can cause cracking of concrete. These factors include: plastic shrinkage cracking; drying shrinkage; thermal stresses; chemical reaction; weathering; corrosion of reinforcement; poor construction practices; construction overloads; settlement cracking; errors in design and detailing; and externally applied loads (www.concrete.org/topicsinconcrete) (2).

There are several crack repair methods, deck sealing, and deck overlays applications currently used by State DOT's to repair bridge deck cracks. They include: gravity polymer crack chasing, pressure-injected epoxies, flood coating or 'healer-sealer', penetrating sealers thin polymer overlays, hot-mixed asphalt with water proofing membrane, latex modified concrete (LMC), and ultra-high performance concrete (UHPC). Many DOT's, government, state, and federal agencies, researchers and suppliers conducted studies that addressed cracking in concrete and crack repairing techniques. The following literature review summarizes some of these studies.

A study by Braun Intertec Corp. for MnDOT (3) evaluated the field performance of twelve (12) crack sealant products. Fig. 1 shows the typical operations of the crack repair process from the study. Their field observations showed highly variable depth of sealant penetration and was likely is dependent on the presence of debris within the crack, filler material used, crack width and depth, and the deck temperatures during application. They observed that the detachment from the crack face to be the predominant failure mode. Their investigation reinforces the need for highly flowable filler material and good adhesion.

Visual observations crack monitoring, in addition to petrographic examination and coring in evaluating the sealer performance (3). Visual observations were performed each spring over a three year period. After one winter, 15 of the 24 test locations were documented as effectively sealed. After 3 winters, 18 of the 24 locations were documented as ineffectively sealed. Results from their coring after the second winter showed that the observed depth of penetration was highly variable and is likely dependent on the original crack width and the deck temperatures during application. The primary influence on the depth of penetration was the presence of debris; every cored crack was filled with debris from the top (bridge surface) to the base of the core, regardless of surface preparation. Figure 2 shows the depth of sealant penetration from the study.

Figure 1. Typical operations of the crack repair process: a) blowing surface with air, b) sand blasting, c) shot blasting, d) bottle application, e) caulk gun application, f) pump injection, g) flood application, h) sand casting on surface [(3)]

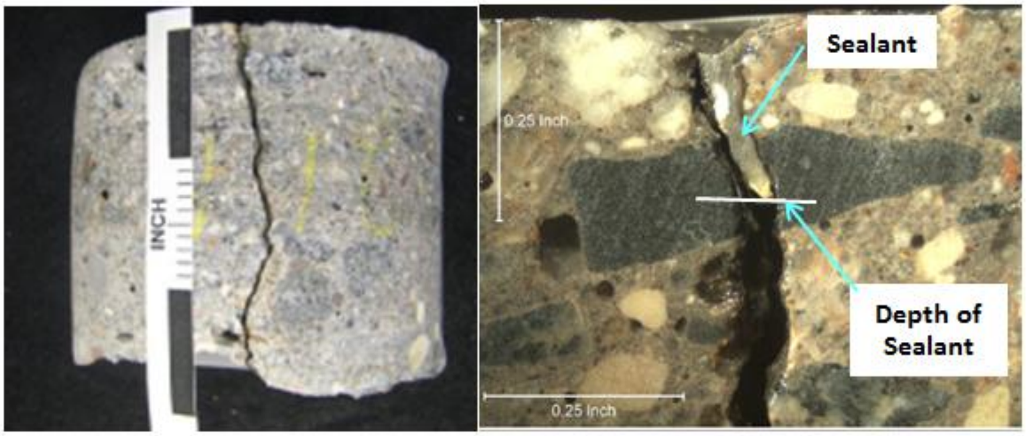

Figure 2. Core showing crack depth (left) and petrographic scan showing penetration of crack sealant (right) (3)

According to Oman (3), most products appeared to reduce permeability after one winter, except for Accuflex Gel-Seal. This product is unique to the experiment as it was the only product that is neither an epoxy nor methacrylate resin. The field review after three winters was that the crack repair performance was drastically reduced across the board from the previous field evaluation. The major differences observed during this review were major loss of sealant and sand materials. After three winters, no product was performing at a fully acceptable level. Among other findings from this study, MMA and HMWM sealers achieved deeper penetration than epoxy crack sealers. One epoxy achieved a similar depth of penetration (about 0.3 in) but has a low viscosity similar to that of methacrylate (MMA) and high molecular weight methacrylate (HMWM) sealers. No particular material property appears to be an indicator of field performance.

Four epoxy sealant products and three MMA/HMWM sealant products were recommended for consideration on MnDOT's Approved Products Lists for crack sealants. Each product recommendation contains the surface preparation and application method conditions under which they were applied. Based on visual observation and performance of products after three (and even two winters), they recommended that MnDOT looks into increasing the frequency of its routine crack sealing program from the current five-year cycle. If an increase in internal resources or funding is not available and a three-year cycle is not feasible, perhaps bridge candidates for sealing could be identified and prioritized by structure type, age, condition, and/or other factors (2).

The Florida Department of Transportation (FDOT)((4) published comprehensive crack dispositions tables for deck cracks and non-deck cracks that includes recommendations of repair methods and repair material based on crack width and crack density. Rettner et al. (5) produced a simplified table of the Florida DOT disposition crack tables as shown in Table 1. The Florida DOT specs for crack repairs were found to be the most comprehensive specs available. (1)

Table 1 Simplified table of the Florida DOT crack disposition tables in Section 400 of FDOT Specifications (5)

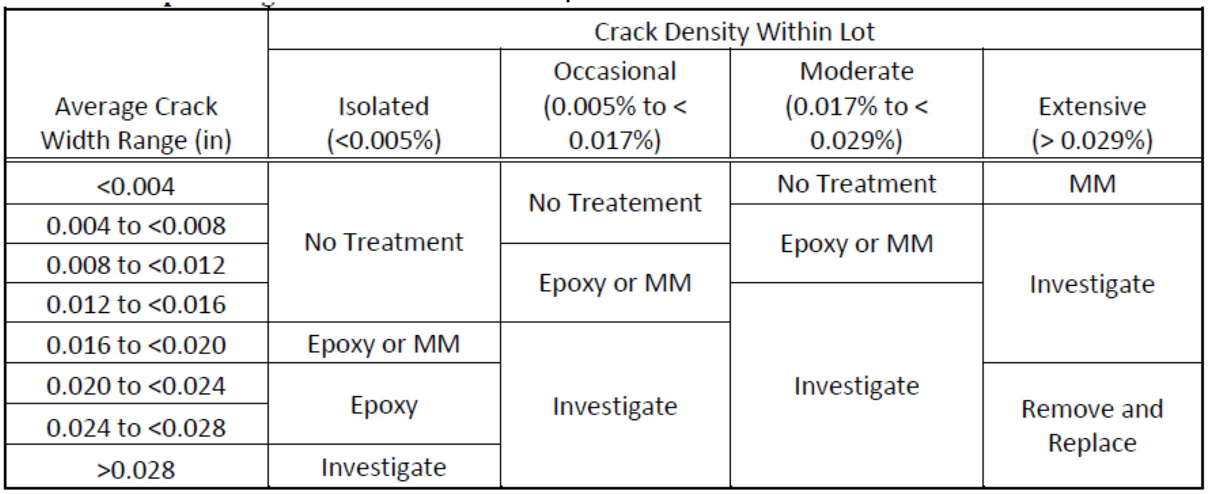

Average Crack Width Range (in)	Crack Density Within Lot			
	Isolated (<0.005%)	Occasional (0.005% to < 0.017%)	Moderate (0.017% to < 0.029%)	Extensive (> 0.029%)
<0.004	No Treatment	No Treatement	No Treatment	MM
0.004 to <0.008			Epoxy or MM	Investigate
0.008 to <0.012		Epoxy or MM		
0.012 to <0.016			Investigate	
0.016 to <0.020	Epoxy or MM	Investigate		
0.020 to <0.024	Epoxy			Remove and Replace
0.024 to <0.028				
>0.028	Investigate			

Ni et al(6) published a national survey of crack sealers for bridge decks from thirty-seven agencies in the United States. Their research evaluated available crack sealers, sealing triggers, approved product list and performance, resealing intervals, method selection, and surface preparation. Results from their surveys showed that Epoxy, Methyl methacrylate (MMA), and High-Molecular-Weight Methacrylate (HMWM) are the most commonly used crack sealers with each offering distinct advantages. Table 2 shows of the use of these four types among different states. The crack sealing criteria based on crack width was collected from few states DOT's and are summarized in Table 3. Ni et al. (6) suggested future research areas should focus on investigating the effects of entrapped chloride on crack sealers performance, conducting long-term performance testing of crack repair, and correlating laboratory and field data.

Table 2 - Use of four (4) sealant types in various states (6)

Agency	Epoxy	MMA	HMWM	OTHER
Arizona DOT	X		X	
Arkansas DOT	X		X	
Indiana DOT	X			X
Iowa DOT	X		X	
Minnesota DOT	X	X	X	
Missouri DOT	X	X	X	X
Nevada DOT	X		X	
New	X		X	
New York State	X	X	X	
New York City	X	X	X	
North Carolina	X		X	
North Dakota	X		X	
City of Seattle	X	X		
Texas DT	X	X		X

Utah DOT	X		X	
Vermont DOT	X	X		
Wisconsin DOT	X			X
Wyoming DOT	X		X	

Table 3 - Crack sealing criteria based on crack width from several DOT's (6)

Agency	**Criteria**	**Ref**
Illinois DOT	Cracks openings less than or equal to 12.7 mm are repaired by epoxy injection. Hairline cracks do not need sealing but should be noted. Cracks more than 12.7 mm should be sealed using cement grout	IDOT
Indiana DOT	Cracks openings 0.3 mm or larger should be sealed	InDOT
Michigan DOT	Cracks openings 0.2 mm or larger should be sealed	MDOT
Minnesota DOT	Cracks openings 0.25 mm or larger should be sealed	MnDOT
Missouri DOT	Cracks openings 0.2 mm or larger should be sealed	MoDOT

A study by Wiss Janney and Elstner (WJE) Associates, Inc. for Iowa DOT (1) reviewed the practices of crack repairs and crack maintenance strategies of 16 state DOT's. These include Illinois, Indiana, Iowa, Kansas, Michigan, Minnesota, Missouri, Ohio, Nebraska, North Dakota, South Dakota, Wisconsin, California, Florida, New York State, and Virginia. They reported that crack repair approaches and methods varied significantly. For example, some agencies, such as the South Dakota and North Dakota DOTs, do not discuss crack maintenance in their manuals. Other agencies, such as the Illinois DOT, provide limited discussion in their manuals and several DOTs, such as the New York State DOT, provide small tables for selecting a crack repair based on one or two crack properties. Indiana, Michigan, Virginia, and Wisconsin DOTs provide comprehensive decision matrices with guidance for selecting a repair or maintenance action broadly based on the condition state of the deck, but these tools do not provide guidance specific to addressing cracks. The Florida DOT provides the most comprehensive and focused tools for selecting a maintenance strategy for early-age bridge deck cracks. Examples of crack maintenance selection tables and matrices were also found in research literature for the bridge, nuclear, and pavement industries. Overall, information considered when selecting crack maintenance strategies included the National Bridge Inventory condition ratings, deck condition state, crack characteristics, and repair options properties. Potential crack repair or treatment strategies included doing nothing, penetrating sealers, crack-chasing methods, flood-coat methods, overlays, and deck replacement. Fig. 3 shows key crack elements of a bridge deck crack.

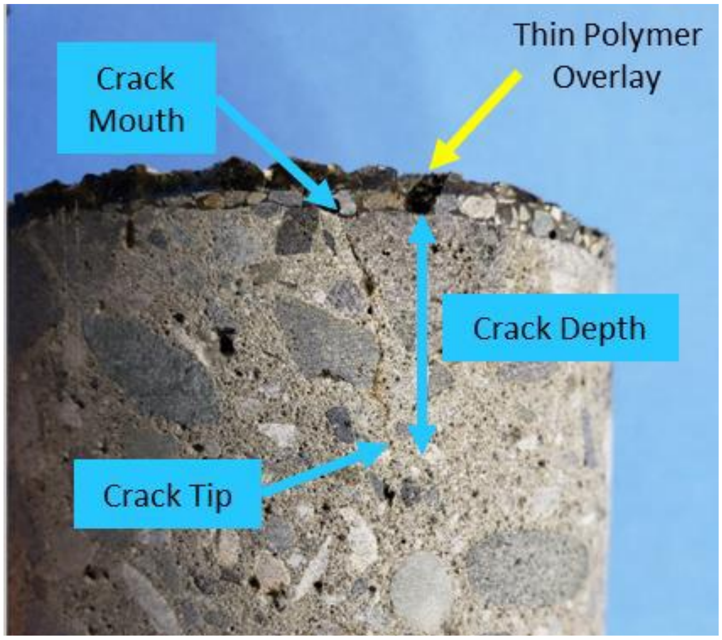

Figure 3. Key elements of a concrete deck crack (1)

The study summarized the concrete crack remediation and treatment procedures using information collected from various DOT's. They categorize crack repairs as follows:

- Do Nothing or 'Judicious Neglect'
- Penetrating Sealers
- Crack-Chasing Methods
- Flood coat Methods
- Overlays
- Replacement

Judicious Neglect only consists of the "Do Nothing" repair option. Penetrating Sealers also only consists of one repair option, "Apply a Penetrating Sealer," and the variety of penetrating sealer materials available are discussed in the Materials section of the profile. Flood coat Methods are grouped together under "Apply a Flood Coat" since the differences between applying a gravity-fed polymer (a.k.a. a healer-sealer) as a flood coat and applying a film-forming sealer are nuanced and these repairs are expected to perform similarly. In comparison, the crack-chasing methods differ significantly from each other and separate profiles for applying gravity-fed polymers, routing and sealing, and pressure injecting epoxy are necessary due to the vastly different types of materials used, construction methods, and performance of the repairs. Tables 4 shows number of times in which each of these crack repair options was considered in deciding on cracking repair and maintenance strategies from responding State DOT's. Tables 5 shows number of times in which each of these crack repair options and the corresponding repair material was considered in deciding on cracking repair and maintenance strategies from responding State DOT's.

Table 4 - Number of times in which each of the listed crack repair option was considered in deciding on cracking repair from State corresponding DOT's (1)

Repair Type	Crack Repair was Considered in Crack-Focused Decision Tool	Crack Repair was Considered in General Decision Tool	Crack Repair was Considered in Comprehensive Crack Repair Decision Tool	Total
Do Nothing	3	1	1	5
Clean and/or Wash Concrete Deck	1	2	0	3
Penetrating Sealers	4	2	1	7
Crack Chasing Method	4	0	2	6
Flood Coating Method	5	1	3	9
General Crack Sealing	5	4	0	9
Deck Sealing	0	1	0	1
Patching	0	5	0	5
Overlay	2	10	1	13

Table 5 - Number of times in which each of the listed crack repair method and material were considered in deciding on cracking repair from responding State DOT's (1)

Repair Type	Repair Detail	Crack Repair Considered in Crack-Focused Decision Tool	Crack Repair Considered in General Decision Tool	Crack Repair was Considered in Comprehensive Crack Repair Decision Tool	Total
Do Nothing		3	1	1	5
Clean/Wash Concrete Deck		1	2	0	3
General Crack Sealing	No method or Material Specified	2	4	0	6
	HMWM No method Specified	2	0	0	2
	Epoxy No method Specified	1	0	0	1
Deck Sealing	No Material Specified	0	1	0	1
Penetrating	No Material	1	1	0	2

Sealers	Specified				
	Silane	2	1	0	3
	Silane or Siloxane	0	0	1	1
Crack Chasing Method	Reactive Silicate Solution	1	0	0	1
	Gravity Fed Polymer	1	0	0	1
	HMWM	1	0	0	1
	Epoxy Injection	1	0	2	3
Flood Coating Method	Gravity Polymer	2	1	0	3
	HMWM	1	0	1	2
	HMWM or Polyurethane	0	0	1	1
	Epoxy	0	0	1	1
	Pavon In-Deck	1	0	0	1
	Chip Seal	1	0	0	1
Patching	Type Not Specified	0	3	0	3
	Wearing Surface	0	1	1	1
	Full Depth	0	1	0	1
Overlays	Thin Overlay (Not Specified)	0	1	0	1
	Thin Epoxy Overlay	2	2	1	5
	Polyester Polymer Concrete Overlay	0	1	0	1
	Rigid Overlay	0	3	0	3
	Flexible Overlay	0	1	0	1
	HMA Overlay with Water Proofing	0	2	0	2

Johnson (7) conducted a performance survey of crack sealers of several state DOT's as well as literature review of crack sealers. He highlighted four primary performance measures for crack sealers: 1) depth of penetration, 2) bond strength, 3) chloride content/resistance to corrosion, and 4) seepage rate.

He reported that epoxy crack sealers have the highest bond strength as well as a good resistance to freeze-thaw. However, HMWM products are much less viscous which enables them to achieve a larger penetration depth compared to epoxy sealers. Crack width, crack density, project characteristics, as well as existing (and future) research data on these sealers are important factors to consider when selecting the crack sealer that would work best for that particular application. Survey results showed that many states do not conduct acceptance tests to determine acceptable crack sealing products and products are typically chosen based on well-known existing research. Depth of penetration and chloride content tests are the most common (if any) QA/QC tests conducted on bridge decks (highly variable and scattered field results).He concluded that to better understand the selection and performance of crack sealers, more field research is needed on crack sealers and their performance including effects of freeze and thaw and changes in temperature, and previously sealed cracks. There is also a need to correlate and coordinate field and laboratory studies to better understand how laboratory results can be extrapolated to field performance,

The study by WJE(1) developed a comprehensive guide for Iowa DOT for remediating cracks in Iowa bridge decks that addresses a variety of cracking scenarios and criteria for selecting crack repairs methods and materials. Service life modeling was conducted to estimate the impact of cracking and crack maintenance strategies on the service life of bridge decks in Iowa. The modeling included chloride-induced corrosion, crack width, crack density, and age of application. The service life models investigated the application of the treatments when the bridge deck is 0, 2, 5, and 10 years old. The benefit of up to 3 applications of a penetrating sealer at regular intervals (4 and 6 years) was also investigated. Tables 6, 7, and 8 show summaries of decision matrix for crack remediation options for different crack width and crack density combinations at bridge deck age between 0 and 2 years, 5 years, and 10 years respectively (1).

Table 6 - Summary of decision matrix for crack remediation options for different crack width and crack density combinations at bridge deck age between **0 and 2 years** (1)

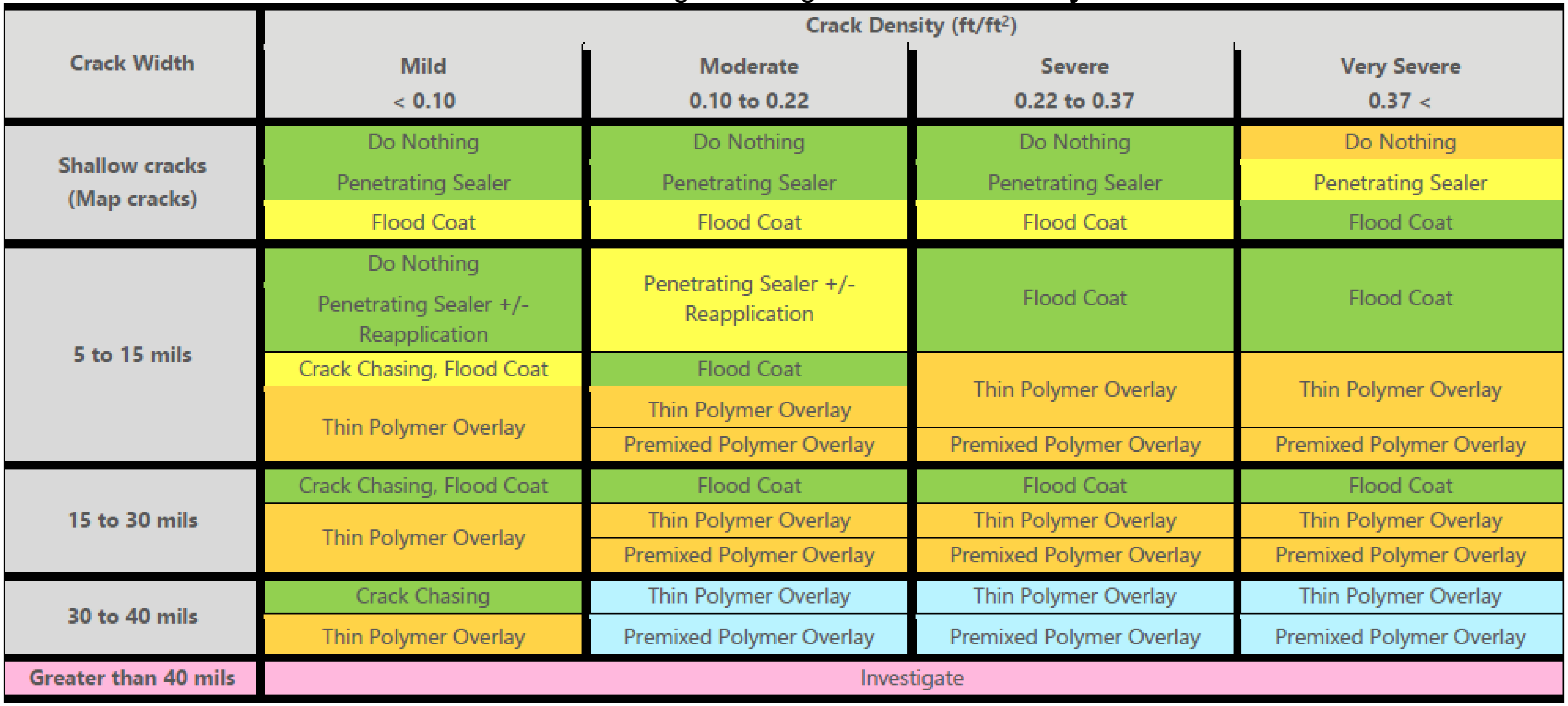

Crack Width	Crack Density (ft/ft^2) Mild < 0.10	Moderate 0.10 to 0.22	Severe 0.22 to 0.37	Very Severe 0.37 <
Shallow cracks (Map cracks)	🟩 Do Nothing 🟩 Penetrating Sealer 🟨 Flood Coat	🟩 Do Nothing 🟩 Penetrating Sealer 🟨 Flood Coat	🟩 Do Nothing 🟩 Penetrating Sealer 🟨 Flood Coat	🟧 Do Nothing 🟨 Penetrating Sealer 🟩 Flood Coat
5 to 15 mils	🟩 Do Nothing 🟩 Penetrating Sealer +/- Reapplication 🟨 Crack Chasing, Flood Coat 🟧 Thin Polymer Overlay	🟨 Penetrating Sealer +/- Reapplication 🟩 Flood Coat 🟧 Thin Polymer Overlay 🟧 Premixed Polymer Overlay	🟩 Flood Coat 🟧 Thin Polymer Overlay 🟧 Premixed Polymer Overlay	🟩 Flood Coat 🟧 Thin Polymer Overlay 🟧 Premixed Polymer Overlay
15 to 30 mils	🟩 Crack Chasing, Flood Coat 🟧 Thin Polymer Overlay	🟩 Flood Coat 🟧 Thin Polymer Overlay 🟧 Premixed Polymer Overlay	🟩 Flood Coat 🟧 Thin Polymer Overlay 🟧 Premixed Polymer Overlay	🟩 Flood Coat 🟧 Thin Polymer Overlay 🟧 Premixed Polymer Overlay
30 to 40 mils	🟩 Crack Chasing 🟧 Thin Polymer Overlay	🟦 Thin Polymer Overlay 🟦 Premixed Polymer Overlay	🟦 Thin Polymer Overlay 🟦 Premixed Polymer Overlay	🟦 Thin Polymer Overlay 🟦 Premixed Polymer Overlay
🟪 Greater than 40 mils	🟪 Investigate			

Notes:

1. Crack densities exceeding 0.37 ft/ft^2 shall be investigated prior to implementation of repairs.
2. Crack widths between 30 mils and 40 mils with a crack density exceeding 0.10 ft/ft^2 shall be investigated prior to implementation of repairs.
3. The decision tree does not apply to crack densities exceeding 0.50 ft/ft^2 or crack widths exceeding 40 mils.
4. Crack width information is used to exclude crack remediation options from selection. For this guide, it is assumed that if 25% of the deck cracks exceed the crack width limit for a given option, then that option should be excluded from viable options.
5. Refer to Table 5.10, Table 5.11 and Table 5.12 of the TR-782 Report for more detailed information regarding initial cost, time-to-5% damage, time-to-replacement, and lifecycle cost for the crack remediation options.

🟩 Most suitable option 🟧 Suitable option 🟨 Least suitable option
🟦 Thin polymer overlay or premixed concrete overlay is most suitable 🟪 Investigate

Table 7 - Summary of decision matrix for crack remediation options for different crack width and crack density combinations at bridge deck age of **5 years** (1)

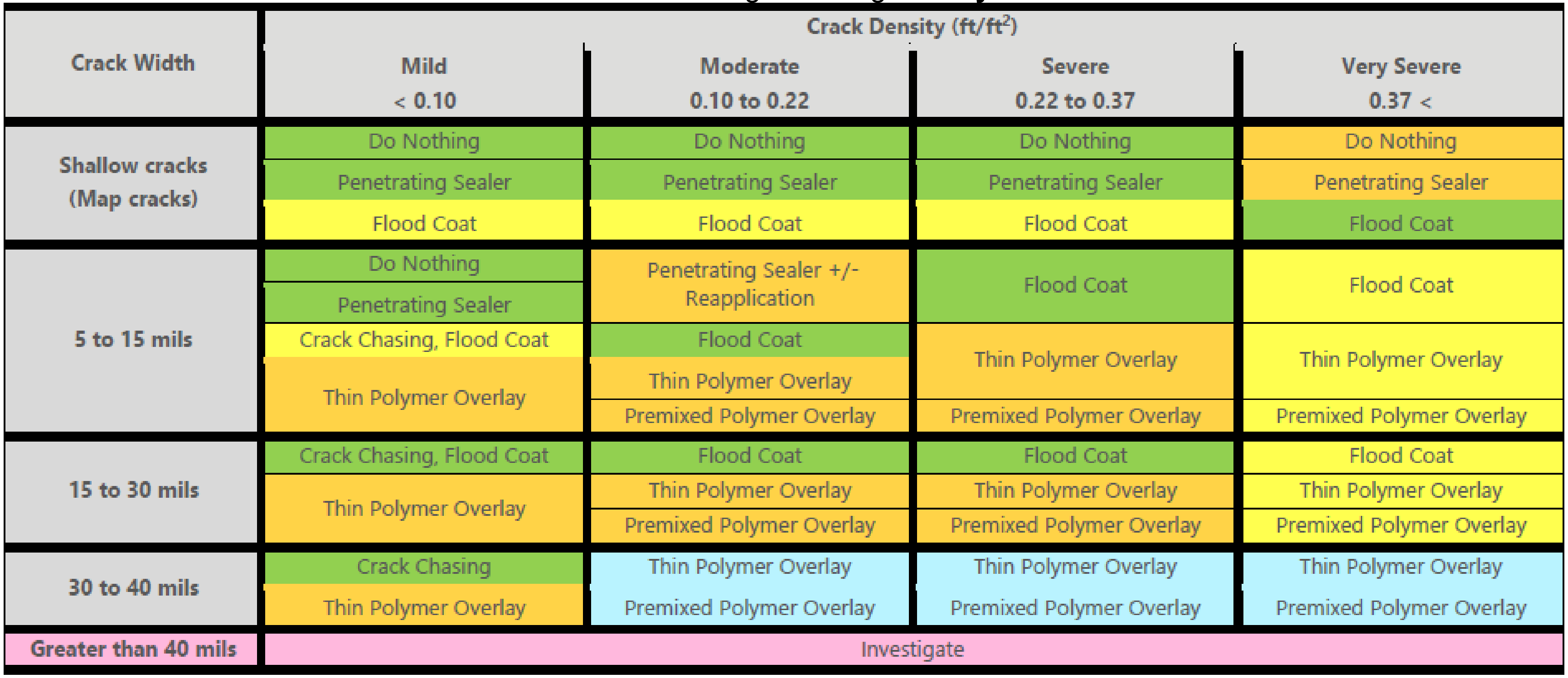

Crack Width	Crack Density (ft/ft^2)			
	Mild < 0.10	Moderate 0.10 to 0.22	Severe 0.22 to 0.37	Very Severe 0.37 <
Shallow cracks (Map cracks)	🟩 Do Nothing 🟩 Penetrating Sealer 🟨 Flood Coat	🟩 Do Nothing 🟩 Penetrating Sealer 🟨 Flood Coat	🟩 Do Nothing 🟩 Penetrating Sealer 🟨 Flood Coat	🟧 Do Nothing 🟧 Penetrating Sealer 🟩 Flood Coat
5 to 15 mils	🟩 Do Nothing 🟩 Penetrating Sealer 🟨 Crack Chasing, Flood Coat 🟧 Thin Polymer Overlay	🟧 Penetrating Sealer +/- Reapplication 🟩 Flood Coat 🟧 Thin Polymer Overlay 🟧 Premixed Polymer Overlay	🟩 Flood Coat 🟧 Thin Polymer Overlay 🟧 Premixed Polymer Overlay	🟨 Flood Coat 🟨 Thin Polymer Overlay 🟨 Premixed Polymer Overlay
15 to 30 mils	🟩 Crack Chasing, Flood Coat 🟧 Thin Polymer Overlay	🟩 Flood Coat 🟧 Thin Polymer Overlay 🟧 Premixed Polymer Overlay	🟩 Flood Coat 🟧 Thin Polymer Overlay 🟧 Premixed Polymer Overlay	🟨 Flood Coat 🟨 Thin Polymer Overlay 🟨 Premixed Polymer Overlay
30 to 40 mils	🟩 Crack Chasing 🟧 Thin Polymer Overlay	🟦 Thin Polymer Overlay 🟦 Premixed Polymer Overlay	🟦 Thin Polymer Overlay 🟦 Premixed Polymer Overlay	🟦 Thin Polymer Overlay 🟦 Premixed Polymer Overlay
🟪 Greater than 40 mils	🟪 Investigate			

Notes:

1. Crack densities exceeding 0.37 ft/ft^2 shall be investigated prior to implementation of repairs.
2. Crack widths between 30 mils and 40 mils with a crack density exceeding 0.10 ft/ft^2 shall be investigated prior to implementation of repairs.
3. The decision tree does not apply to crack densities exceeding 0.50 ft/ft^2 or crack widths exceeding 40 mils.
4. Crack width information is used to exclude crack remediation options from selection. For this guide, it is assumed that if 25% of the deck cracks exceed exceed the crack width limit for a given option, then that option should be excluded from viable options.
5. Refer to Table 5.10, Table 5.11 and Table 5.12 of the TR-782 Report for more detailed information regarding initial cost, time-to-5% damage, time-to-replacement, and lifecycle cost for the crack remediation options.

🟩 Most suitable option 🟧 Suitable option 🟨 Least suitable option
🟦 Thin polymer overlay or premixed concrete overlay is most suitable 🟪 Investigate

Table 8 - Summary of decision matrix for crack remediation options for different crack width and crack density combinations at bridge deck age of 10 years (1)

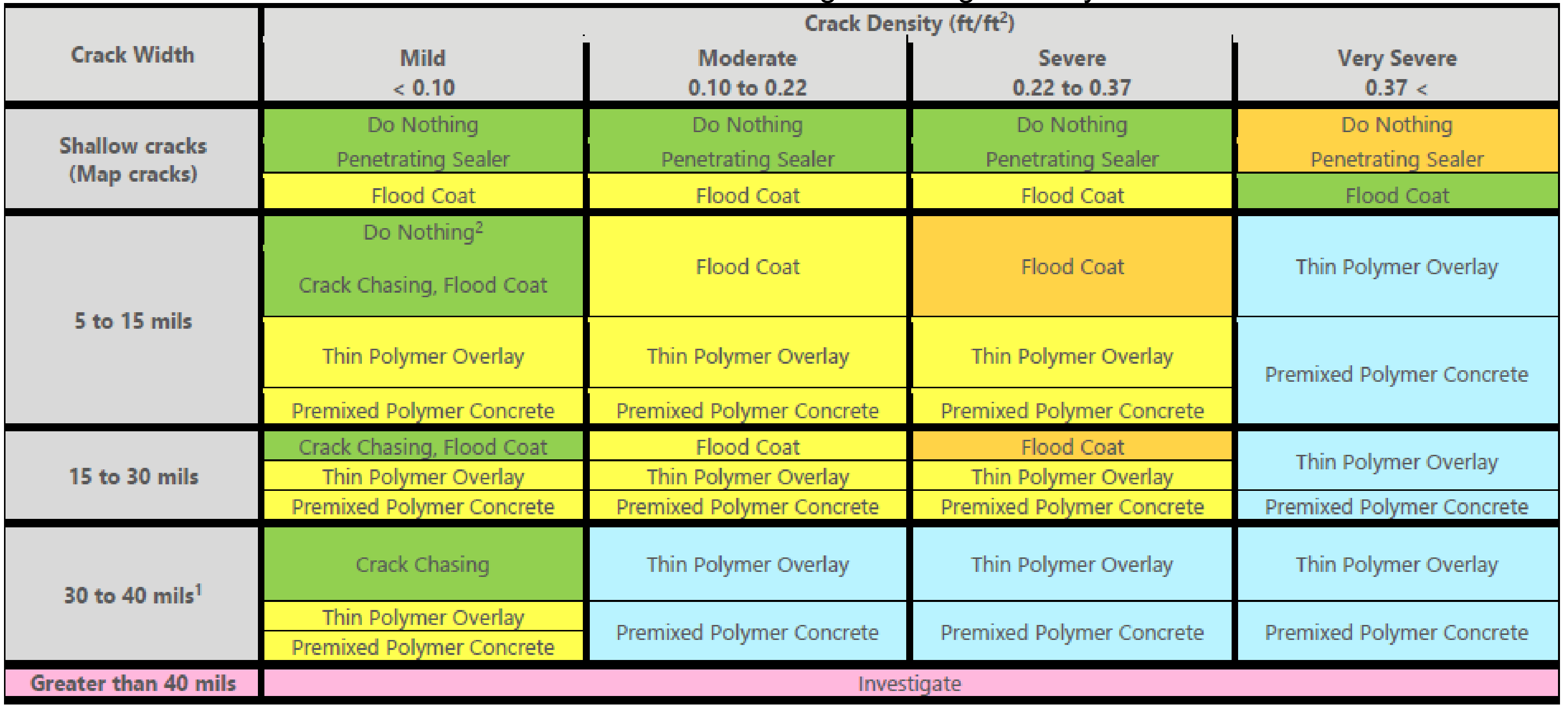

Crack Width	Crack Density (ft/ft^2)			
	Mild < 0.10	Moderate 0.10 to 0.22	Severe 0.22 to 0.37	Very Severe 0.37 <
Shallow cracks (Map cracks)	Do Nothing Penetrating Sealer Flood Coat	Do Nothing Penetrating Sealer Flood Coat	Do Nothing Penetrating Sealer Flood Coat	Do Nothing Penetrating Sealer Flood Coat
5 to 15 mils	Do Nothing[2] Crack Chasing, Flood Coat Thin Polymer Overlay Premixed Polymer Concrete	Flood Coat Thin Polymer Overlay Premixed Polymer Concrete	Flood Coat Thin Polymer Overlay Premixed Polymer Concrete	Thin Polymer Overlay Premixed Polymer Concrete
15 to 30 mils	Crack Chasing, Flood Coat Thin Polymer Overlay Premixed Polymer Concrete	Flood Coat Thin Polymer Overlay Premixed Polymer Concrete	Flood Coat Thin Polymer Overlay Premixed Polymer Concrete	Thin Polymer Overlay Premixed Polymer Concrete
30 to 40 mils[1]	Crack Chasing Thin Polymer Overlay Premixed Polymer Concrete	Thin Polymer Overlay Premixed Polymer Concrete	Thin Polymer Overlay Premixed Polymer Concrete	Thin Polymer Overlay Premixed Polymer Concrete
Greater than 40 mils	Investigate			

Notes:

1. Crack densities exceeding 0.37 ft/ft^2 shall be investigated prior to implementation of repairs.
2. Crack widths between 30 mils and 40 mils with a crack density exceeding 0.10 ft/ft^2 shall be investigated prior to implementation of repairs.
3. The decision tree does not apply to crack densities exceeding 0.50 ft/ft^2 or crack widths exceeding 40 mils.
4. Crack width information is used to exclude crack remediation options from selection. For this guide, it is assumed that if 25% of the deck cracks exceed the crack width limit for a given option, then that option should be excluded from viable options.
5. Refer to Table 5.10, Table 5.11 and Table 5.12 of the TR-782 Report for more detailed information regarding initial cost, time-to-5% damage, time-to-replacement, and lifecycle cost for the crack remediation options.

🟩 Most suitable option 🟧 Suitable option 🟨 Least suitable option
🟦 Thin polymer overlay or premixed concrete overlay is most suitable 🟪 Investigate

Crack Characterization and Repair

NJDOT (8) currently uses pressure injected epoxy for crack sealing and pneumatic grout injection. Other States (FDOT) use gravity polymer fill material such as methacrylate and low viscosity epoxies for wider dormant cracks. For narrow cracks they use pressure epoxy injection similar to NJDOT practices. NJDOT specifications Section 552 specifies materials, equipment and construction procedures for crack repairs using pressure injection sealing of cracks.

NJDOT Steps for Pressure Injection Sealing of Cracks

A. Crack Repair Survey.
The Resident Engineer (RE) shall examine the structure to verify the repair limits shown on the plans. At least 15 days before the start of crack repair, notify the RE in writing and make the work site available for this examination. The RE may increase or decrease the limits of repair based on the examination. The RE will schedule surveys during daylight hours unless the working time is restricted in the Contract.

B. Preparing for Repair.
Remove deteriorated, damaged, and loose concrete from the crack area. Drill port holes at 3 foot intervals along the crack. Perform additional surface preparation requirements according to the epoxy manufacturer's recommendations.

C. Sealing Surface Cracks
Seal the surface of the crack with an epoxy crack sealant. Ensure that this sealer does not obstruct the port holes for the pressure injected epoxy resin and is capable of containing the injected epoxy resin. Ensure that the sealant is hard before injecting the epoxy resin adhesive.

D. Injecting Epoxy Resin Adhesive
Mix and apply the epoxy resin adhesive according to the manufacturer's recommendations and the following. Begin by injecting the lowest entry port and continue until the epoxy adhesive has reached the next port hole in the crack. Stop injection and immediately seal the port hole before moving the injection to the next port hole. Continue the operation by injecting the epoxy resin adhesive into the next port hole in the crack. Continue the operation until the crack is filled.

E. Finishing the Surface.
When the crack has been filled and the epoxy resin adhesive has cured, grind smooth the surface of the crack repair area to match the surrounding concrete.

Epoxy Resin Injection Equipment
Provide a positive-placement, fixed-ratio type pump for injecting epoxy resin adhesive into concrete cracks. Ensure that the equipment is capable of automatically mixing 2 components at the nozzle. Also ensure that the equipment is equipped with a rubber nozzle arrangement that will allow injection of adhesive, without air entrapment, at pressures of up to 524 300 pounds per square inch to ensure complete penetration of

cracks. Also ensure that the machine is equipped with a pressure gauge at or near the nozzle to verify the working pressure.

NYSDOT (9) special specifications Section 555 specifies materials, equipment, and construction procedures for crack repair using crack sealing by epoxy injection. They specify two types of repairs:

1) Prevention to be used in cracked contaminated concrete areas to prevent movement and protect reinforcing item (555.80010001),

2) Restoration to be used in cracked uncontaminated concrete areas to restore structural integrity, item (555.80002000).

Crack Repair Procedure
Install injection ports, seal the crack opening, inject the crack with epoxy (full depth for restoration work, or as deep as conditions allow for prevention work), and restore the sealed surface to a flush condition in areas visible to the public. Perform the work at locations indicated on the contract plans or where directed by the Engineer.

PREVENTION: use in contaminated, cracked concrete areas to prevent movement and protect reinforcing.

RESTORATION: use in uncontaminated cracked concrete areas to restore structural integrity. Take verification cores for payment. Have an experienced epoxy manufacturer representative present until the work is acceptable to the Engineer. The following materials can be used for RESTORATION:

1. Crack Sealant - epoxy paste that completely cures in 4 hours or less and retains the injected epoxy. Any other type of crack sealant is subject to a project demonstration and approval by the Engineer.
2. Low Viscosity Injection Epoxy - Manufacturer certified to meet ASTM C881, Type I or IV, Grade 1, Class B or C (as temperature conditions require.)
3. Vertical and Overhead Patching Material (Approved List)

INJECTION EQUIPMENT: Use equipment in good working order, as approved by the Engineer, with the following features:

- Separate feed lines to the mixing chamber
- Automatic mixing and metering pump
- Ability to thoroughly mix the epoxy components in the mixing chamber
- Operator control of the epoxy flow from the mixing chamber
- Clean, legible, accurate pressure gauges easily viewable by the operator
- Ability to provide an uninterrupted pressure head to continually force epoxy into the cracks • Injection pressure from 0 to at least 200 PSI. Capable of metering each epoxy component to within 3.0% of the epoxy manufacturer's mix ratio. Un-reacted epoxy components may be stored overnight in separate reservoirs and feed lines. Before starting the work, demonstrate to the Engineer the ability of the equipment to meter and

mix epoxy components to the required mix ratio. Ratio accuracy may be determined by simultaneously metering each component into separate, clean, accurately graduated, volumetric containers, or another procedure approved by the Engineer. Also, activate the automatic mixing and metering pump, mix a small amount of injection epoxy, and waste it into a disposable container. The Engineer will observe this trial operation and be satisfied the equipment is working properly, and the epoxy is mixed with no streaks.

1. Crack and Surface Preparation: Remove all debris or contaminants accessible within the cracks by using hand tools, water blasting or oil-free high pressure air blasting, vacuuming, or other methods suitable to the Engineer. Epoxy resin will not penetrate compacted, water or oil soaked debris. Allow free moisture within the crack to be absorbed before injecting epoxy. Remove all materials, including moisture, from the surface adjacent to the crack which might interfere with bonding of the crack sealant.

2. Injection Port Installation: Attach injection ports to the prepared surface by placing them onto (surface adapters) or into the cracks (socket ports) and affixing with crack sealant. Larger cracks may be ported by inserting an anchored tube into the crack. Use positive connection port designs to connect injection equipment to the ports. Other injection port designs and attachment methods, where worker fatigue would not be a problem, require approval by the Engineer. Use the following general guidelines for spacing injection ports when cracks are uniform in width through the structure. For cracks that get tighter with depth, double this spacing. Intermediate ports may be placed for observation. To permit maximum flow into the void, position ports on the wider crack sections and at intersections, rather than at an exact spacing. If these guidelines cannot be followed, use port locations approved by the Engineer. Port spacing may be modified by the Engineer as experience is gained, or when cores are taken to determine penetration.

3. Crack Seal: After port installation, seal the crack opening with crack sealant, being careful not to plug the injection ports. Allow the crack sealant to cure completely before injecting epoxy. Apply crack sealant only when surface and ambient temperatures are above 50º F.

4. Port Flushing: Prior to any epoxy injection, flush critical ports with oil-free compressed air to verify that air exits from all the installed ports, dry the cracks, and check for leaks.

5. Epoxy Injection. Perform epoxy injection only when the surface and ambient temperatures are above 45º F and are not expected to fall below 45º F during the next 24 hours.

6. Crack Repair by Epoxy Injection (Restoration): Take cores ranging in diameter from 1 to 4”, as approved by the Engineer, to verify full penetration by epoxy and its cure. Take a representative core from each structural element, or one from every 100 feet of crack repaired, whichever is greater, at locations approved by the Engineer. The Engineer will retain the cores and determine if they are acceptable for payment.

Patch the holes with Vertical & Overhead Patching Material. More than one core may be necessary to obtain an acceptable sample from cracks that diverge below the surface. (To avoid cutting reinforcing, the core drill may be angled to intercept a crack behind the reinforcing.)

7. Clean Up: In all areas visible to the public, as determined by the Engineer, remove spillage, the ports and crack sealant until flush with the adjacent surface. Remove stains and repair any damage to the satisfaction of the Engineer at no additional cost.

Several studies (6,7,10) have looked into crack characterization based on crack widths and decision making. Table 9 shows crack characteristics for epoxy injection from NYSOT, VDOT, and MNDOT.

Table 9 - Crack widths for epoxy injection (10)

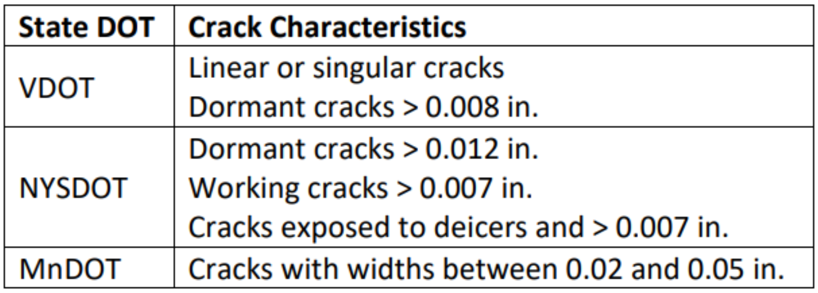

State DOT	Crack Characteristics
VDOT	Linear or singular cracks Dormant cracks > 0.008 in.
NYSDOT	Dormant cracks > 0.012 in. Working cracks > 0.007 in. Cracks exposed to deicers and > 0.007 in.
MnDOT	Cracks with widths between 0.02 and 0.05 in.

Ni (6) looked at crack sealing criteria based on crack width from several_state DOT's experiences, as shown in Table 10.

Table 10 - Crack sealing criteria based on crack width from several DOTs (6)

Agency	Criteria	Ref
Illinois DOT	Cracks openings less than or equal to 12.7 mm (0.5 in) are repaired by epoxy injection. Hairline cracks do not need sealing but should be noted. Cracks more than 12.7 mm should be sealed using cement grout.	IDOT
Indiana DOT	Cracks openings 0.3 mm (0.012 in) or larger should be sealed	InDOT
Michigan DOT	Cracks openings 0.2 mm (0.008 in) or larger should be sealed	MDOT
Minnesota DOT	Cracks openings 0.25 mm (0.01 in) or larger should be sealed	MnDOT
Missouri DOT	Cracks openings 0.2 mm (0.008 in) or larger should be sealed	MoDOT

Issa et al. (10) recommended a Do-Nothing action for crack width < 0.008 in based on literature review from various states on crack width and recommended actions as shown in Table 11.

Table 11 - Crack width range for Do-Nothing Action (10)

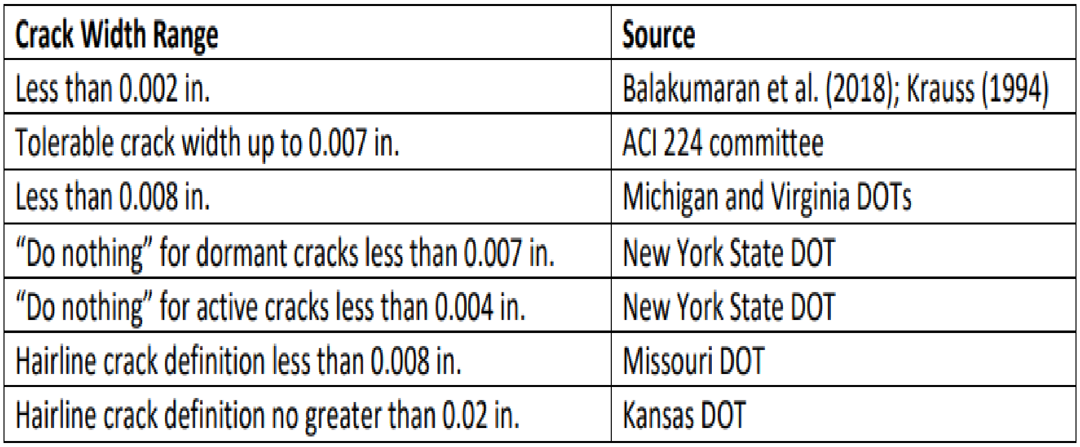

Crack Width Range	Source
Less than 0.002 in.	Balakumaran et al. (2018); Krauss (1994)
Tolerable crack width up to 0.007 in.	ACI 224 committee
Less than 0.008 in.	Michigan and Virginia DOTs
"Do nothing" for dormant cracks less than 0.007 in.	New York State DOT
"Do nothing" for active cracks less than 0.004 in.	New York State DOT
Hairline crack definition less than 0.008 in.	Missouri DOT
Hairline crack definition no greater than 0.02 in.	Kansas DOT

The AASHTO manual of bridge inspection (MBEI)(11) published recommendation for crack width range for reinforced and prestressed concrete as insignificant, moderate and wide as shown in Table 12.

Table 12 - Classification of cracks 'Insignificant', 'Moderate', and 'Wide' (11)

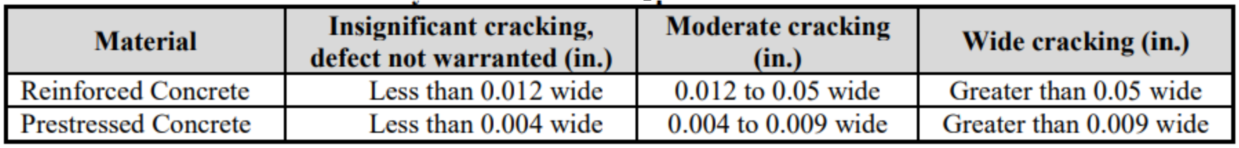

Material	Insignificant cracking, defect not warranted (in.)	Moderate cracking (in.)	Wide cracking (in.)
Reinforced Concrete	Less than 0.012 wide	0.012 to 0.05 wide	Greater than 0.05 wide
Prestressed Concrete	Less than 0.004 wide	0.004 to 0.009 wide	Greater than 0.009 wide

The NJ Turnpike Authority Bridge manual included four condition states for cracks or defects similar to those in AASHTO MBEI (8) as shown in Table 13.

Table 13 - NJTP Concrete cracking, definitions, and recommendations (12)

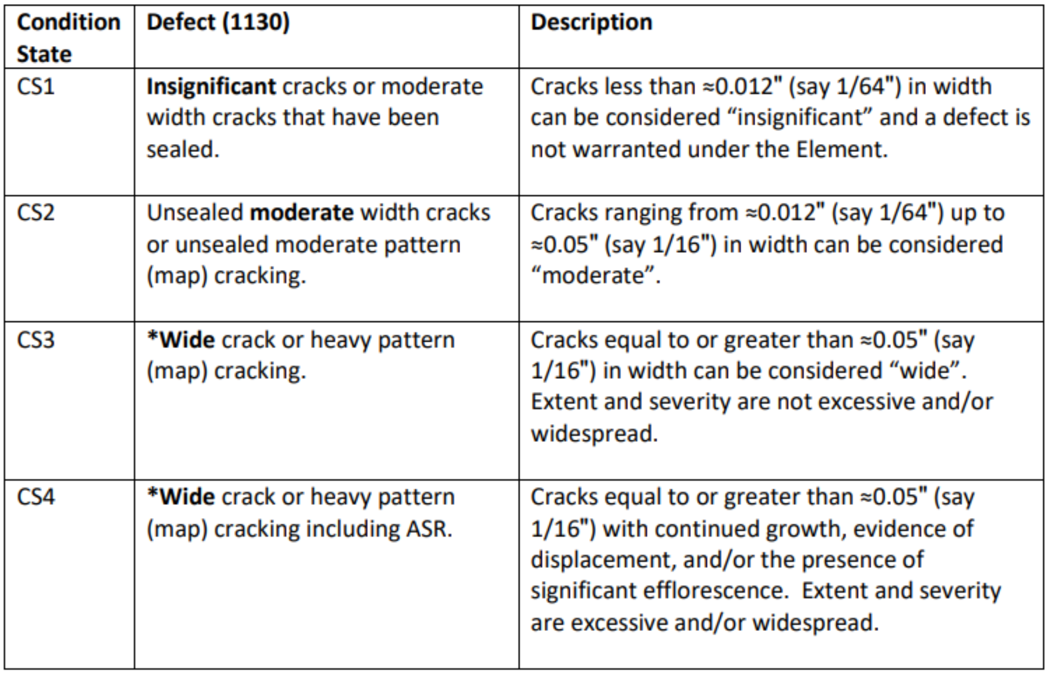

Condition State	**Defect (1130)**	**Description**
CS1	**Insignificant** cracks or moderate width cracks that have been sealed.	Cracks less than ≈0.012" (say 1/64") in width can be considered “insignificant” and a defect is not warranted under the Element.
CS2	Unsealed **moderate** width cracks or unsealed moderate pattern (map) cracking.	Cracks ranging from ≈0.012" (say 1/64") up to ≈0.05" (say 1/16") in width can be considered “moderate”.
CS3	***Wide** crack or heavy pattern (map) cracking.	Cracks equal to or greater than ≈0.05" (say 1/16") in width can be considered “wide”. Extent and severity are not excessive and/or widespread.
CS4	***Wide** crack or heavy pattern (map) cracking including ASR.	Cracks equal to or greater than ≈0.05" (say 1/16") with continued growth, evidence of displacement, and/or the presence of significant efflorescence. Extent and severity are excessive and/or widespread.

As mentioned earlier ACI 224(13) referenced vacuum assisted methods for epoxy injection into cracks. Tecvac, Inc. (14) provides information and details on vacuum assisted injections. According to Tecvac, vacuum assisted injection routinely fills 0.001 in cracks. They also reference petrographic reports from the CTL Labs in Chicago that show cracks as narrow as 5 microns wide being filled using vacuum technology.

They report the success of this method is due a combination of vacuum and ultra-low viscosity repair materials, and no pressure. They use low molecular weight MMA (MethylMethacrylate). This material shares all of the physical properties of epoxy yet is just about as thin as water. It has the ability to migrate into places epoxies may not reach. MMA has some drawbacks such as smell, tends to bubble when put under pressure and is not easily metered. Fig. 4 and 5 show vacuum assisted crack injection for a concrete barrier and concrete wall respectively (14). Balvac (15) is another company that uses vacuum assisted injections for crack repairs. The company is a subsidiary of Belfour Beatty construction Inc. in the UK and had a patent for vacuum assisted injection. Fig. 6 shows vacuum assisted grout injection for a concrete deck.

Figure 4. Vacuum assisted injection method (14)

Figure 5. Vacuum assisted injection method (14)

Figure 6. Vacuum assisted grout injection for a concrete deck (15)

LABORATORY TESTING OF CONCRETE CRACK REPAIR

Crack Repair Formulations

The project was aimed at developing formulations for repair of macro and micro cracks in concrete. The repair formulations were evaluated based on two main criteria: workability and injection into the crack using various delivery methods. Three selected formulations were selected. Formulations A have Portland Cement, Micro fly ash, very fine sand, and superplasticizer. Formulations B uses products on the NJDOT QPL list including CTS Cement and Quikrete Quick-Setting Cement. These two types of cement are specially formulated with added polymers, very fine sand and superplasticizers. Formulations C are geopolymer based formulation which includes metakaolin, micro fly ash, zirconium sand, iron oxide and superplasticizer.

Horizontal, inclined, and vertical injection were performed using these formulations. Two injection methods were used: manual injection and automatic injection using cordless caulk gun. The developed formulations were successfully injected into 1/8 in (3mm crack width) using the automatic cordless caulk gun. These formulations, the mix trials, the automatic injections process along with injection parts are explained in detail in the following sections.

Formulation A

Formulation A included the following components: Portland Cement Type I, Micro fly ash, and No. 100 fine sand. The No. 100 sand is very fine sand, with particles that pass through a No. 100 sieve. Particles passing through No. 100 sieve typically have a of diameter of 0.15 mm (150 μm) or smaller. No. 200 sand has particle size smaller than 0.075 mm. **Table 14** shows the different mixes tried under formulation A. Table 15 shows the material used in formulation A trial mixes and their particle sizes and composition.

Table 14 - Various trial mixes for Formulation A

Material	Mix A1	Mix A2	Mix A3	Mix A4	Mix A5	Mix A6	Mix A7	Mix A8
Type I portland cement	1.0	1.0	1.0	1.0	1.0	1.0	1.0	1.0
fine sand (no. 100 mesh)	1.0	1.0	1.0	2.0	3.0	3.0	3.5	-
micro fly ash	0.5	0.5	0.5	0.5	0.5	0.4	0.5	-
metakaolin	-	-	-	0.5	-	0.2	0.2	-
silica fume	-	-	-	-	-	0.1	0.1	-
iron oxide	-	-	-	-	-	-	-	1.0
zinc oxide	-	-	-	-	-	-	-	0.1
water/cementitious ratio	0.26	0.3	0.4	0.325	0.41	0.41	0.48	0.25
super platicizer	5%	3%	5%	5%	5%	5%	5%	5%

Table 15 - Materials used in formulations with composition and particle size

Material	**Particle size**	**Composition**					
		SiO_2	**Al_2O_3**	**CaO**	**Fe_2O_3**	**ZnO**	**$ZrSiO_4$**
Portland Cement I	10μm to 20μm	**20 %**	5 %	**65 %**	2 %	-	-
Fly Ash	5μm to 30μm	**50 %**	**20 %**	5 %	5 %	-	-
Metakaolin	1μm to 10μm	**50 %**	**40 %**	0 %	2 %	-	-
Silica Fume	0.1μm to 1μm	**96 %**	< 1 %	< 1 %	< 1 %	-	-
Sand (No. 50 Mesh)	150μm to 300μm	**90-95 %**	< 1 %	< 1 %	< 1 %	-	-
Sand (No. 100 Mesh)	80μm to 150μm	**90-95 %**	< 1 %	< 1 %	< 1 %	-	-
Sand (No. 200 Mesh)	40μm to 80μm	**90-95 %**	< 1 %	< 1 %	< 1 %	-	-
Iron Oxide	1μm to 10μm	-	-	-	99%	-	-
Zinc Oxide	10nm to 200nm	-	-	-	-	99%	
Zircon Sand	60μm to 100μm	-	-	-	-	-	99%
CTS Cement ALL	10μm to 20μm	-	-	-	-	-	-
Quikrete Quick-Set Cement	10μm to 20μm	-	-	-	-	-	-

Workability

Mix A1 performed well compared to the other trial mixes shown in Table 14. It has good workability and good working time. Its setting time varied between 40 min to 50 min. Fig. 7 shows Mix A1 just before pouring it into the injection tube. Fig. 8 shows Mix A1 being dispersed from injection tube into thin plates for flexural testing. Table 16 summarizes workability observations and setting times of the various trial mixes of Formulation A.

Figure 7. Mix A1 just before pouring it injection tube.

Figure 8. Mix A1 being poured into thin plates for flexural testing

Table 16 - Workability observations for Formulation A

Mix ID	Temp (Celsius)	Workability and Initial Setting Observations
Mix A1	75	**Mix A1** was very fluid. It had very good workability and can be easily configured and prepacked by suppliers and contractors. Infiltrated 1/8 and 1/4 in cracks with minimal pressure. Also infiltrated inclined/vertical cracks. Initial setting time was about 40 minutes.
Mix A2	73	**Mix A2** was less fluid compared to Mix **A1** and infiltrated the crack relatively easily but there was still separation between water and fine particles observed inside the crack
Mix A3	75	**Mix A3** was too fluid. Easily infiltrated the crack but separation between water and fine particles was observed inside the crack
Mix A4	74	**Mix A4** had Metakaolin and two times more sand than **mixes A1, A2, and A3.** It required more water to achieve very good workability similar to that of mix **A1**. Initial setting was about 25 minutes.
Mix A5	74	**Mix A5** has 3 times more sand than Mixes **A1, A2** and **A3** and 1.5 times more sand than mix **A4** and requires more water to have very good workability similar to mixes **A1** and **A2**. Initial setting time about 30 minutes.
Mix A6	75	**Mix A6** has silica fume and metakaolin and required more water, has good workability but was not tested in filling 1/8 in cracks. Initial setting 20 minutes.
Mix A7	72	**Mix A7** had about 20% more sand than mix **A6**. It required more water, has good workability but was not tested in filling 1/8 in cracks. Initial setting about 20 minutes
Mix A8	75	**Mix A8** had iron oxide and zinc oxide. It was viscous and did not infiltrate the crack. Initial setting time about 15 minutes

Figure 9 - Artificial 1/8 in and 1/4 in cracks cut in concrete blocks

Fig. 9 shows two concrete blocks with 1/8 in and 1/4 in cracks injected with Mix A1. After the injection was complete, the bricks were sliced into 3 slices to check injection penetration. Fig. 10 shows slices cut from the injected concrete block with 1/8 in crack width that show the depth of penetration of the injected material and the integrity of the repair process.

Figure 10. Slices cut from the injected concrete block with 1/8 in crack width.

Formulation B

Formulation B focused on two products available in the NJDOT QPL list: 1) Rapid-set Cement All, and 2) Quikrete Quick-Setting Cement. Rapid Set Cement All is a high-quality, durable, easy-to-use, multi-purpose repair material that can be used for almost any type of concrete work including crack repair, concrete repair, grouting, and anchoring as well as other rapid set applications. It is ideal when rapid strength gain, high durability and low shrinkage are desired. Its setting time is 15 minutes and it is ready to drive or build on in 1 hour. It is durable in wet environments; it can be applied from featheredge to 4 in. thick. Cement All is a blend of high-performance Rapid Set cement with fine graded sand. Cement All offers superior resistance to sulfate attack. It is non-metallic and no chlorides are added. The water cement ratio varies from 0.1 to 0.15

Quikrete Quick-Setting Cement is a very fast setting concrete repair product. It has unique characteristics of being able to be sculpted and molded as it sets and can be used for crack repairs, concrete repairs, edges of curbs and concrete steps.

Its setting time is 10-15 minutes. The water cement ratio varies from 0.2 to 0.25. Table 17 shows the trial mixes using Rapid Set Cement All and Quikrete Quick-Setting Cement. Table 17 shows the various trial mixes for Formulation B.

Table 17 - Trial mixes for Formulation B

Material	**Mix B1-RS**	**Mix B2-RS**	**Mix B3-RS**	**Mix B4-QK**	**Mix B5-QK**	**Mix B6-QK**
Rapid-Set Cement All	**1.0**	**1.0**	**1.0**	**-**	**-**	**-**
Quikrete Quick-Setting Cement	**-**	**-**	**-**	**1.0**	**1.0**	**1.0**
water/cementitious ratio	**0.15**	**0.15**	**0.10**	**0.23**	**0.15**	**0.25**
super plasticizer	**3%**	**5%**	**5%**	**3%**	**5%**	**3%**

Workability

Mix B1-RS made of Rapid Set Cement All with 0.15 water cement ratio performed well compared to B2-RS and B3-RS. Mix B1-RS has good workability and sufficient good working time. Its setting time varied between 12 min to 18 min. Figure 11 shows Mix B1-RS after mixing and being poured into plastic mold. Table 18 describes workability observations for Mixes of formulation B.

Figure 11. Mix B1-RS after mixing and being poured into plastic mold

Table 18 - Summarizes workability observations and setting times for Mixes B

Mix ID	Temp (Celsius)	Workability and Initial Setting Observations
Mix B1-RS	72	**Mix B1-RS** was very fluid. It had very good workability and can be easily configured by contractors. Infiltrated 1/8 and 1/4 in cracks with minimal pressure. Also infiltrated inclined/vertical cracks. Initial setting time was about 15 minutes.
Mix B2-RS	72	**Mix B2-RS** was very fluid and more than B2-RS. Excellent workability and can be easily configured by contractors. Infiltrated 1/8 and 1/4 in cracks with minimal pressure. However, potential for shrinkage is higher for this mix.. Initial setting time was about 18 minutes.
Mix B3-RS	74	**Mix B3-RS** was very fluid but less than B1-RS. It had good workability and can be configured by contractors. Infiltrated 1/8 and 1/4 in cracks with more needed pressure. Initial setting time was about 12 minutes.
Mix B4-QK	74	**Mix B4-QK** had very good workability and can be configured by contractors. Infiltrated 1/8 and 1/4 in cracks with more needed pressure. Initial setting time was about 20 minutes.
Mix B5-QK	75	**Mix B5-QK** had good workability but less than B4-QK. Initial setting time was about 20 minutes.
Mix B6-QK	75	**Mix B6-QK** had very good workability but more potential for shrinkage due to higher w/c ratio. Initial setting was about 20 minutes.

Formulation C

Formulations C are composed of geopolymer based formulation which includes metakaolin, micro fly ash, zirconium sand, iron oxide and superplasticizer. This formulation required high speed mixing for good flow and workability. The mix has two parts: Part A which is comprised of potassium alumino silicate and lithium silicate, and Part B which includes metakaolin, micro fly ash, ultra fine zirconium sand and iron oxide. Table 19 shows thirteen different trail mixes made for formulation C. The table also shows the modifications in the mix proportions and the added superplasticizer. This geoploymer mix is well suited for ultra-thin cracks where cracking sealing is desired through application of single or more coats.

Mix 9 shows the best performance in terms of mixing, workability, flowability and ease of application. For Mix 9, the ratio of Part A to Part B was 1:1.2. Part A included potassium alumino silicate and lithium silicate in the ratio 9:1. Part B included metakaolin, micro fly ash, zirconium sand, and iron oxide in these ratios: 1:3.5:2.5:0.5 with 1% to 3% superplasticizer. Fig. 12 shows coating of a 4 in x 2 in concrete surface surface using Mix 9 from formulation C.

Table 19 - Trial Mixes for Formulation C (Geopolymer-based mixes)

	Mix Date	11/1/2024	11/15/2024	11/15/2024	11/20/2024	11/20/2024	11/20/2024	12/11/2024	12/11/2024	2/28/2025	2/28/2025	3/7/2025	3/14/2025	3/25/2025	3/28/2025	4/1/2025	4/1/2025	4/11/2025
Part A (Commercial)		**1**	**2**	**3**	**4A**	**4B**	**4C**	**5A**	**5B**	**6A**	**6B**	**7**	**8**	**9**	**10**	**11**	**12**	**13**
Lithium silicate		75	75	75														
Lithium Polysilicate					5	5	5	5	5	5	5	5	5	5	10	10	10	10
Potassium Silicate								45	45	45	45	45	45	45	90	90	90	90
Part A (Lab Made)					45	45	45											
Water	1000																	
Potassium Silicate (Solids)	920																	
White Silica Fume	840																	
Part B1	Proportions	75	75	75	50	50	50	50	50	50	50	50	50	60				
Fly Ash (PV120)	70g																	
Metakaolin	20g																	
Iron Oxide	10g																	
Zirconium sand	50g																	
Part B2	Proportions														150	75	75	
Fly Ash (PV120)	70g																	
Metakaolin	20g																	
Iron Oxide	10g																	
Silica Fume	20g																	
Part B3	Proportions																	80
Fly Ash (PV120)	70g																	
Metakaolin	20g																	
Iron Oxide	10g																	
Part C																		80
White Desert Sand															200	25	50	
Zirconium Sand																		40
Cement		5	15	10		5	10				5						5	
Zinc Powder								25	2.5			1	0.5					
Super Plasticizer															5			

Figure 12. Coating of a 4 in x 2 in concrete surface using Mix 9 of Formulation C

Injection Procedures

All developed mixes had excellent workability and flow that makes suitable different crack types. The developed formulations can be injected using powered caulk guns and can also be gravity injected when necessary. Cracks widths of 1/8 in (3 mm) and 1/4 (6 mm) in were cut into 8in x 4in x 2 in as was shown in Fig. 8. In addition, longer cracks created by fabricating 14 in x 4 in x 4in concrete samples as shown in Fig. 13.

Figure 13. Concrete crack 14 in long, 2mm wide, and 2 in deep created in the lab

Prior to injection the top of the crack was sealed by adhesive tape and the injection port was sealed as well. A 3/8 in. hole was drilled at one end of the crack and rigid plastic injection port was pushed into the hole and sealed 24 hours prior to injection. A battery-powered caulk gun was used to inject the repair material into the crack. The cordless caulk gun can exert pressures up to 350 psi during injection. The battery-powered caulk was sufficient to inject cracks vertically up to 14 in and possibly more depending on the crack width. The capacity of the caulking tube is 10 oz (300 ml). The caulk gun is shown in Fig. 14.

Figure 14. Battery-powered caulk gun

Fig. 15 shows 14 in long crack before injection and after injection. The crack width was 3 mm and injection was vertical injection. As shown in the right image of Fig. 15, the filler material was able to inside the crack all the way up to the top travelling more than 14 in. The formulation used to inject this crack was formulation B (Mix B1-RS). Other formulations also performed as well.

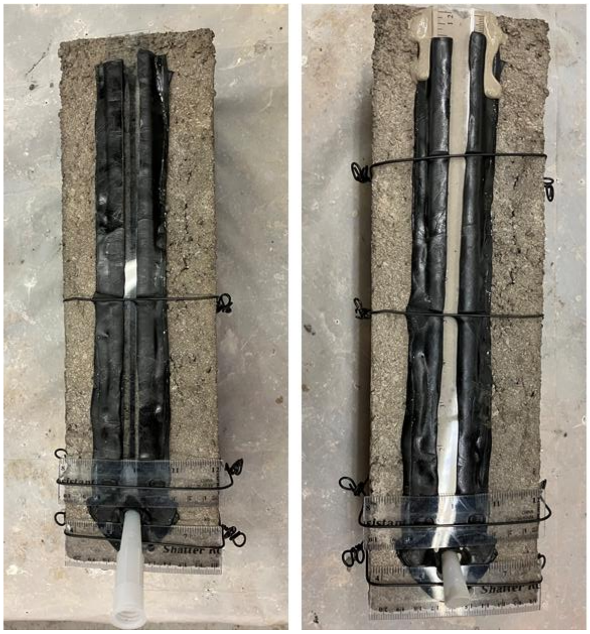

Figure 15. Vertical injection of 14 mm long crack with a crack width of 3mm

Deteriorations resulting in irregular surfaces such as those encountered in spalling of vertical columns or vertical walls can also be repaired using the formulations developed in this study. Fig. 16 shows a concrete cylinder that was split into pieces. A piece of Plexiglas was placed on top of one piece, and its edges were taped using adhesive tape. Two holes were drilled in the Plexiglas for injection at the bottom and for air release near the top. The half cylinder was injected vertically up to 7.5 in as shown in Fig. 16 using Mix A1. Other mixes performed as well.

Figure 16. Vertical injection of half-concrete cylinder with irregular surface

In addition to the vertical injection, horizontal injection and inclined injection were performed on various samples as shown in Fig. 17. The horizontal injection performed well with a cordless caulk gun and also using gravity flow for wider cracks.

One of the key steps in the injection process is to completely seal the injection port in place and seal its surroundings using strong adhesives and leaving them to completely set over 24 hours. The pressure build at the injection port is significant and leakage can occur if the seal is not tight. In addition, using pressure to wet the crack location prior to injection can improve the injection and the flow of the injection material. Vertical injections require the most pressure and should be done in short segments to avoid pressure build up and leakage. The segment length depends on several factors including: 1) filler material flowability, 2) crack width, 3) crack geometry, and 4) injection pressure.

It is worth noting that making a groove near the entry port helped in allowing the repair material to flow deeper into the crack. Although we did not extend the groove along the crack, making a groove was still helpful in the injection process. Other advantages of the groove are removal of surface contaminants and providing a cap seal that can hold up the repair material in place.

Pull Off Tests

The pull-off test was used to determine adhesion (bond) strength and its correlation to factors that can adversely affect adhesion and its quality such as surface preparation and mix properties. The tests were conducted using the specification of ASTM D4541-17(16), Standard Test Method for Pull-Off Strength of Coatings Using Portable Adhesion Testers. ASTM D4541-17 is the standard test method for measuring the pull-off strength of coatings using portable adhesion testers. The test involves gluing dollies to the coating and using a portable tester to pull it off, measuring the maximum tensile force required for detachment. The pull off tester used was PosiTest® AT-M Manual Adhesion Tester as shown in Figure 17. In this research, the adhesion of the various formulations developed in this investigation was measured. For these tests, half 4 in x 8 in concrete cylinders were used as the base material. A thin layer for material to be tested as cast on top of the half cylinders. The thickness of the material on the top of the half cylinder varied between 1/2 in. to 3/4 in. A 25 mm in diameter drill bit was used to make 20 mm cores in the half cylinders as shown in the left image of Figure 18. A minimum of three 20 millimeter pull off dollies were glued to the circular cored areas within the scribe using a two-part manufacturer supplied epoxy as shown in the right image of Figure 18. The epoxy was cured for a minimum of 24 hours. The test was performed after the cast material has reached its full strength. The tensile load was applied at a constant rate of 150 psi/s (1 MPa/s). This rate of loading was chosen to satisfy the requirement that the test has to be completed within 100 seconds. After each pull-off test, the maximum tensile stress and failure mode were recorded. The test is deemed successful when failure occurs in the base material- in this case- the half concrete cylinders as shown in Figure 19.

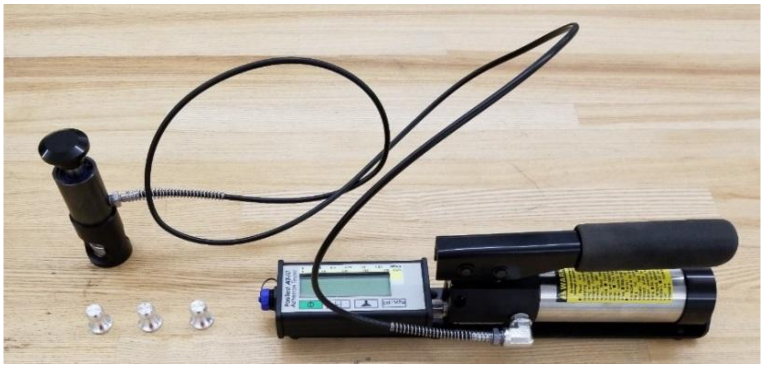

Figure 17. Pull-off PosiTest® AT-M Manual Adhesion Tester

Figure 18. Half cylinder specimen with 20 mm cores (left), 20 mm glued dollies (right)

Figure 19. Pull-off completed tests (left), 20 mmm dollies after pull out tests (right)

Table 20 shows pull out adhesion test results for the three formulations tested in this study. The results show that all three mixes tested for adhesion achieved tensile strength of 200 - 350 psi with the average strength of at least 250 psi.

Table 20 - Pull-off test results for different formulations

Mix	Trial 1	Trial 2	Trial 3	Average
Formulation A, Mix A1*	-	-	-	-
Formulation B, Mix B1-RS	291	228	268	262
Formulation B, Mix B4-QK	204	231	318	251

* Mix A1 samples broke at the edges during drilling and were not tested

Conclusions and Recommendations

The following conclusions were drawn from the investigation of crack repair formulations and injections:

- Workable and flowable crack repair formulations (A, B, and C) for horizontal, vertical, and inclined crack repairs were developed for different crack widths
- Formulations A and B filled 1/8 in (3mm) cracks at least 1 in into the crack depth.
- Formulation A composition included Portland Cement, Micro Fly Ash, very fine sand (100), water and superplasticizer.
- Formulations B used two common repair materials used by NJDOT contractors: CTS Cement ALL and Quikrete Quick Setting Cement with varying water cement ratio and superplasticizer.
- Formulation C was geopolymer based material that included potassium silicate, lithium polysilicate, metakaolin, zirconium sand, iron oxide, and superplaticizer and was suitable for coating micro and nano cracks.
- All crack injection directions require a very tight injection port to avoid leakage due to high injection pressure, especially when injecting vertical cracks.
- Vertical injection of 1/8 in (3mm) wide cracks was achieved up to 12 in high with very tight injection ports.
- Cordless power caulk guns were used for vertical injections and were effective in injecting vertical cracks up to 12 in high.
- Formulation C was more suitable for coating micro/nano cracks. No shrinkage cracking was observed in the coating observed up to 30 days.
- Formulations A and B were capable of sealing thin cracks by gravity flow. Gravity flow depth of penetration was approximately 0.25 in.
- Pull off tests show that Formulations A and B had more adhesion strength than the tensile of the parent concrete material.
- There were difficulties in vertical injection of 1mm cracks more than few inches. This is attributed to the pressure buildup at the injection port.

The Rutgers Team has identified crack repair materials and enhanced their capabilities in the current project. Future implementation would include the following:

- Enhancement of crack filler material to increase flowability and penetration deeper into the cracks and fill longer vertical cracks. Existing research has shown that the depth of filler material is highly variable and difficult to measure.

- Investigate the use of these formulations as ‘coating’ or ‘sealers’ using gravity flow, especially in locations with multiple and widespread cracks. Cores can be taken to measure to measure coating penetration.

LITERATURE REVIEW ON ULTRASONIC TESTING OF CONCRETE

Vertical surface cracks in concrete structures are common defects that can pose significant challenges if not promptly addressed. These cracks often result from factors such as plastic shrinkage during curing, drying shrinkage over time, temperature fluctuations, and inadequate construction practices. Additionally, chemical reactions, overloading, settlement, and corrosion of reinforcement contribute to crack formation. Timely repair is crucial, as these cracks can lead to moisture ingress, causing rebar corrosion and compromising structural integrity. Furthermore, the enlargement of cracks heightens the risk of spalling, posing safety hazards and aesthetic degradation. The resultant need for extensive repairs not only imposes economic strain but also disrupts operations and incurs additional expenses. Thus, repairing surface cracks in the early stages is crucial for effective maintenance strategies. Generally, for large cracks, grout repair methods combined with pressure-injected mechanisms are used to repair deeper cracks. However, the same method is not effective for fixing the initial stages of cracks when the crack depth cannot be interpreted with visual aids. Therefore, it is imperative to characterize the crack patterns (depth and orientation) to optimize the viscosity of repair materials, ensuring that they reach the required crack depths.

Surface cracks in concrete structures are typically too small to significantly impact global dynamics, making wave-based methods the preferred choice for studying crack interaction. Over the years, various techniques have been developed to characterize surface-breaking cracks non-destructively. These include time-of-flight methods (17-19), surface wave transmission method (20-23), and ultrasound diffusion method (25-28). Each methodology offers unique advantages, such as cost-effectiveness, flexibility in sensor placement, and relatively straightforward technical interpretation. However, in field settings, interpreting wave parameters can be challenging due to the heterogeneous nature of concrete. Factors such as reflections from boundaries, mode conversion, and determining wave mode type can affect method accuracy. Additionally, limited accessibility to the concrete surface can constrain sensor placement configurations. Therefore, a thorough understanding of method fundamentals is crucial. This paper will review various studies aimed at characterizing surface-breaking cracks in concrete, summarizing methodologies and providing insights into sensor placement, signal interpretation, and decision-making for crack characterization.

Fundamentals of Wave Propagation Techniques

Stress waves generated in a bulk medium primarily propagate in three modes: longitudinal (P-wave), shear (S-wave), and Rayleigh (R-wave) waves. In a P-wave, particle motion is parallel to the direction of wave propagation, while in an S-wave, particle motion is perpendicular. R-waves exhibit elliptical particle motion, combining longitudinal and transverse components. The velocity of these waves depends on material properties and can be estimated through preliminary experiments supported by theoretical formulations.

In the context of crack assessment, stress waves, typically in the ultrasonic range, are generated in concrete using piezoelectric transducers for signal generation and reception. These propagating wave modes interact with the material, and the presence of a crack has the potential to alter the signal characteristics, such as amplitude, propagation path, phase, and frequency relative to the undamaged state. Figure 20a illustrates the commonly used sensor configurations reported in the literature, namely direct, semi-direct, and indirect arrangements of transducers. Transducers can operate in a pitch-catch setting, with transducers on opposite surfaces, or in a pulse-echo setting, where the same transducer is used for both wave transmission and reception, subject to inspection requirements and surface accessibility restrictions. Kaur et al. (30,31) utilized the pitch-catch method to study the extent of crack depth in concrete beams and conducted amplitude-based monitoring of crack repair using grout-based and bacterial healing of fine cracks. They demonstrated the restoration of P-wave amplitude during crack healing, matching the properties of sound concrete (Figure 20b). In contrast, the pulse-echo approach (32,33) is used to capture reflections from hidden cracks and is predominantly employed in defect imaging techniques. Reflections from defects allow for the estimation of defect location.

Given that concrete is a heterogeneous material, determining wave velocity and identifying wave modes to estimate crack characteristics can be challenging, particularly in field settings. This difficulty arises due to contributions from boundary reflections, mode conversion, and interference from other structural components such as rebar. As a result, various wave propagation methods rely on approximating the travel pathway of stress waves. These methods are primarily divided into time-of-flight, surface wave transmission, and ultrasound diffusion methods, as discussed below.

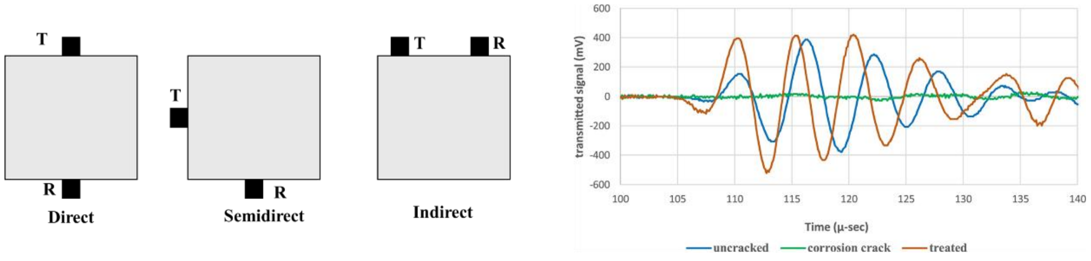

(a) (b)

Figure 20. (a) Different configurations for sensor placement (T: Transmitter; R: Receiver) and (b) Direct wave transmission showing restoration of signal amplitude when the crack is healed (30)

Time of flight (ToF) approach

This method relies on changes in the arrival time of the excited wave between the transmitter and the receiver, as demonstrated in Figure 21a. In a study by Bungay (18), ToF of longitudinal wave transmission is used to estimate the crack depth using eq. 1,

$$d = \left(\frac{X}{T_S}\right)\sqrt{T_C^2 - T_S^2} \tag{1}$$

where d is the crack depth, X is the distance between transducers, T_C and T_S are the ToF in the cracked and sound concrete. However, this method assumes that wave propagation will follow a linear pathway, as approximated in the figure, and that the ultrasonic pulse velocity is constant in both pristine and cracked specimens, which may lead to lower precision in experimental scenarios. Pulse velocity may be affected by moisture or dust entrapped in voids, contributing to changes in pulse velocity.

An extension of this method, mentioned in BS1881: Part 203(17), uses four transducers to eliminate the requirement for preliminary tests in pristine concrete (Figure 21b). It solely relies on the ToF between two indirect measurements with no assumption of travel path. It is recommended to optimize the separation of transducers, generally with a distance of at least twice the wavelength. Eq. (2) represents the modified relation:

$$d = X\sqrt{\frac{4T_1^2 - T_2^2}{T_2^2 - T_1^2}} \tag{2}$$

where T_1 and T_2 are the TOF between transducers spaced at distances X and 2X.

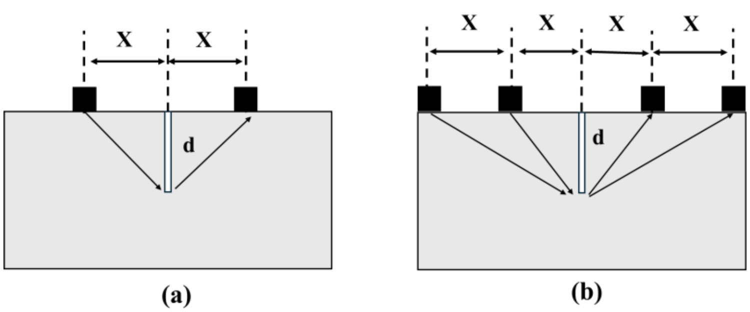

Figure 21. (a) Typical ToF approach using indirect wave transmission and (b) BS: 1881 method

Other models, including the work by Pinto et al. (19) have reported two graphically based methods expanding on the above-discussed models. In the first model (Figure 22a), various ToF readings are taken at different sensor configurations. Under the assumption that pulse velocity is constant in all path lengths, ToF can be correlated with pulse velocity as per eq. (3),

$$T_i = \frac{2L_i}{V} \tag{3}$$

where T_i is the measured TOF at distance X_i from the crack, V is the pulse velocity, and L_i is the half path length corresponding to T_i. Using this principle, eq. (4) can be developed to establish a correlation between the transducer positions and the crack depth,

$$X_i^2 = \frac{V^2}{4}T_i^2 - d^2 \tag{4}$$

Another variation of this method is developed when a crack is located near one of the edges, providing asymmetrical access to either side of the crack. Therefore, the transmitter is fixed in this case, with multiple receivers on one side of the crack (Figure

22b). The first transmitter-receiver pair is equidistant from the crack opening, while the other receivers are moved at fixed increments. Under similar assumptions of constant pulse velocity, spatial positions can be correlated with ToF as in eq. (5), and crack depth can be estimated accordingly:

$$X_i^2 = V^2\left(T_i^2 - \frac{T_1^2}{4}\right) - d^2 \tag{5}$$

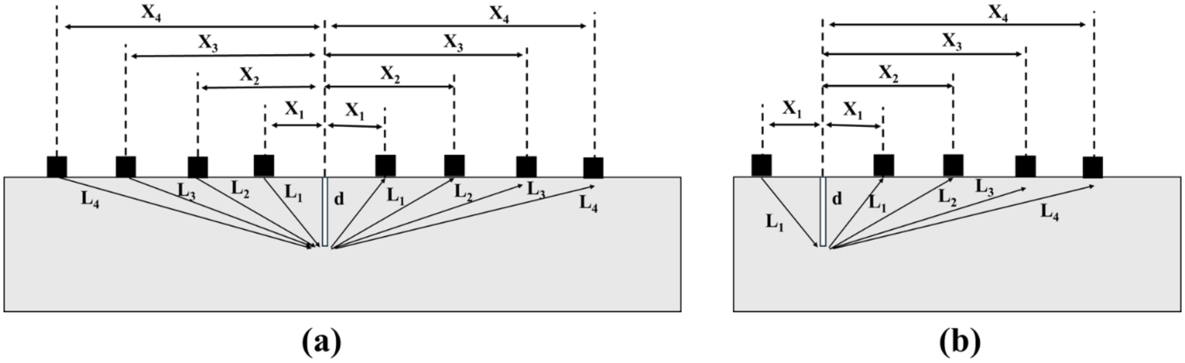

Figure 22. (a) Multiple transducer configuration and (b) transducer configuration when the crack is near the edge

<u>*Surface wave transmission*</u>

Surface wave transmission across a crack can be utilized to estimate crack depth through relative analysis, such as the ratio of spectral transmission amplitude at points B (before the crack) and C (after the crack), as shown in Figure 23a. Since the penetration of R-waves into the material is frequency-dependent, low-frequency components can transmit to point C by traveling below the crack depth, while high-frequency components get filtered out relative to point B. Therefore, by comparing the spectral ratio at points B and C, one can estimate the effect of crack depth. Hévin et al. (21) introduced a cut-off frequency technique to identify the frequency above which a decline in high-frequency components occurs, as illustrated in Figure 23b. The cut-off frequency marks the end of the decline in transmitted energy, with a threshold of 0.5 commonly used to approximate it. A lateral shift in the cut-off frequency towards the lower frequency range is observed with increasing crack depth. Considering that the majority of R-waves travel at approximately one-third of the wavelength in depth, the cut-off frequency can be correlated with crack depth. However, the authors reported errors of up to 15% relative to the actual crack depth.

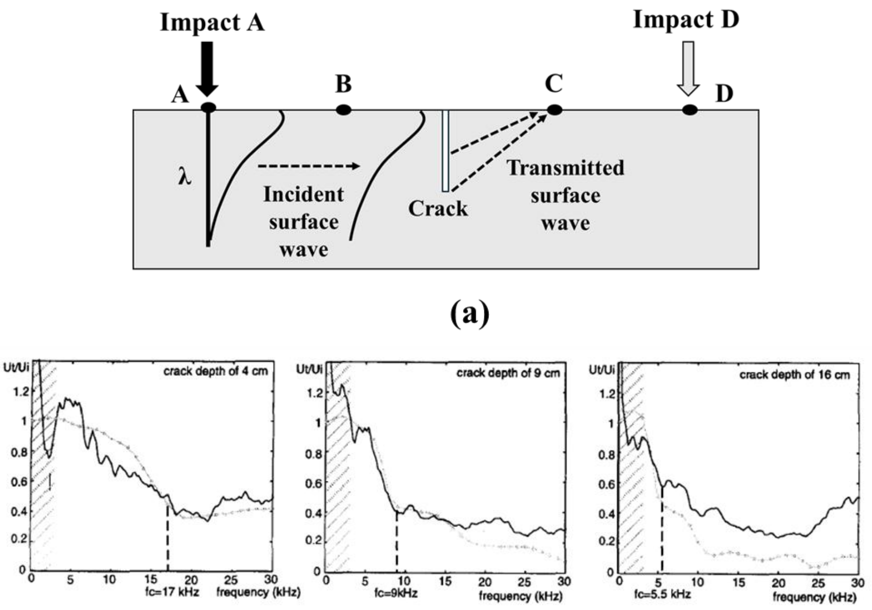

(a)

(b)

Figure 23. (a) Transmission of surface wave across the crack and (b) shift in the cut-off frequency of the spectral ratio (solid/dashed curve – experimental/numerical results) (21)

Ahn et al.(22) presented analytical expressions to evaluate surface wave transmission coefficients from point B to C in the frequency domain. Eq. (6) and (7) represent the frequency domain representation of transmitted signals recorded at points B and C when excitation is at point A:

$$Y_{AB}(f) = S_A(f)\, T_{AB}(f)\, R_B(f) \tag{6}$$

$$Y_{AC}(f) = S_A(f)\, T_{AB}(f) T_{BC}(f)\, R_C(f) \tag{7}$$

where $Y_{AB}(f)$ is the Fourier transform of the A-scan recorded at point B, $T_{AB}(f)$ is the transmission response function for region AB, and $R_B(f)$ represents the frequency response at point B. The same explanation can be translated for eq. (7) with an additional term $T_{BC}(f)$. Similar equations can be developed for responses at B and C when the excitation is at point D,

$$Y_{DC}(f) = S_D(f)\, T_{DC}(f)\, R_C(f) \tag{8}$$

$$Y_{DB}(f) = S_D(f)\, T_{BC}(f)\, T_{DC}(f)\, R_B(f) \tag{9}$$

Eqs. (6-9) can then be utilized to develop the required TRF between B and C as shown in eq. 10 under the assumption that concrete is a homogeneous and isotropic material. A TRF value of 1 represents the absence of a crack, while 0 denotes no transmission between points B and C. This formulation eliminates the effect of transmitter and receiver response functions.

$$|T_{BC}(f)| = \sqrt{\frac{Y_{AC}(f)Y_{DB}(f)}{Y_{AB}(f)Y_{DC}(f)}} \quad (10)$$

The developed transmission response can be used to extract relevant parameters sensitive to the crack depth, and one such approach is the measurement of spectral wave energy as per the eq. (11), where f_L and f_U are the lower and upper bounds of the integration limit.

$$E(d) = \int_{f_L}^{f_U} T_{BC}(f;d)df \quad (11)$$

Considering there is no theoretical formulation available to estimate the crack depth from spectral energy, a ratio-based parameter (*R*) is developed relative to the undamaged concrete as shown in eq. (12), where d_0 denotes zero crack depth. Then, a curve fitting approach is used to correlate *R* and *d* to determine the crack depth. In practice, the determination of integral bounds is crucial for the reliable estimation of the spectral energy.

$$R(d) = \frac{E(d)}{E(d_0)} = \frac{\int_{f_L}^{f_U} T_{BC}(f;d)df}{\int_{f_L}^{f_U} T_{BC}(f;d_0)df} \quad (12)$$

Despite the general decreasing trend in surface wave transmission with increasing crack depth, it is challenging to identify integral bounds using a simple cut-off technique due to the frequency-dependent shape of the transmission envelope, as depicted in Figure 24a. In addition, inherent material and equipment-specific noise content contribute to the overall signal-to-noise (SNR) ratio. Hence, the Signal Consistency (SC) parameter can be used to determine the repeatable frequency range, as per eq. (13), where up to five transmission measurements are taken for the undamaged case:

$$SC(f) = \frac{\sqrt[n]{T_{BC1}.T_{BC2}.....T_{BCn}}}{\left(\frac{T_{BC1}+T_{BC2}+\cdots+T_{BCn}}{n}\right)} \quad (13)$$

where *n* represent the number of repeated cases. *SC* varies from 1 for perfect repeatability and 0 for no consistency in the measurements. Studies have utilized a *SC* value of greater than 0.99 to obtain high consistency in the measurements. This approach allows for the reliable extraction of integral limits. Figure 24b and 24c show the signal consistency index and the selected integral limits for surface wave transmission observed in the study by Shin et al. (20). This approach allowed them to establish a correlation between the spectral energy ratio and the crack depth as shown in Figure 24d. It is important to note that this study relies on comparison with the undamaged state of concrete.

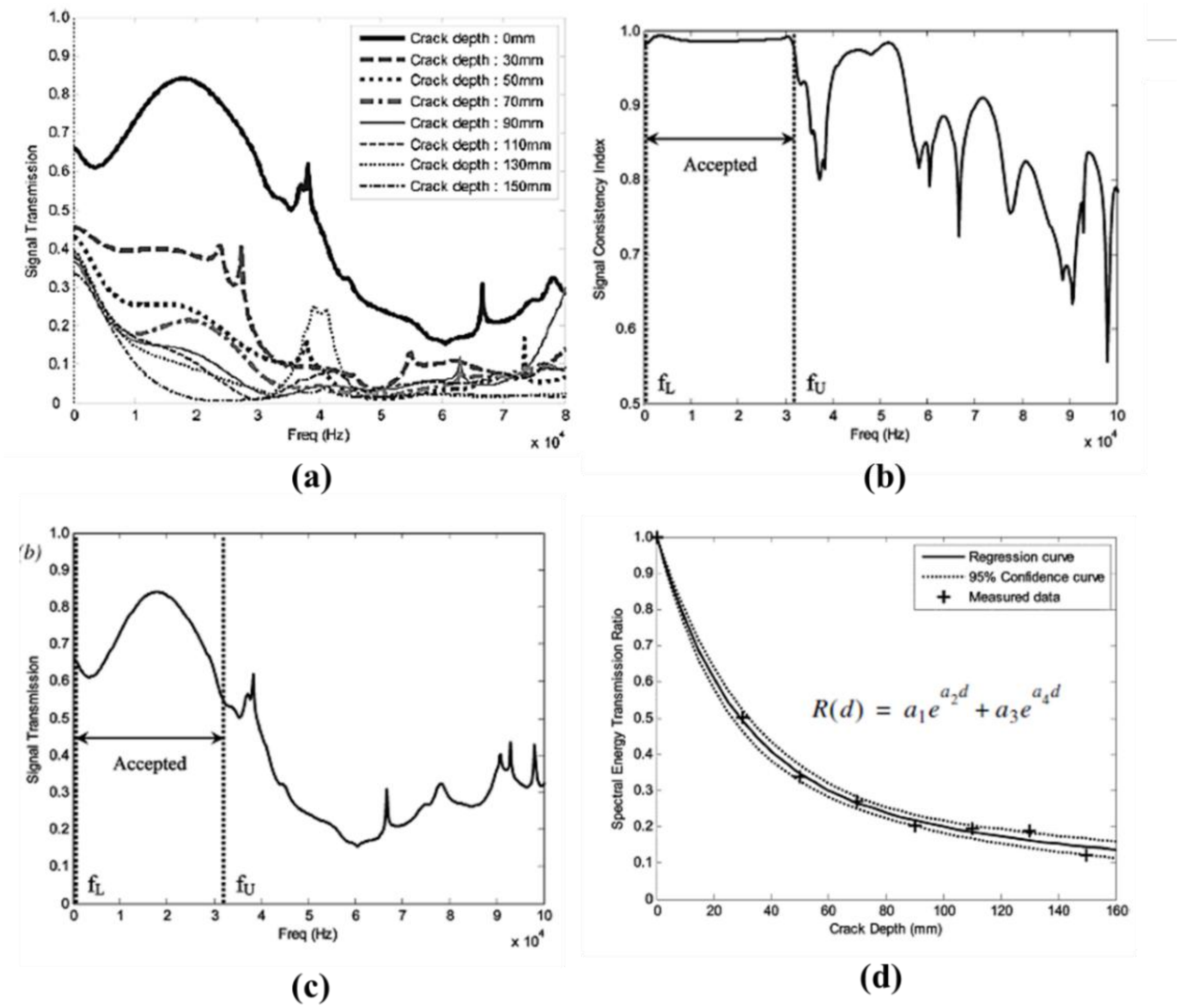

Figure 24. (a) Dependency of transmission function shape on frequency, (b) signal consistency variation of transmission function in undamaged case, (c) finalized integral limits based on signal consistency index, and (d) Correlation between spectral energy ratio and crack depth (20)

Ultrasonic Diffusion Approximation

When stress waves propagate through a heterogeneous material such as concrete, they can be approximated as a superposition of ballistic and diffusive components. When the wavelength is larger than the aggregate size, the ballistic component dominates the signal transmission. This component remains unscattered and coherent with the incident source signal. However, when the wavelength is similar to or smaller than the aggregate size, scattering becomes dominant before the wave arrives at the receiver, and the process can be captured as a diffusive process. The diffusion process occurs over a longer time scale than the propagation of the coherent part and is both spatially and temporally incoherent with the incident source signal. This process can be approximated by modifying the heat transfer equation with an additional dissipation term, as shown in eq. (14) (34):

$$\frac{\partial < E(x,t,f) >}{\partial t} - D\Delta< E(x,t,f) > +\sigma < E(x,t,f) \geq E_0(x,t,f)\delta(x_0)\delta(t_0)\forall x \in \mathfrak{B} \tag{14}$$

where E is the spectral energy density, E_0 is the spectral source energy density at x_0 and t_0, D is the frequency-dependent diffusion coefficient, σ is the dissipation rate, and the equation shows diffusion of spectral energy in a linear elastic body $\mathcal{B}$. The diffusion coefficient D is a property of material microstructure, where a higher value of D indicates greater diffusion of energy in that material.

The σ term is not influenced by the scattering. Anugonda et al. (26) utilized a 1-D solution to investigate the diffusion process, as shown in eq. (15 and 16), establishing a linear regression fit equation. The curve-fitting process of this equation enables the estimation of σ observed as the exponential decay with time and $z^2/4D$ term denotes the arrival time for maximum energy.

$$< E(z,t) \geq E_0 \frac{1}{\sqrt{2\pi Dt}} e^{-\frac{z^2}{4Dt}} e^{-\sigma t} \tag{15}$$

$$\ln(< E(z,t) >) + 0.5\ln(t) = C_0 - \frac{z^2}{4Dt} - \sigma t \tag{16}$$

In practice, the incoherent diffusion component leads to rapid spatially fluctuating phase and amplitude, resulting in phase cancellation upon averaging (35). This phenomenon is particularly pronounced with large-diameter transducers, making smaller contact area transducers preferable for capturing such components. Figure 25 illustrates the typical energy diffusion profile in concrete when different frequency excitation sources (300 kHz and 500 kHz) are used. It is evident that higher frequency energy components exhibit relatively greater diffusion.

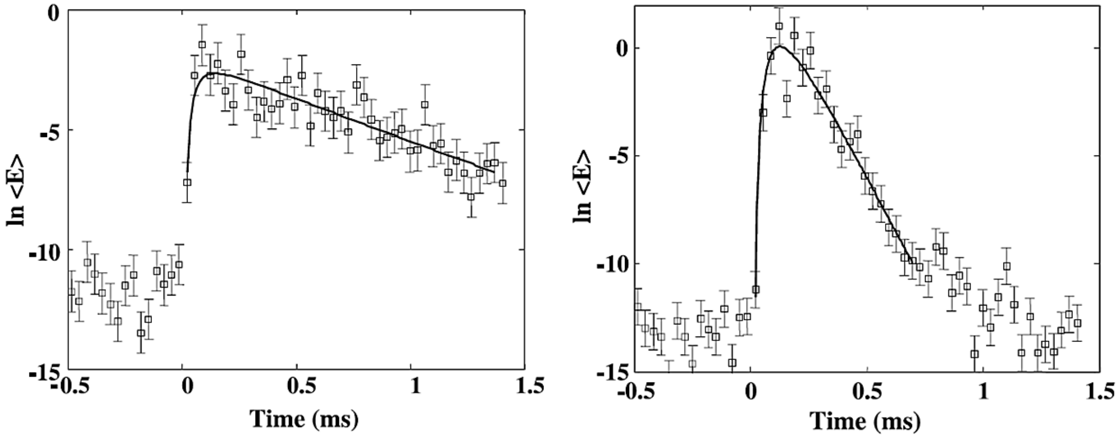

(a) (b)

Figure 25. Energy diffusion profile in concrete for excitation of (a) 300 kHz and (b) 500 kHz signal (26)

In the context of crack detection, the same diffusion principle applies when the wavelength of the surface wave becomes comparable to the crack depth, initiating a diffusion process, as summarized in the study by In et al. (34). They described a 2-D solution of Eq. 14 using a simplified bounded plate approximation of negligible thickness to estimate *D* and *σ* through a curve fitting approach,

$$< E(x,y,t) \geq \left\{ \begin{array}{l} 1+\sum_{n=1}^{\infty}\sum_{m=1}^{\infty} 4\,cos\left(\frac{n\pi x_0}{l}\right) cos\left(\frac{m\pi y_0}{p}\right) \times cos\left(\frac{n\pi x}{l}\right) cos\left(\frac{m\pi y}{p}\right) e^{-D\left[\left(\frac{n\pi}{l}\right)^2+\left(\frac{m\pi}{l}\right)^2\right]t} + \\ \sum_{n=1}^{\infty} 2\,cos\left(\frac{n\pi x_0}{l}\right) cos\left(\frac{n\pi x}{l}\right) e^{D\left[\left(\frac{n\pi}{l}\right)^2\right]t} + \sum_{n=1}^{\infty} 2\,cos\left(\frac{n\pi y_0}{p}\right) cos\left(\frac{n\pi y}{p}\right) e^{D\left[\left(\frac{m\pi}{p}\right)^2\right]t} \end{array} \right\} \times E_0 e^{-\sigma t} \tag{17}$$

where x_0 and y_0 represent the coordinates of the stress wave source, and *l* and *p* denote the dimensions in the x and y directions, respectively.

While studying the interaction of surface waves with cracks, various unwanted factors might influence signal analysis, such as mode conversion during crack interaction and reflections from boundaries. Lin et al. (36) and others addressed this challenge by utilizing shear horizontal (SH) ultrasonic waves for inspection and investigating ultrasound diffusion. They introduced the concept of two-wave travel time (TWTT) to estimate the arrival of diffracted SH waves from the crack tip, as illustrated in Figure 26. In sound concrete, TWTT represents the arrival time of the reflected SH wave from the bottom surface and can be used to estimate the velocity of the SH wave. In the absence of a crack (Figure 26a and 26c), the transmitted signal exhibits two main envelopes: one represents the direct wave transmitted between the source and the receiver, followed by the reflected envelope from the bottom surface. However, in the presence of a crack (Figure 26b and 26d), the transmitted signal includes a diffracted envelope from the crack tip instead of the direct wave, along with the reflected envelope from the bottom surface. The arrival time of the diffracted wave can be utilized to estimate the crack depth using eq. (18),

$$d = \sqrt{\left(\frac{V.TWTT}{2}\right)^2 - \left(\frac{X}{2}\right)^2} \tag{18}$$

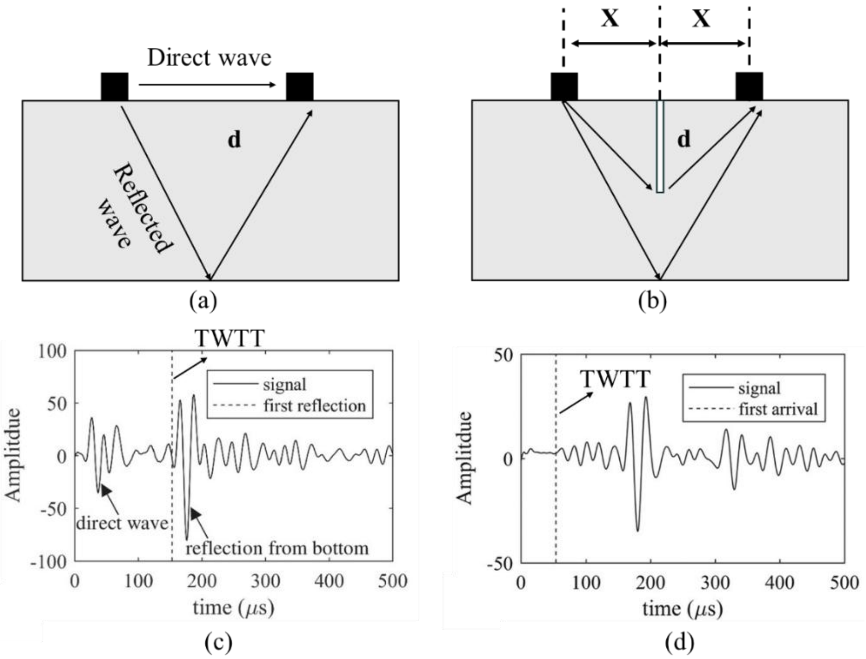

(a) (b)

(c) (d)

Figure 26. (a, b) Concept figures showing the effect of crack on the wave propagation and transmitted signal in (c) undamaged specimen and (d) cracked specimen. (36)

Quiviger et al.(27,28) and others(29) introduced another damage parameter called ATME (arrival time of maximum energy), based on eq. 16, which has been found to be sensitive to crack depth, as illustrated in Figure 27. This parameter is estimated through curve fitting on the energy spectra recorded by the receiver (Figure 27a). However, the methodology appeared to be efficient only for cracks represented by notches in experimental conditions where the crack faces are reasonably open (Figure 27b). It was not found to be sensitive to cases where cracks were fabricated through loading tests, resulting in cracks with fine tips behaving as closed cracks under normal conditions. Both the TWTT and ATME-based approaches suffered from such limitations

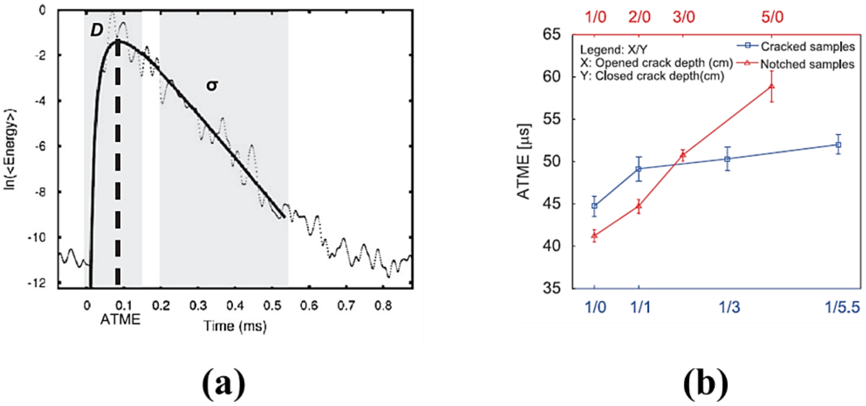

(a) (b)

Figure 27. (a) The concept of identifying ATME and (b) The variation of ATME with crack notched and cracked samples

Payan et al.(25) extended their investigation to micro-cracks by inducing closing and opening phenomena of micro-cracks under additional low-frequency vibrations. Figures 28a and 28b illustrate the experimental profile of such an investigation, where a new damage parameter called ATME (arrival time of maximum energy) is developed by calculating the energy content of the transmitted signal within a predefined time and frequency window. The ATME generally decreases due to diffused ultrasound when the fine crack is open. Experiments correlating ATME with dynamic vertical displacement show a hysteresis response, where ∆t represents the maximal ATME excursion during a cycle (Figure 28c). The value of ∆t is found to be linearly correlated with the crack depth (Figure 28d). The methodology may be subject to the morphology of the crack and its response to the dynamic load in practical scenarios; hence, imaging methods supporting the above inspection may become useful.

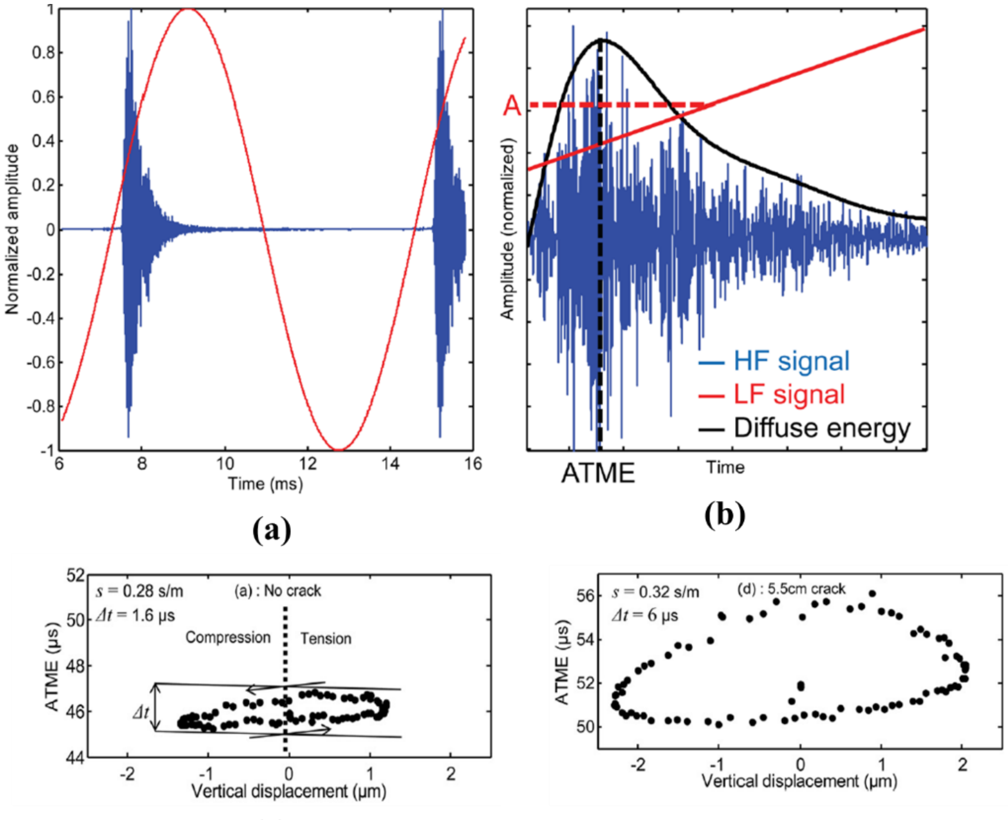

(a) (b)

(c) (d)

Figure 28. (a) Experimental high frequency (HF) and low frequency (LF) signals, (b) ATME and LF amplitude variation, and change in ∆t for (c) no crack and (d) 5.5 cm crack (25)

Vertical Crack Imaging

Chang et al. (37) utilized an array of transducers to capture the wave travel time diffracted by the crack tip and employed this information to back-calculate a 3-D image highlighting the tip of a vertical crack. The underlying imaging principle was based on the migration theory, where the source and receiver locations around the crack were set as foci of the ellipse equation (eq. 19),

$$\sqrt{(x-x_S)^2+(y-y_S)^2+(z-z_S)^2}+\sqrt{(x-x_R)^2+(y-y_R)^2+(z-z_R)^2}=V.T \quad (19)$$

where (x, y, z), (x_S, y_S, z_S), (x_R, y_R, z_R) represent the Cartesian coordinates of the potential crack tip, source, and receiver locations, respectively. In this equation, *V* denotes the longitudinal wave speed in the medium measured in its undamaged condition, and *T* represents the arrival time of the first diffracted wave. By creating multiple ellipses using different source and receiver locations, their interaction will effectively highlight the tip of the crack. Figure 29 illustrates the concept of imaging and presents a sectional image highlighting the crack tip.

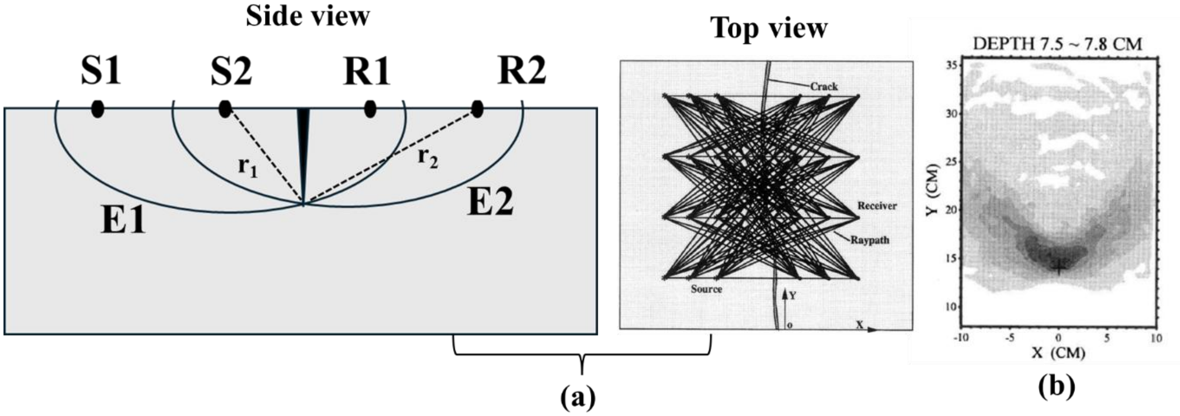

Figure 29. (a) Schematic showing the imaging concept in 2-D, and (b) sectional image highlighting the crack depth (darker region) (37)

Kimoto et al. (38) employed two distinct focusing techniques, namely Synthetic Aperture Focusing Technique (SAFT) and Computed Time-Reversal Focusing Technique (TRFT), to estimate the crack depth using SH-waves. SAFT is a beamforming technique that generates crack images through synthetic focusing of the recorded waveforms. In the time domain, eq. (20) illustrates the implementation of SAFT.

$$S(x;\delta)=\sum_{i,j} v_{ij}\left(\frac{|x-x_i|}{c}+\frac{|x-x_j|}{c}+\delta\right) \quad (20)$$

where *x* represents the field point, c is the wave velocity, and *δ* represents the offset of the origin of the temporal axis, compensating for the signal delay caused by the measuring device. The term v_{ij} denotes the recorded A-scans in the pitch catch setting between x_i and x_j, both are on the opposite side of the crack. Eventually, the summation over the chosen indices *i* and *j*, and careful selection of *δ* will maximize the signal intensity *S* at the crack tip.

On the contrary, in the TRFT approach, the time-reversed wavefield focused on the crack tip is utilized to create images. This is achieved by introducing a new time variable τ as $t = t_i - \tau$, where t_i being a sufficiently large constant ensuring $v_{ij}(t)$ is approximately zero for t greater than t_i. Hence the reversed waveform $\{v_{ij}(t - \tau)\}$ is employed to excite the *jth* element, and the back propagating field from array elements can be written as eq. (21),

$$F_i(x,\tau) = \sum_j v_{ij}\left(t_i - \tau + \frac{|x_i - x_j|}{c}\right) \tag{21}$$

The crack tip can be identified as the focus point of simultaneously superimposed time-reversed focusing fields. This is done by choosing t_i as,

$$t_i = T_d + \frac{|x_i - x_{tip}|}{c} \tag{22}$$

where T_d is constant and independent of *i.* The superimposed field can be written as eq. (23),

$$F_i(x,\tau;x_{tip}) = \sum_{i,j} v_{ij}\left(T_d - \tau + \frac{|x_i - x_{tip}|}{c} + \frac{|x_j - x|}{c}\right) \tag{23}$$

For more detailed information on the SAFT and TRFT methods, the following publications can be referred to. Figure 30 displays the SAFT and TRFT images of the same crack, showcasing the successful application of both methods in locating the crack tip. However, the authors reported that TRFT outperformed the SAFT method, particularly when the cracks were partially closed under dynamic loading.

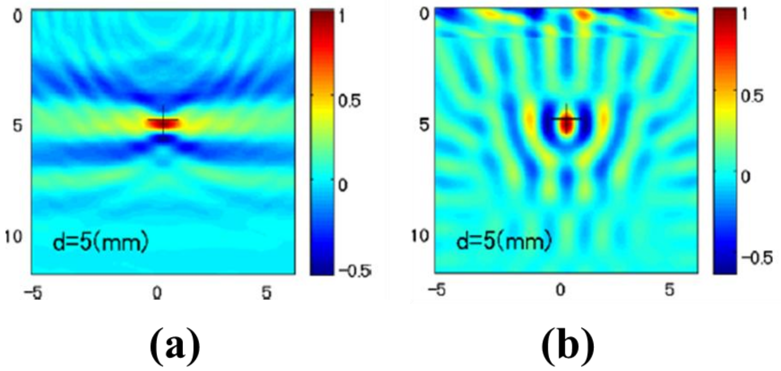

Figure 30. Crack tip imaging using (a) SAFT and (b) TRFT method (38).

Kuchipudi et al. (39) and others (40) further refined SAFT with the half-skip time focusing method (HSTFM), which incorporates target-scattered signals after being reflected from the backwall. It assumes that the reflection from the backwall to the receiver is analogous to the travel path to the virtual sensors represented with asterisks, as depicted in Figure 31a. In this approach, image construction involves utilizing the two skip paths (T*-R-p and T-p-R*) and numerically estimating the intensity at these paths using eq. (24 and 25).

$$\text{T*-R-p: } I_p = \sum_{T=1}^{n-1}\sum_{R=T+1}^{n} A^{TR}\left(t_{HSTFM}\frac{S_{T1}+S_{T2}+S_R}{V}\right) \tag{24}$$

$$\text{T-p-R*: } I_p = \sum_{T=1}^{n-1}\sum_{R=T+1}^{n} A^{TR}\left(t_{HSTFM}\frac{S_T+S_{R1}+S_{R2}}{V}\right) \tag{25}$$

where *V* is the wave velocity. Elliptical contours (Figure 31b) are subsequently generated, with one focus at the actual sensor location and the second focus at the hypothetical sensor location. The interaction of these ellipses emphasizes the position of the scattering point. As the scattering intensity increases at the crack tip location, it serves as an approximation of the crack depth. Figure 31c represents the crack imaging obtained using this method.

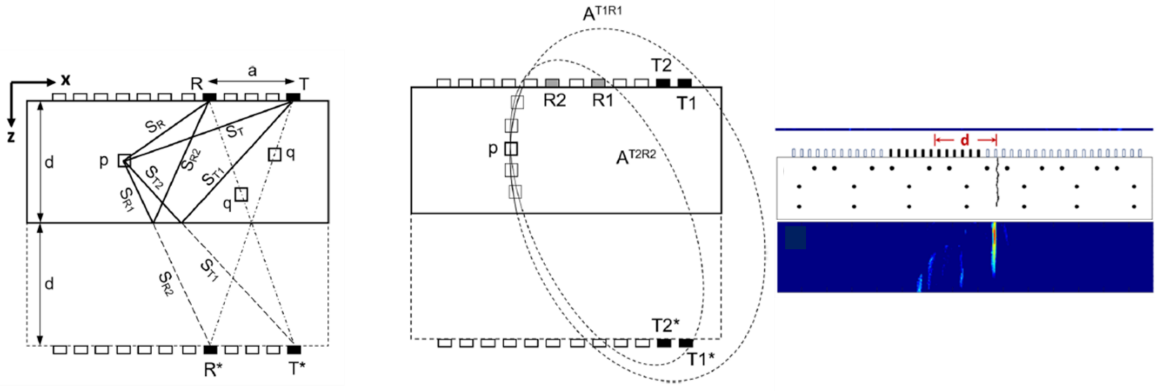

(a) (b) (c)

Figure 31. (a) Schematic showing the half-skip time focused method and (b) ellipse profiles showing scattering ‘p’ at its interaction, and (c) image showing the extent of the crack.

Another imaging technique called stack imaging of spectral amplitudes based on impact-echo (SIBIE)(24,41,42) is based on the extraction of resonance frequencies generated during impact echo tests. The test cross-section is divided into square elements (Figure 32a), and peak frequencies due to reflection at each element are calculated using eq. (26), regardless of whether resonance frequencies occur or not.

$$f_2 = \frac{c_P}{r_2} \text{ and } f_R = \frac{c_P}{r_1 + r_2} \tag{26}$$

where f_2 and f_R are two resonant frequencies, r_1 and r_2 are distances relative to the impact source and receiver, and c_P is the P-wave velocity. The reflection intensity at each element is calculated by summing the two frequencies, resulting in a stack image being created for each element. Eventually, a 2-D map (Figure 32b) of reflection intensities at each element is presented, resulting in a contour where the location of the highest intensity marks the presence of the crack tip, as shown in the figure. It is crucial to maintain a minimum grid size (Δx) as per the following equation,

$$\Delta x = \frac{c_P \Delta t}{2} \tag{27}$$

where Δt is the sampling time period of the recorded waveform.

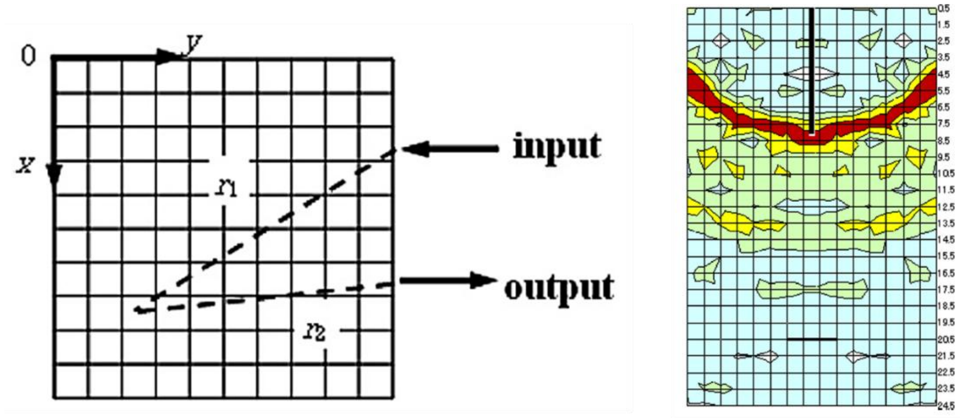

(a) **(b)**

Figure 32: (a) Cross section divide into meshes and (b) SIBIE map for vertical crack (24).

ULTRASONIC TESTING ON CONCRETE CRACK AND REPAIR

Laboratory Experiment Setup and Specimen

UT is employed to estimate the depth of surface-breaking cracks and to monitor their repair process. To develop preliminary insights, experiments were conducted on a readily available concrete brick, where vertical cracks of varying depths were fabricated, and ultrasonic signal transmission across the cracks was analyzed. Different signal frequencies were tested, and efforts were made to establish potential correlations between crack depth and signal features. Key parameters such as amplitude comparison, time of flight, and the correlation index between pristine and damaged or repaired specimens were utilized to interpret wave–specimen interactions.

Figure 33 shows the experimental setup for the UT, which consists of a function generator, a high-voltage power amplifier, an oscilloscope, and a PC. The input signal of desired characteristics (shape, frequency, and amplitude) is generated using the function generator, which is then amplified through a power amplifier. The amplified signal is fed to the transmitter (13 mm × 13 mm × 0.96 mm piezoceramic transducer), which converts the electric signal into corresponding mechanical stress waves that propagate into the specimen. The chosen specimen for this study is an 8 in. × 4 in. × 2 in. concrete brick. The propagating stress wave is recorded using an identical transducer (receiver), which converts the stress waves back into electrical signals. These signals are digitized using the oscilloscope, which is then stored in the personal computer for analysis. The separation between the two transducers is maintained at seven inches, for all the specimens considered in this study. This will allow reasonable interaction between the ultrasonic signal and the specimen.

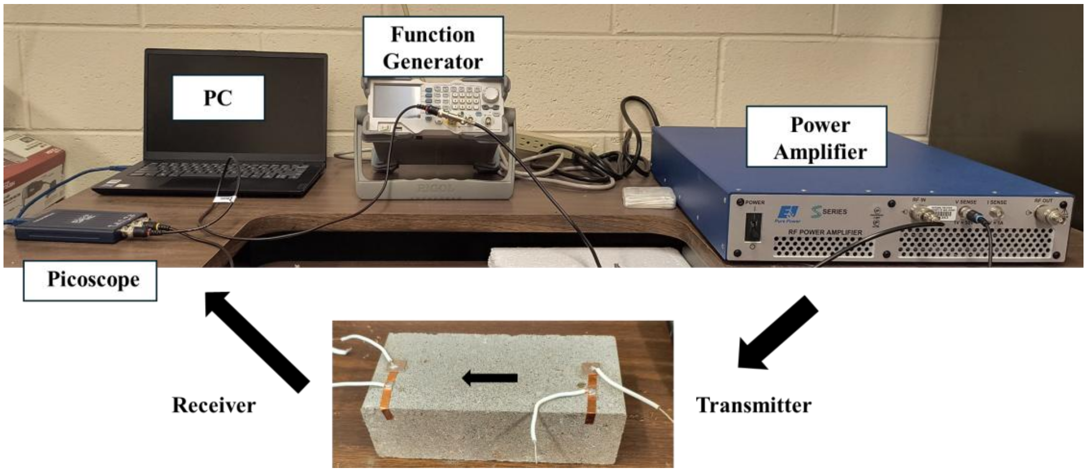

Figure 33. Experimental setup

Laboratory Experiment Results

<u>*Preliminary observations*</u>

A 3-cycle cosine wave function modified by the Hanning windowed function is used as the input signal. This shape of the signal is considered to optimize the signal recognition in the transmitted waveform and achieve higher energy distribution around the central excitation frequency. Different inspection frequencies were tested for the analysis, ranging from 50 kHz to 150 kHz. This report discusses the observations made from the 70 kHz and 140 kHz signals, as they offered reasonable strength in the transmitted signal across the cracks of different depths. Frequencies lower than 70 kHz were ignored as these resulted in potential overlap between the transmitted and the recorded signal. Figure 34 shows a typical example of a sample in the pristine and damaged condition, where the cracks are fabricated with high RPM cutting steel blades. Cracks are fabricated halfway between the transmitter and the receiver.

(a) (b)

Figure 34. (a) Pristine specimen, and (b) cracked specimen

Figure 35 a,b shows the signal transmission across a 1.5" deep crack for 70 kHz and 140 kHz signals. When compared with the transmitted signal in pristine condition, the presence of a crack affected the arrival time of the first discernible peak in the signal and the overall strength (amplitude) of the signal. Although it is evident that the arrival time delay is due to a crack (Figure 35c,d), it remained challenging to pick the exact peak whose time can be correlated to the crack depth. Furthermore, it remains subjective to pick time intervals that demonstrate the signal decays corresponding to the crack depth. In addition to the crack presence, other potential factors for the signal attenuation can be associated with destructive interference between scattered waves from the crack boundaries and the incoming transmitted waves. Ideally, certain quantitative parameters that can better capture the effects of the crack on signal transmission are desired.

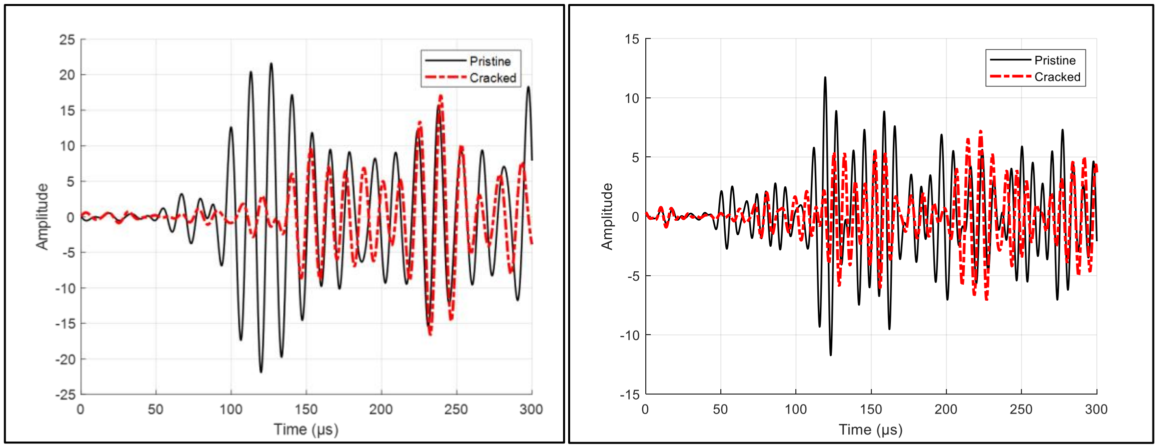

(a) (b)

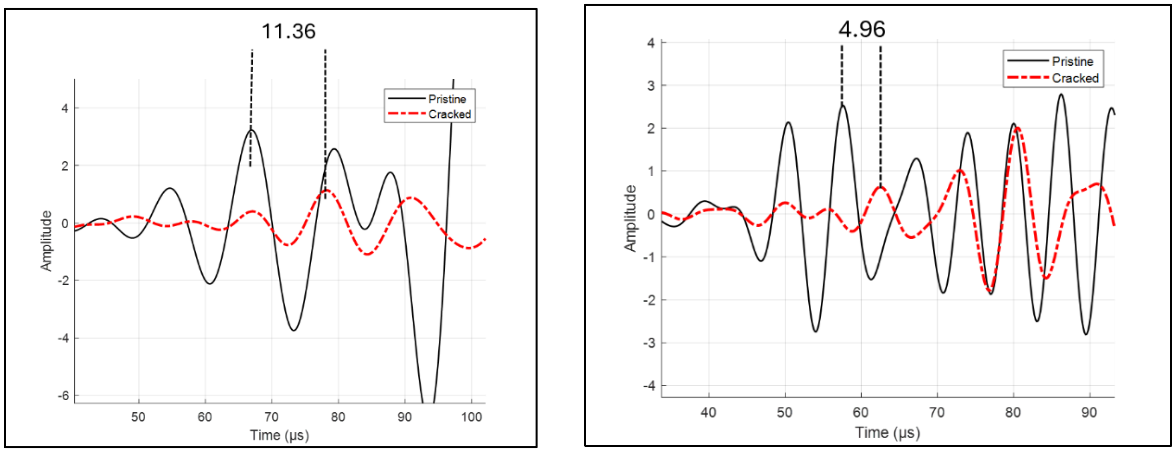

(c) (d)

Figure 35. Transmitted signals relative to the signal transmission in the specimen obtained with (a) 70 kHz and (b) 140 kHz signals, and their corresponding shift in the time of arrival of their first peaks at (c) 70 kHz and (d) 140 kHz inspection. The specimen has a crack depth of 1.5".

Effect of crack repair on transmitted signal

To evaluate the effectiveness of the crack repair, the cracks are filled with the repair fluid, and the UT is performed on it one day after the repair. To ensure that the repair liquid reaches the bottom of the crack, additional efforts were made. A hole is drilled at one end of the crack, which extends to the bottom of the crack. Then the repair solution is pushed into the hole using a syringe. The results of crack repair for a 1.5" crack depth are discussed in this section. Figure 36 shows the repaired specimen, and it can be observed through visual inspection that the repaired material has reached the bottom of the crack depth. However, it would be an overestimation to state that the crack has filled completely to become relatively equivalent to the pristine state of the specimen.

Figure 36. Repaired specimen

Figure 37a,b shows the comparison of the transmitted signal in the repaired state relative to the pristine signal. Preliminary observation shows the strength of the signal is recovered for both the 70 kHz and 140 kHz inspection, especially for the initial envelopes in terms of amplitude comparison and reasonable overlapping of the peaks. Some peaks showed slightly higher energy, which can be due to mismatched material properties between the pre-made concrete bricks and the repair solution. In the context of time-of-flight (Figure 37c,d), the arrival time of the first main peak becomes reasonably similar to the transmitted signal in the pristine state. It hints towards an efficient repair material for completely filling the crack.

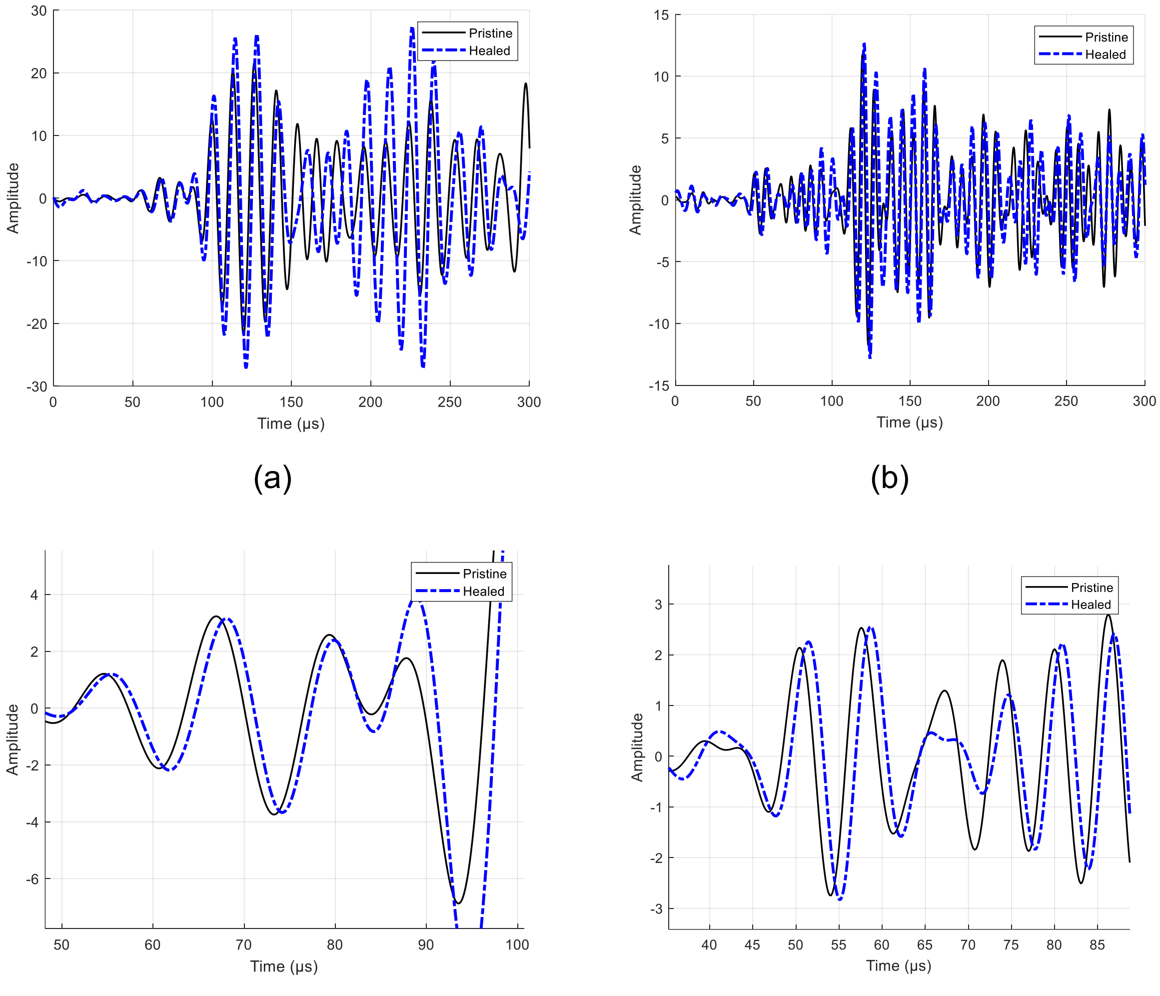

(a) (b)

(c) (d)

Figure 37. Transmitted signal in the repaired specimen relative to its pristine state for (a) 70 kHz (b)140 kHz inspection, and time of arrival of (c) 70 kHz signal and (d) 140 kHz signal.

As observed in Figure 35, the crack resulted in a decay in signal amplitude, a time shift in the transmitted signal, and an emergence of the new mode shapes. When repaired as shown in Figure 37, the recovery in the transmitted amplitude, signal shape, and arrival time became evident. It becomes critical to quantify such observations to estimate the effect of crack depth and the crack repair on the signal transmission. To expand on the dataset, we have considered additional specimens with the crack depth of 1" and 0.5".

The decibel drop method is used to capture the signal decay across different time windows of the recorded signal to capture the amplitude-drop trend. For the pulse-echo technique, it is widely accepted to apply a threshold of 6 dB drop at the crack edges, which highlights the potential length of the crack; however, no such threshold is defined for signal transmission-based investigation. For now, a threshold of -6 dB is accepted for reference in this investigation. Different time windows of 50 µs length between 50 µs and 250 µs are used for this analysis. This approach of using distinct time windows instead of a single longer time window was considered to exclude the dominant contribution from the unwanted reflections from the specimen boundaries (typically in time windows after a few initial signal envelopes). Such reflections remain subjective to the size of the specimen and offer no meaningful insights if not separated from initial peaks. Despite such challenges, these are still included in the current analysis, as it is desired that once the crack is repaired, such reflections will be restored relative to the signal transmission in pristine conditions. These will predominantly be present in the time window after 150 µs. Eq. (28) shows the calculation of the decibel drop method.

$$dB\ drop = 20\log\left(\frac{A_{cracked}}{A_{pristine}}\right) \quad (28)$$

where *A* is the amplitude of the signal energy in the selected time window, calculated as per eq. (29),

$$A = \sum_{t_i}^{t_f} X(t)^2 \quad (29)$$

where *X*(*t*) is the signal amplitude at the specific time instant between initial and final time bounds represented as t_i and t_f.

Another considered parameter is the similarity index between the cracked/ repaired state of the specimen relative to its pristine state. This is captured by estimating the correlation coefficient between the two states as per eq. (30),

$$C(A,B) = \frac{1}{N-1}\sum_{i=1}^{N}\left(\frac{A_i-\mu_A}{\sigma_A}\right)\left(\frac{B_i-\mu_B}{\sigma_B}\right) \quad (30)$$

where *C* is the correlation coefficient, A and B are the pristine and the cracked/repaired signal in the specific time windows, μ and σ are the mean and standard deviation of the signals. This coefficient is a measure of linear dependence between two random variables, and the values remain between -1 and +1, where a negative value represents a negative correlation between the two variables. Correlation coefficients can be effectively utilized to quantify the similarity between the transmitted ultrasonic signals before and after crack formation or repair. In the context of this study, using the correlation coefficient as a measurement parameter allows the evaluation of both amplitude changes and waveform distortions induced by surface-breaking cracks. A high correlation value close to +1 indicates minimal alteration in the signal transmission, whereas a lower correlation reflects significant signal modification due to scattering, mode conversion, or time delays introduced by the crack. Thus, the correlation coefficient serves as a sensitive and compact metric to capture crack-induced changes in the ultrasonic response under identical inspection settings.

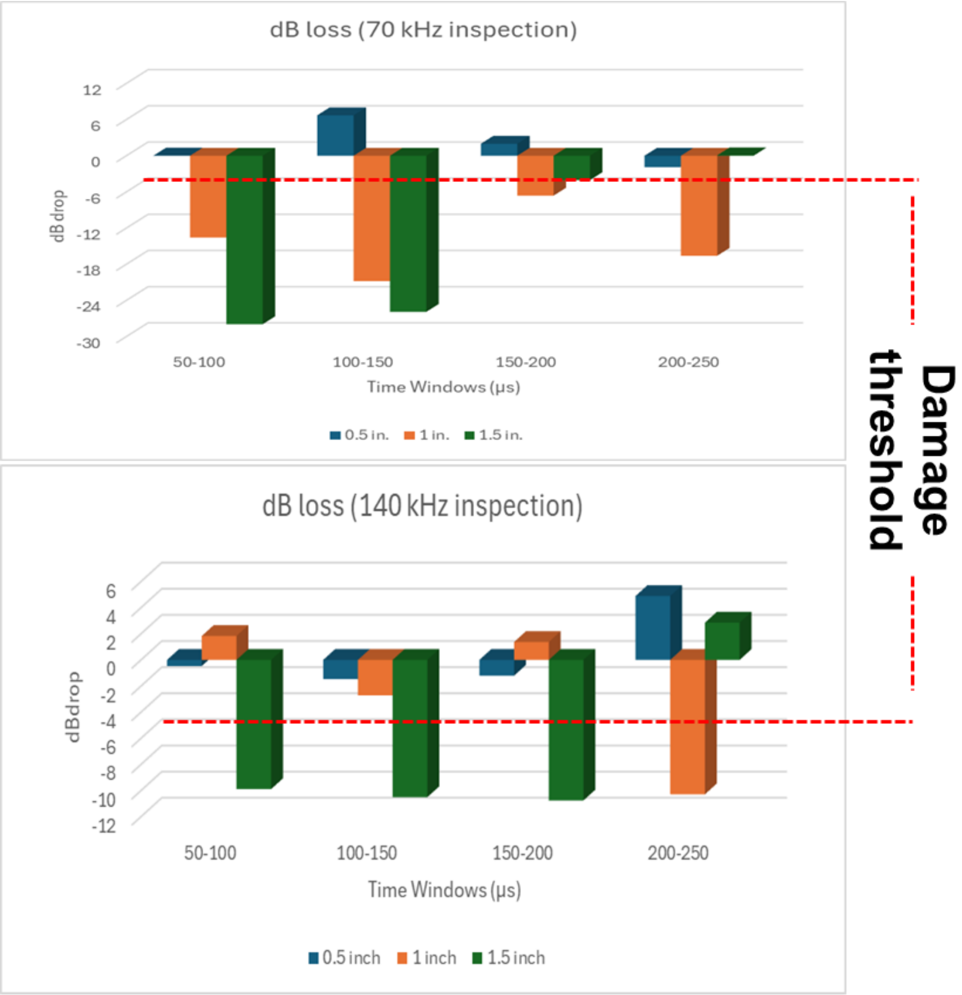

Figure 38. dB drop trend across different crack depths obtained using (above) 70 kHz and (below) 140 kHz signals.

Figure 38 shows the dB drop for the specimens with different crack depths for 70 kHz and 140 kHz inspection. For 70 kHz, the dB drop loss is greater than 6dB for most windows (50% or greater) at 1" and 1.5" deep cracks. On the contrary, the 140 kHz signal only showed a drop of 6dB and above only 1.5 in. deep cracks. Although 140 kHz shear waves experience higher intrinsic attenuation in concrete, the observed amplitude decay across the cracked specimen was greater at 70 kHz. This behavior is attributed to the stronger interaction of the longer-wavelength 70 kHz wavefront with the crack geometry, resulting in enhanced scattering and energy redistribution. In contrast, the 140 kHz wave may partially bypass or diffract through the defect more effectively, or benefit from multiple wave path contributions, reducing the apparent transmission loss due to the crack.

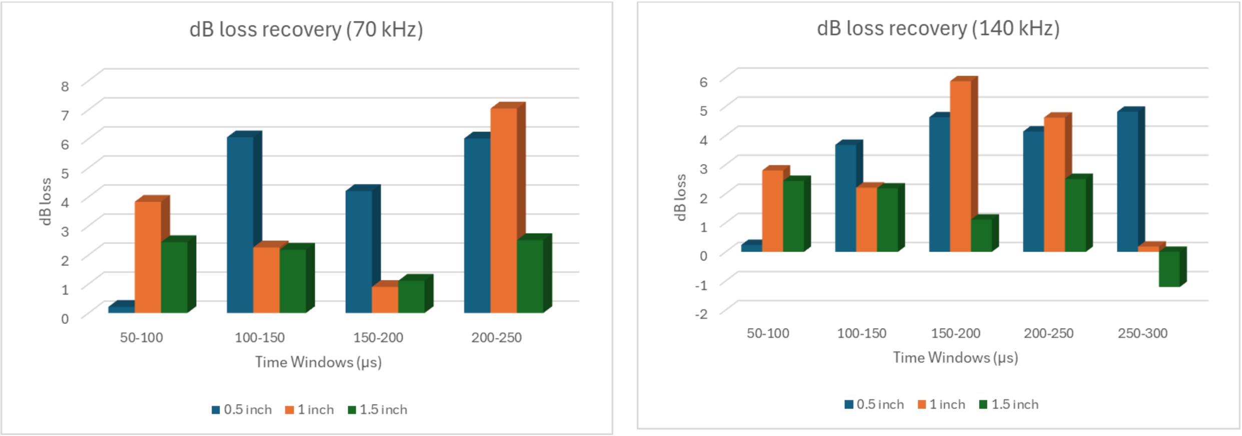

(a) (b)

Figure 39. Recovery trend in dB loss across different crack depths obtained using (a) 70 kHz and (b) 140 kHz signals.

Figure 39 shows the recovery trend in the signal strength across different time windows. It can be observed that, irrespective of the inspection frequency, all the relative amplitudes showed positive dB gains for most windows. It highlights the effects of repaired cracks on the signal transmission. Ideally, the repaired specimen should have dB loss close to 0; however, the positive gains might be a result of a property mismatch between the repair material mix and the concrete mix of the ready-made brick. It is possible that the repair mix has a higher elastic modulus than the brick mix.

Figure 40 shows the correlation coefficient trends for different crack depths before and after the crack repair for a 1.5". deep crack. It is expected that the relative correlation coefficient of different windows should be closer to +1 after repair. Overall, the effect of the crack is evident across all the windows as the correlation coefficient was significantly lower for both frequencies. The overall increase in the correlation coefficient across the majority of time windows is evident in the figure, especially in the first couple of time windows, where initial meaningful wave modes exist. Despite being less relevant to interpretable wave modes, the last two windows are considered in the analysis to capture the similarity in the overall signature of the wave transmission. These windows will capture the effect of boundary reflections and multiple reverberations of multiple scattered modes.

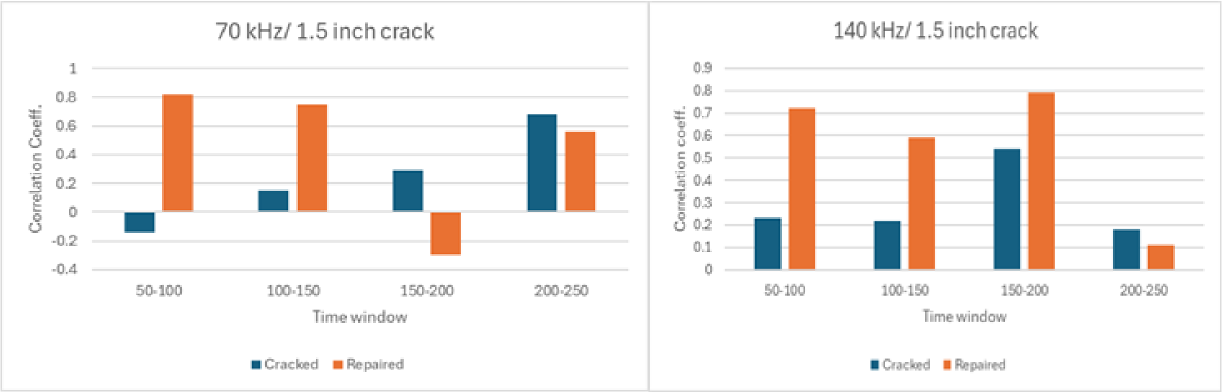

(a) (b)

Figure 40. Correlation coefficient of specimen with 1.5 in. deep crack obtained using (a) 70 kHz and (b) 140 kHz signals.

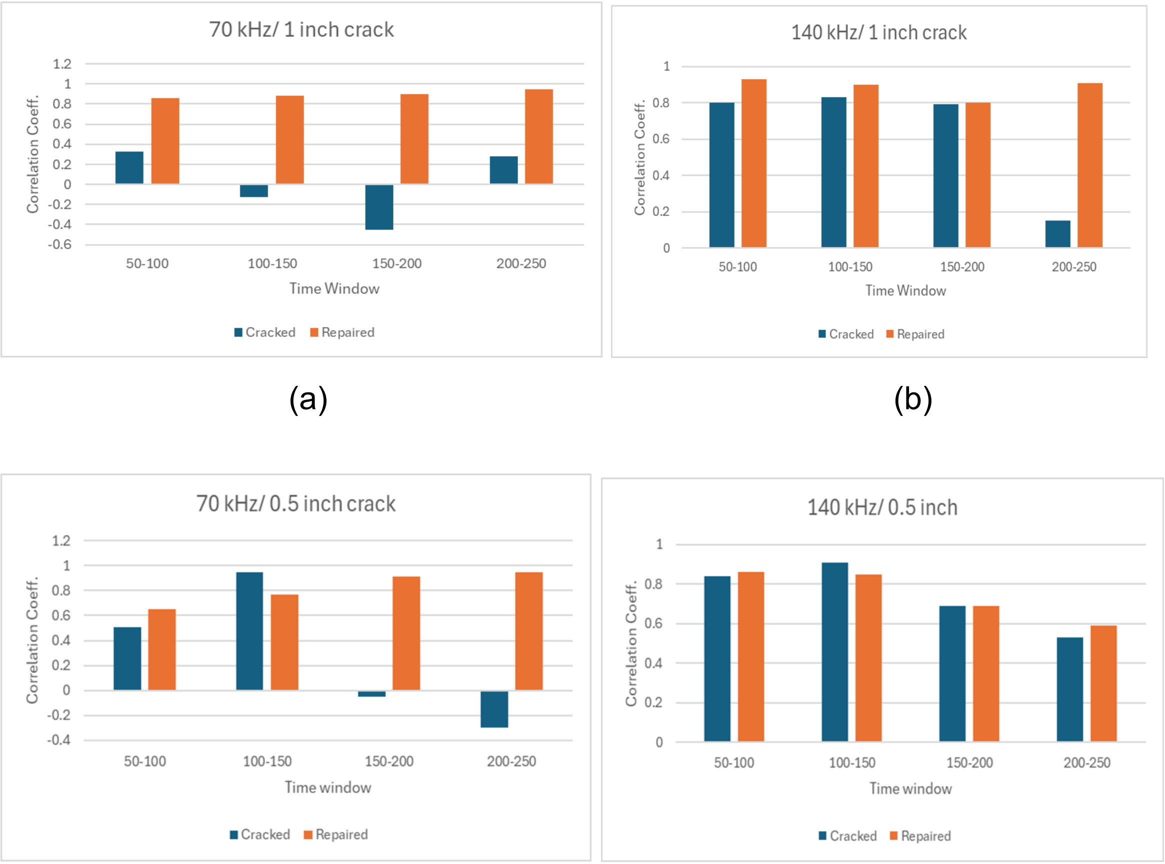

(a) (b)

(c) (d)

Figure 41. Correlation coefficients before and after crack repair for (a, b) a 1 in. crack and (c, d) a 0.5 in. crack using different frequencies.

Figure 41 highlights the correlation coefficient in the cracked and repair state for 1" and 0.5" deep cracks. It is observed that as the crack size becomes smaller, the relative change in correlation coefficient across the 140 kHz signal is not significant. In comparison, the 70 kHz signal showed relatively high correlation coefficients after repair in most time windows. It can be argued that for the current specimen, 70 kHz signal capture wave-crack interaction in the cracked and repaired state is better than the 140 kHz signal.

Progressive monitoring of crack repair

In this section, progressive change in the signal transmission is observed for a specimen with a 1.5" deep crack. Once the crack is filled with the solution, hourly measurements of the first 9 hours and the 36th hour were taken in the process. Figure 42 shows the procedure for crack repair. As described earlier, additional efforts were made to achieve complete crack filling. This was done by drilling a hole up to the bottom of the crack, followed by pushing the repair solution using a syringe.

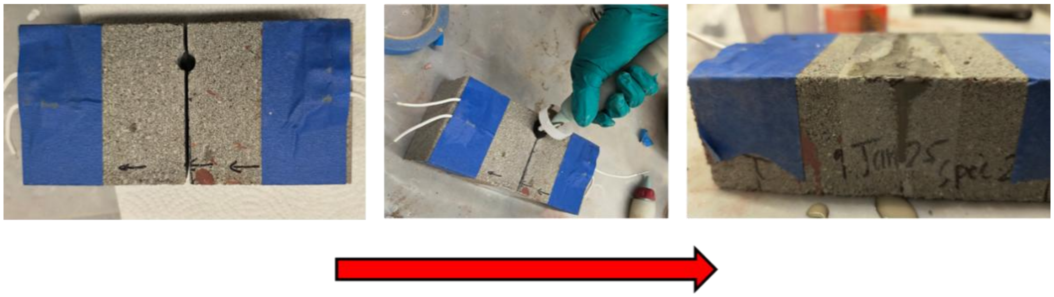

Figure 42. Crack repair process

Figure 43 shows the gradual change in the recovery in dB loss of the cracked specimen after its repair. The gradual improvement in the amplitude relative to the pristine state is evident across all the time windows. The only exception was the 200-250 μs window, which has a higher dB ratio. It can be associated with the new modes that were created due to evolving stiffness at the crack boundaries. A similar observation is observed for the 140 kHz signal as well (Figure 44), where all the time windows showed amplitude recovery in the signal transmission. Overall, in the context of amplitude comparisons, it is reasonable to state that a 36-hour time window is sufficient to regain the desired level of crack repair, as the amplitude recovery is evident across different time windows for both the inspection signals.

Figure 43. Gradual change in the amplitude recovery of the signal transmission across different time windows using a 70 kHz signal.

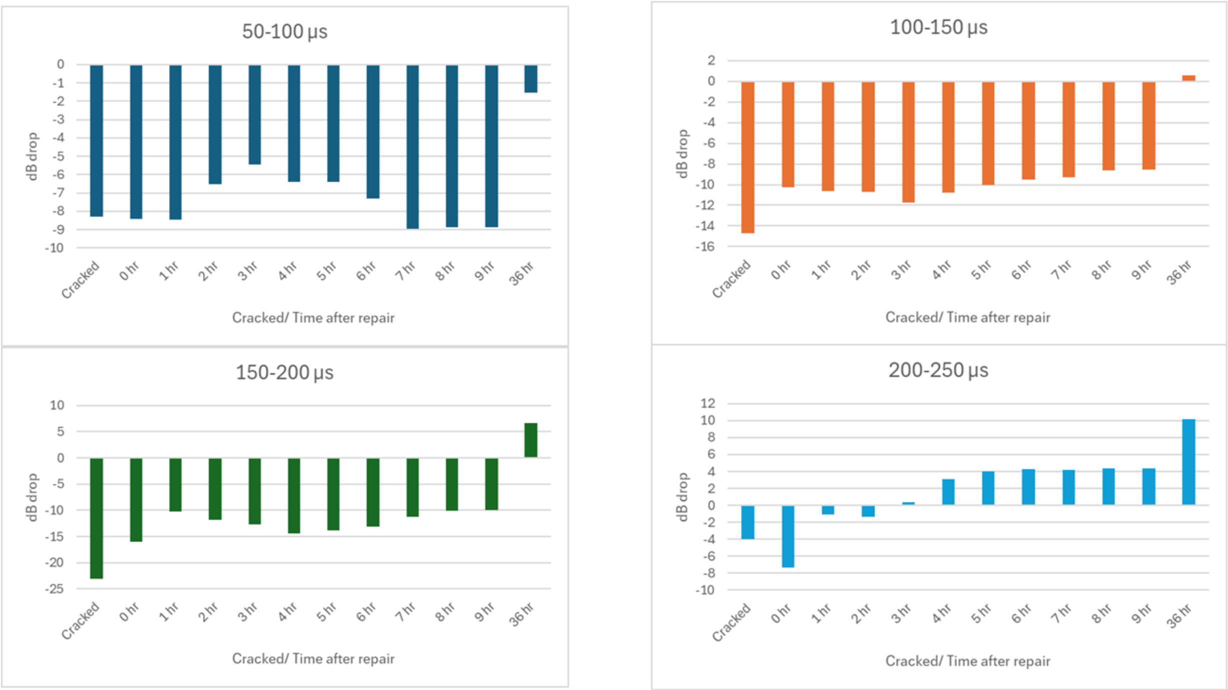

Figure 44. Gradual change in the amplitude recovery of the signal transmission across different time windows using a 140 kHz signal.

In the context of correlation coefficients, surprisingly, a relatively weak trend is observed across both the frequencies and in most time windows. For instance, in Figure 45, which represents the 70 kHz results, except for the 50-100 μs and 100-150 μs windows, other windows remained relatively inconclusive of any sign of repair. Either there is a negligible relative change, or a negative correlation is observed. This observation is even more inconclusive for the 140 kHz signal (Figure 46), as no logical trend was observed. Overall, based on the previous results and the progressive repair results, amplitude-based analysis remained consistent with the anticipated findings, i.e., signal strength recovery in different time windows hints towards the crack repair.

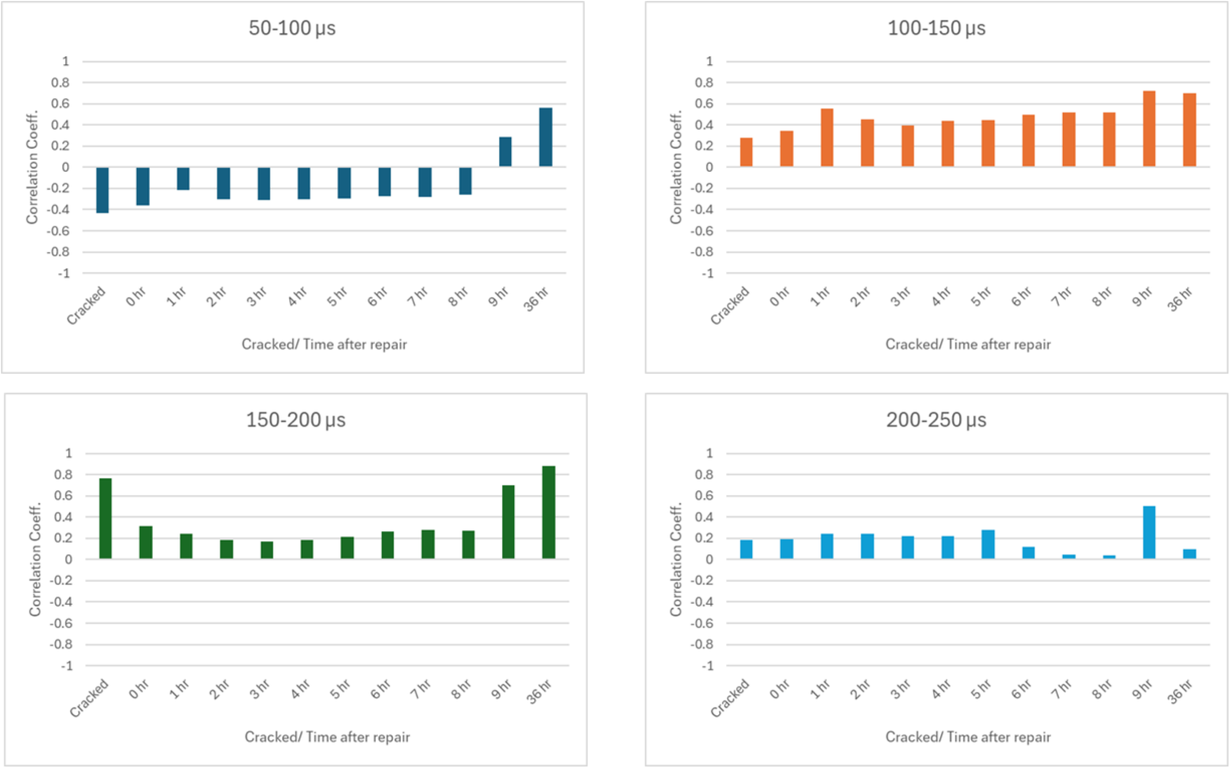

Figure 45. Trend of correlation coefficient change across different time windows for the 70 kHz signal.

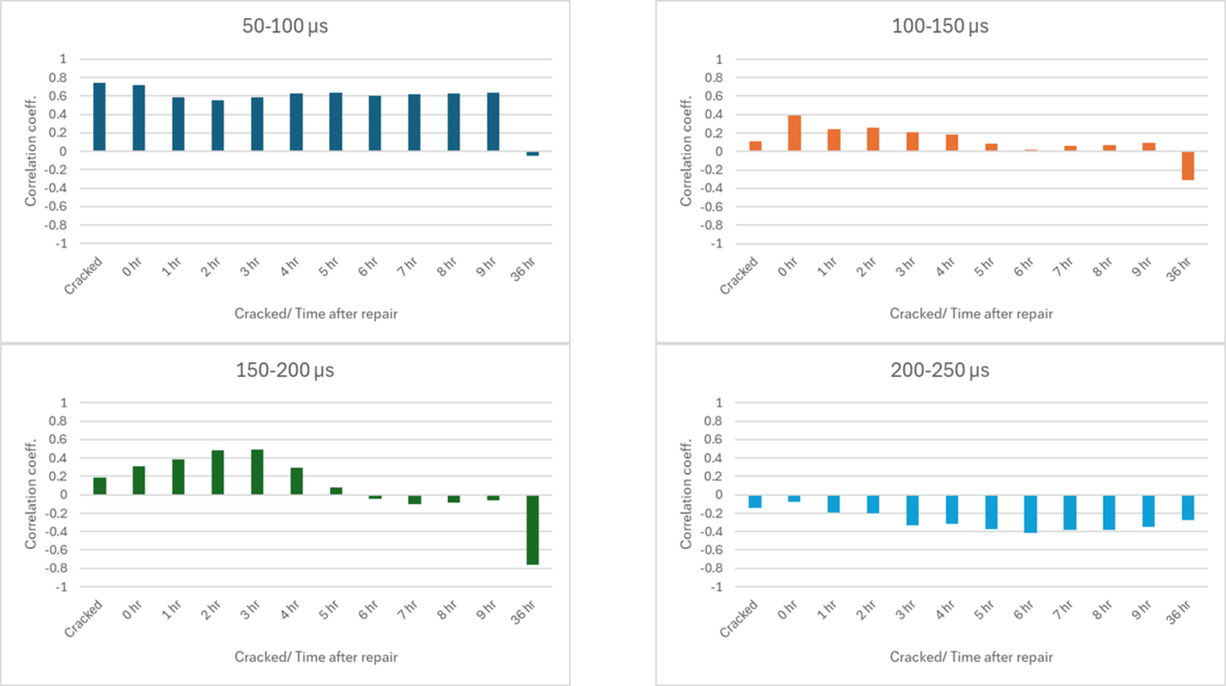

Figure 46. Trend of correlation coefficient change across different time windows for the 140 kHz signal.

Partially repaired crack

In this section, the crack was intentionally partially repaired by pouring the repair material from the top without the use of a syringe (Figure 47). This allowed only partial filling of the crack as the repair material did not penetrate the crack depth sufficiently.

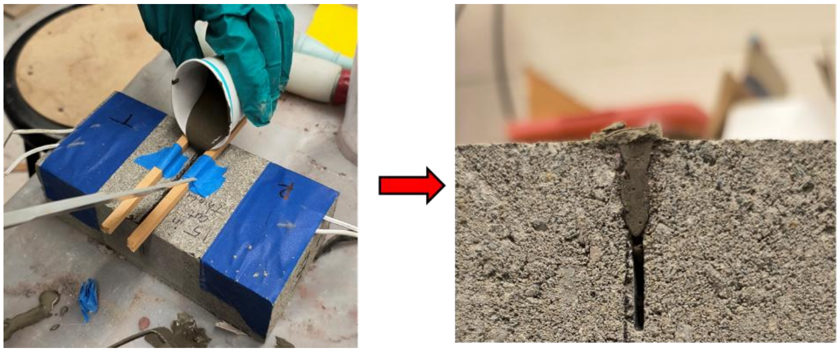

Figure 47. Partial crack filling procedure

Figure 48 shows the effect of partial crack repair on both frequencies. The partial amplitude recovery for the 70 kHz signal is evident across most time windows, whereas for 140 kHz, the amplitude recovery was relatively unchanged, hinting at no effective change in the signal recovery.

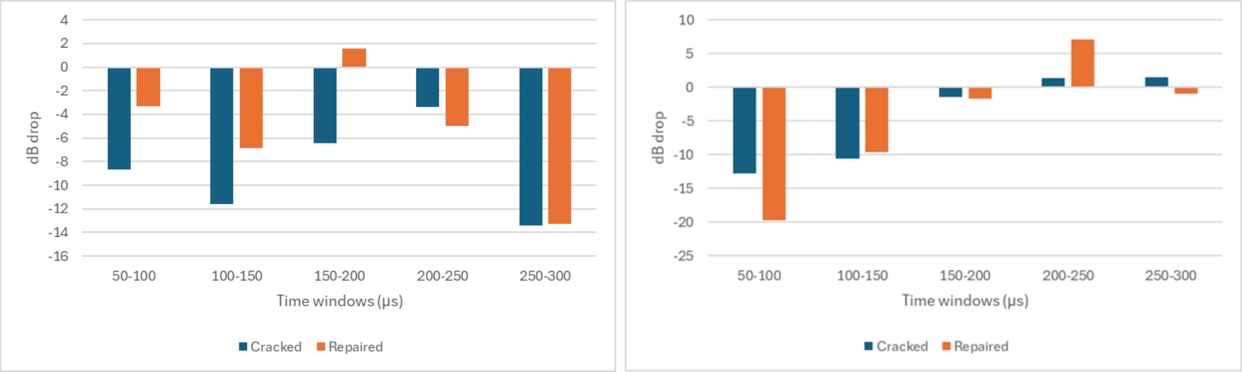

(a) (b)

Figure 48. Signal strength recovery for a partially filled crack obtained using (a) 70 kHz and (b) 140 kHz signals.

The analysis presented in this study fundamentally relied on comparing the signal from damaged or repaired states against a corresponding pristine baseline. However, as illustrated in Figure 49, the shape of the pristine signal exhibited considerable variation across different specimens. This variability poses a significant challenge to the transferability of the results, particularly in practical field scenarios where establishing a reliable pristine baseline may not be feasible. The inconsistency in baseline signals can be an effect of transducer coupling to the surface or variability in the quality control of the specimen. This issue not only limits comparative assessments but also highlights the difficulty in achieving standardized evaluations in real-world structures.

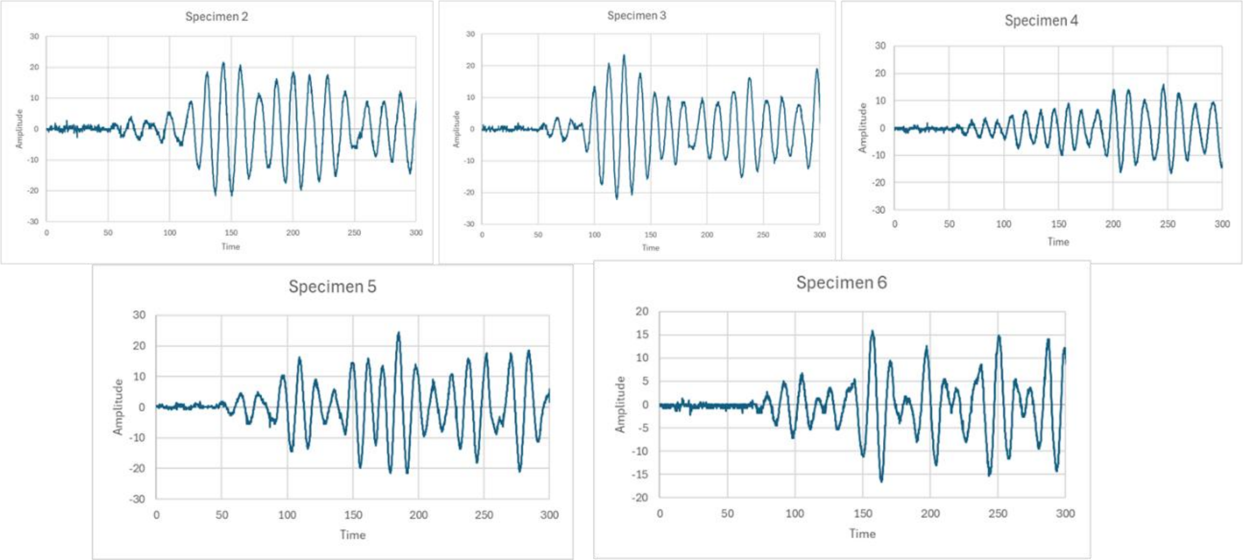

Figure 49. Variability of the pristine signal shape for a 70 kHz signal across different specimens.

Therefore, there is a pressing need to develop novel methodologies capable of establishing a universal or adaptive baseline that can represent the pristine condition across a broader range of specimens or structural regions. Such an approach would significantly enhance the robustness and applicability of baseline-dependent diagnostic techniques in field environments.

Field Testing of Concrete Slabs

Concrete slab

A concrete specimen measuring 24" × 24" × 8" was prepared using pre-mix concrete, with #4 rebars embedded at a cover depth of 2.5" in both longitudinal and transverse directions, forming a grid pattern (Figure 50). The dimensions of the specimen were selected to accommodate multiple cracks of varying depths and orientations simultaneously. To fabricate controlled cracks, a 7/32" thick plywood sheet was cut into a staircase-like profile, creating stepped regions with depths of 0.5", 1", 1.5", and 2". These plywood inserts were placed into the freshly poured concrete and removed approximately one hour after pouring, just before the concrete reached full hardening. This method ensured clean and well-defined artificial cracks. Two orientations of cracks were introduced: one set aligned perpendicular (90°) and another inclined at 30° to the top surface, to study the effect of crack angle on wave propagation. Each artificial crack was designed to be 6" long, providing enough separation to minimize interference from adjacent cracks and allowing multiple measurement points along the same crack. In addition to these, a 2.5" deep crack was introduced to intersect the rebar, simulating a typical failure scenario where cracks initiate at the rebar and propagate to the surface. A pristine (uncracked) region was also preserved intentionally within the specimen to serve as a reference for wave propagation in undamaged concrete. The inclusion of this region enables a direct comparison of transmission characteristics between cracked and uncracked zones.

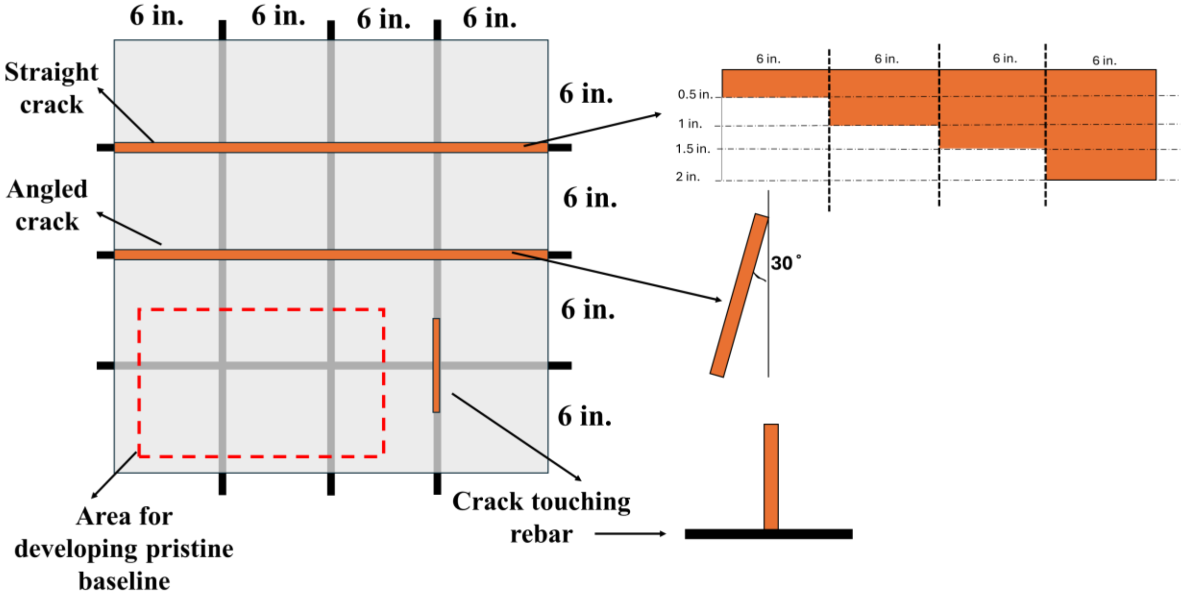

(a)

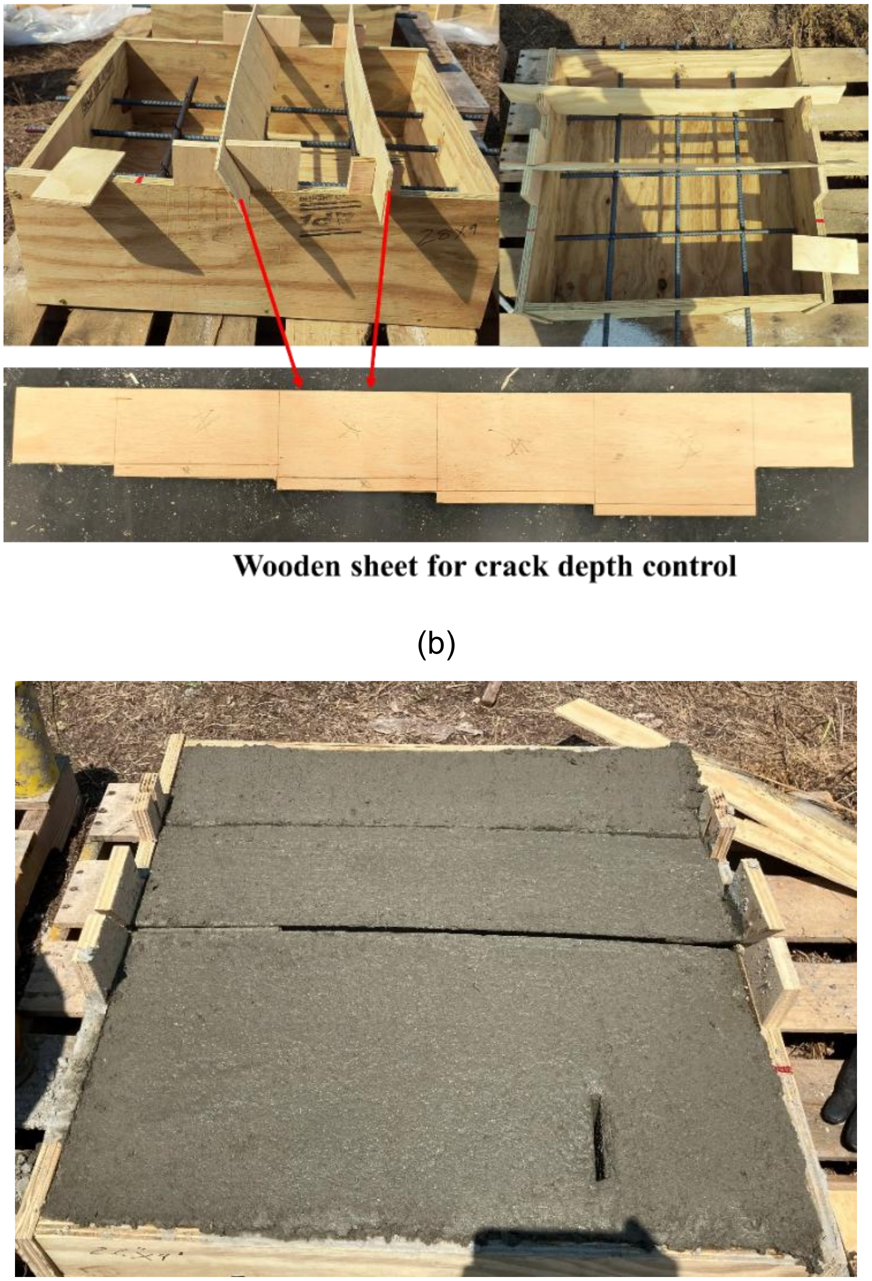

(b)

(c)

Figure 50. (a) Schematic for the concrete specimen, (b) wooden mold for pouring the concrete, and (c) final form of the concrete slab.

In summary, the specimen was designed to comprehensively investigate ultrasonic wave propagation across straight and inclined cracks of varying depths, as well as through pristine concrete. The setup enables evaluation of multiple crack conditions within a single specimen, offering both experimental efficiency and valuable comparative insights.

Concrete beams

To simulate realistic tensile crack formation in reinforced concrete, beam specimens measuring 20 in. in length, 6" width, and 6" depth were prepared. Cracks were introduced using a three-point bending test, which induces flexural tensile stresses at the bottom surface of the beam, leading to controlled crack initiation and propagation (Figure 51). To regulate the maximum depth of crack propagation, steel rebars were embedded at three different depths of 1.5", 2", and 2.5" from the top surface of the beam. During testing, the applied load gradually increased until a surface-visible crack formed and extended vertically. The test was terminated immediately upon visual confirmation that the crack had reached the depth of the embedded rebar. This ensured that crack growth remained limited to the intended depth, preventing overextension and enabling consistent replication across specimens.

Through this method, thin, realistic tensile cracks with their width ranging from 0.5 mm to 0.1 mm were successfully generated and closely resemble those observed during early stages of structural deterioration in the field. The variation in rebar depth served as a control mechanism, allowing the formation of cracks of different depths. Overall, the combination of the three-point bending configuration and depth-specific rebar placement provided a reliable approach for generating structurally relevant cracks. The resulting specimens are suitable for evaluating the performance of non-destructive testing techniques in detecting and characterizing fine subsurface cracks.

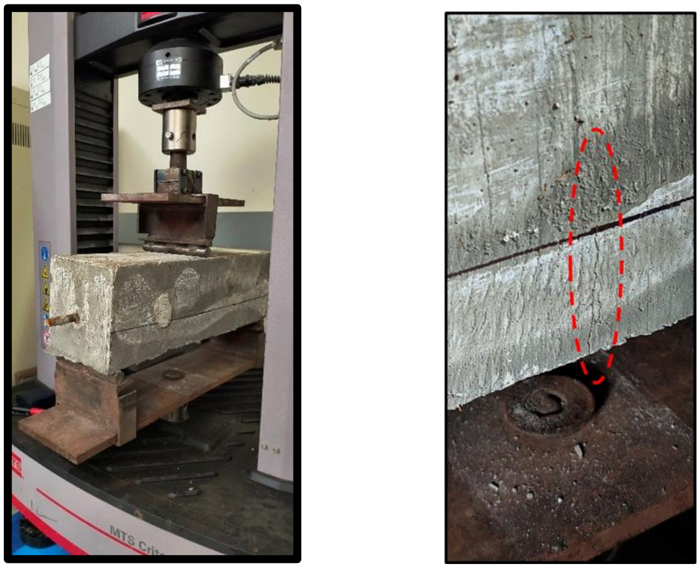

(a) (b)

Figure 51. (a) Three-point bending test setup, and (b) generated crack reaching up to a minimum depth of the rebar

Field Ultrasonic Testing Results

Ultrasonic tests were conducted on the concrete slab and concrete beam after 28 days of curing in outdoor conditions. Dry point contact transducers are used for this task because of the need to conduct ultrasonic measurements at different positions. The advantage of these transducers over piezoceramic patches is their point-based contact, allowing them to work around uneven surfaces. Additionally, these do not require any couplant for signal transmission, making them suitable for field tests. Based on the insights gained from piezoceramic patch-based investigation on concrete bricks, 50 kHz shear transducers were selected (Model: S1802 by ACS Instruments, Germany). The ultrasonic measurements were conducted in a pitch-catch configuration with a separation of 2", 4", 6", and 8" with the aim of observing trends between surface wave arrival time and transmitted energy with the propagation distance. The comparison of such observations made over the pristine region of the specimen and the cracked region will facilitate the estimation of crack depths and the quality of their recovery after repair.

Figure 52a shows the schematic of the transducer configuration for ultrasonic testing across the cracked region of the concrete slab. The transmitter and receiver were separated at different distances on either side of the crack. Furthermore, the length of the crack (6") supported the repeated measurements across two different rows along the length of the crack. Similarly, Figure 52b shows the marked regions for ultrasonic testing on the cracked concrete beam. For the pristine section of the slab, three identical yet independent rows across different locations of the pristine region were used to record signal transmission. Figure 52c shows the UT on a concrete beam and the concrete slab.

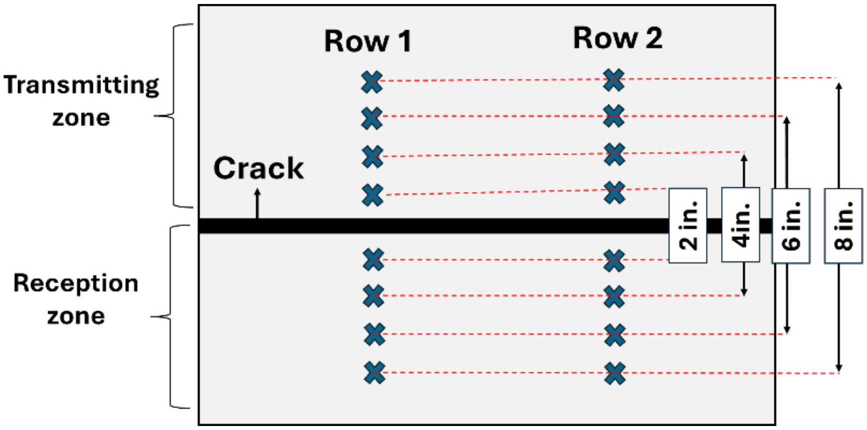

(a)

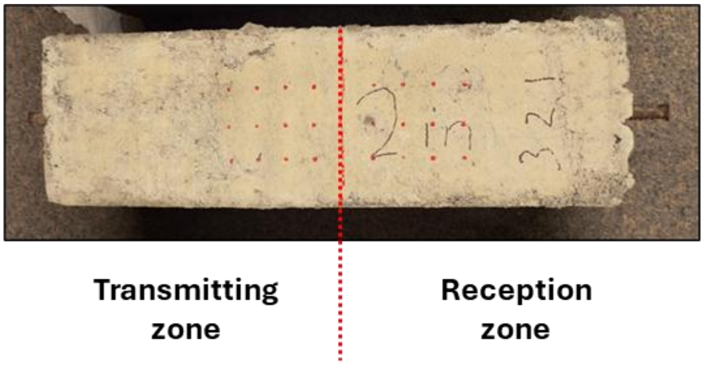

(b)

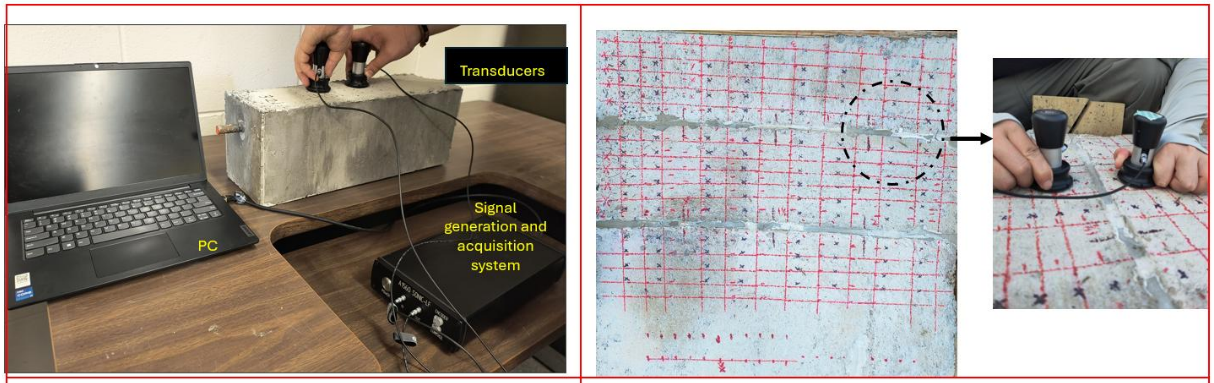

Ultrasonic testing on a concrete beam

Ultrasonic testing on the concrete slab

(c)

Figure 52. Schematic of ultrasonic testing configuration for (a) concrete slab, (b) concrete beam, and (c) ultrasonic testing setup

Investigating pristine/uncracked regions

Conventionally, UT relies on comparative analysis of test structures in their pristine and damaged/ repaired conditions. Obtaining pristine conditions in field conditions is nearly impossible, as most structures do not have any record of their pristine baseline reference for different types of tests. Inspections based on UT are sensitive to surface conditions, the complexity of structural components, and defect geometry. It remains highly challenging to isolate contributions of such factors; therefore, it is desired to identify UT parameters that remain consistent with different specimens irrespective of their design. With this objective, signal transmission is studied across different specimens (3 beams and the pristine section of the concrete).

Signal transmission of surface waves was studied across three independent rows on each of the specimens. The signal characteristics were recorded and analyzed for different propagation distances by varying the separation between the transmitting and receiving transducers by 2", 4", 6", and 8".

Time of flight: Figure 53 illustrates the general trend of signal transmission in relation to the arrival time of the first peak of the surface wave. For the 2" distance, the signal exhibited reasonable consistency in arrival time, ranging between 30-40 μs across all rows and specimens. The peak considered in this observation is clearly above the noise level, without any post-processing. It should be noted that the signals used for time-of-arrival comparisons may have been recorded with different gain factors during acquisition. These gain values were selected based on experimental requirements to achieve a sufficient signal-to-noise (SNR) ratio. For the time-of-arrival discussion, no gain conversion was applied. One notable observation was that for Beam 1 and Beam 2, the signals were sufficiently similar across different rows, in contrast to those for Beam 3 and the slab. This difference could potentially be attributed to the shallower rebar depths of 1.5" and 2" in Beam 1 and Beam 2, compared with the deeper rebar depth of 2.5" in Beam 3 and the slab. The beams with lower rebar depth may have received some assistance in the signal transmission from the rebar, providing consistent transfer of the signal strength. However, this study does not aim to investigate such effects in detail from a field inspection perspective, where the knowledge of the rebars is not readily available.

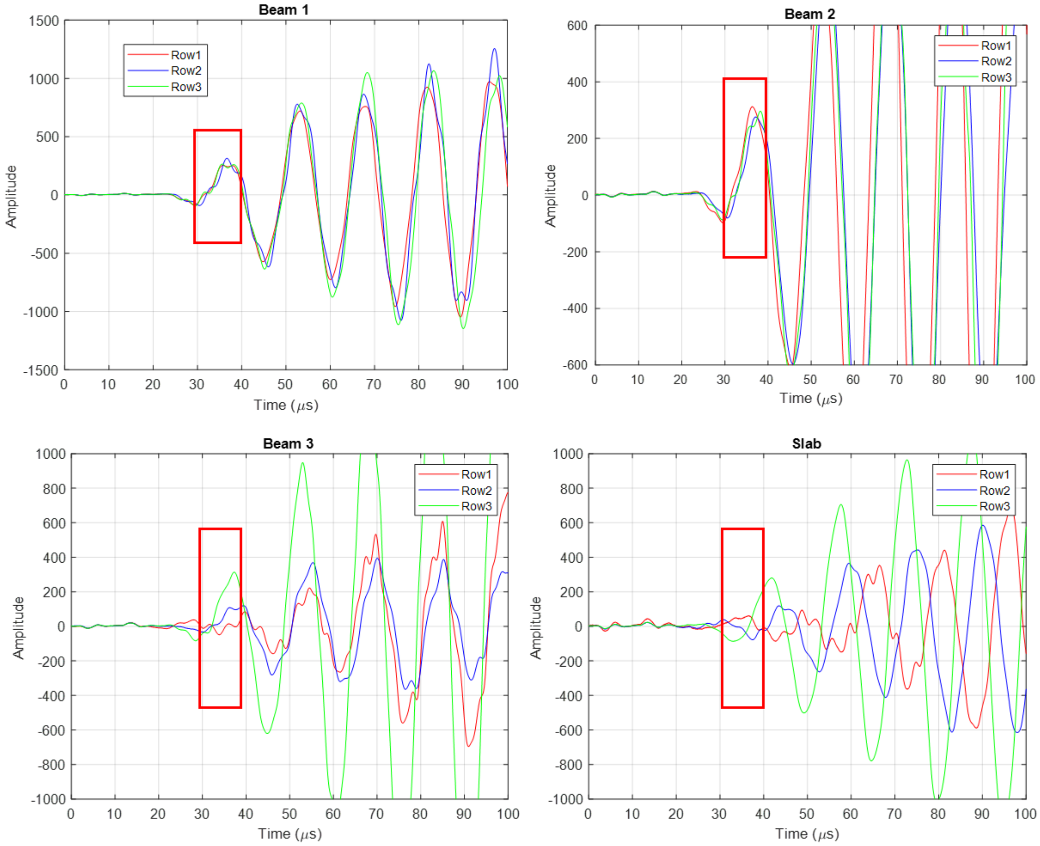

Figure 53. Signal transmission trend for 2" transmission distance

Unlike the narrow 30 to 40 μs window observed for signal arrival at a 2" transmission distance, the trend becomes inconsistent with increasing propagation distances of 4", 6", and 8". For the 4" separation (Figure 54), Beam 1 and Beam 2 exhibited consistent signal arrivals between 50 and 60 μs, whereas Beam 3 and the slab showed arrivals over a broader range of 40 to 60 μs. This inconsistency became more pronounced at larger propagation distances of 6" (Figure 55) and 8" (Figure 56), making it challenging to identify a common arrival time trend among different specimens. A likely reason for this observation is that the contribution of the pure surface wave diminishes at longer propagation distances, allowing other modes such as converted modes and those traveling through the rebar to dominate the signal shape. Based on these observations, only the 2" results will be considered for the remainder of this report.

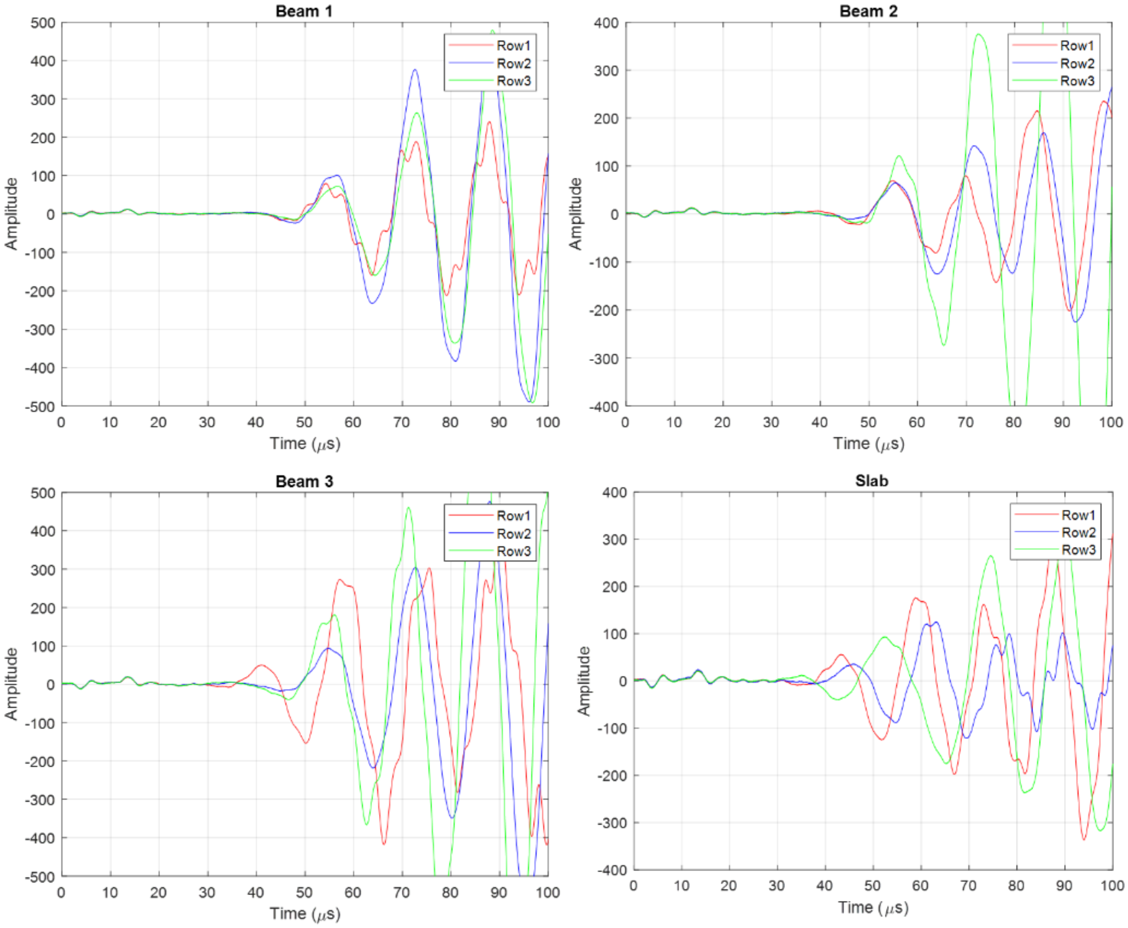

Figure 54. Signal transmission trend for different specimens at 4" transducer separation

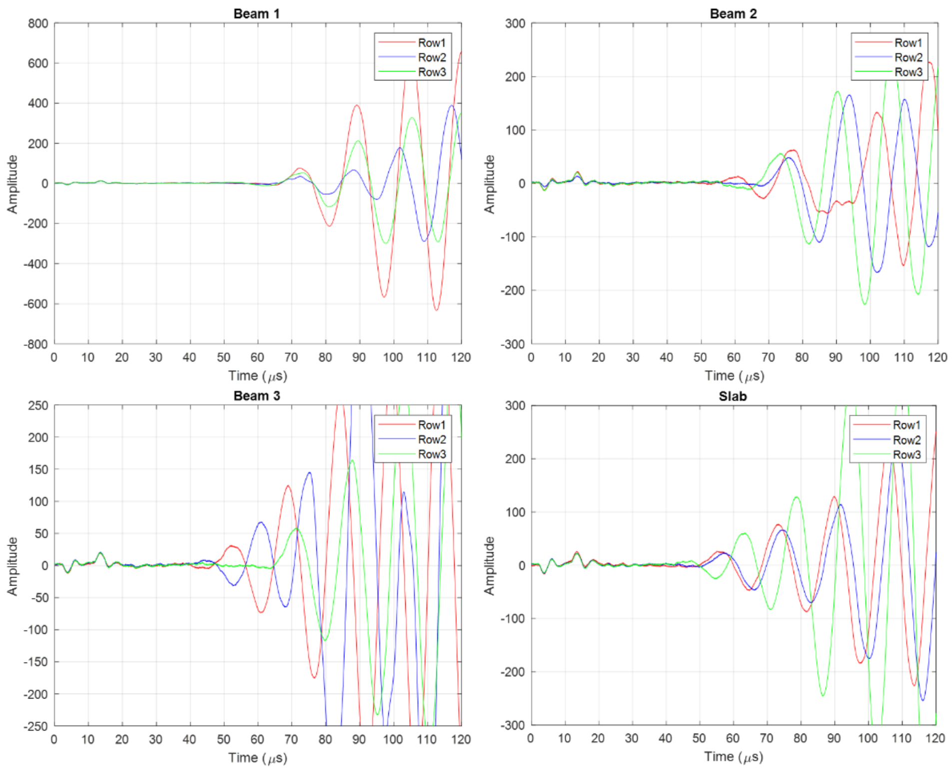

Figure 55. Signal transmission trend for different specimens at 6" transducer separation

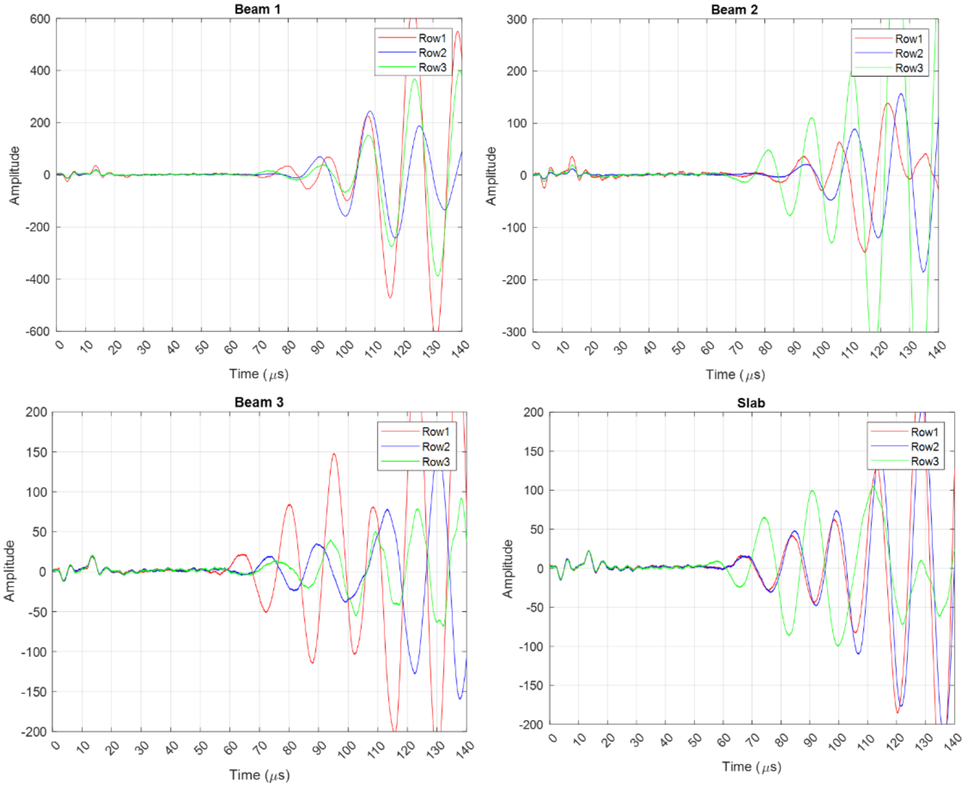

Figure 56. Signal transmission trend for different specimens at 6" transducer separation

Signal Shape and amplitude: In contrast to the time of arrival characteristics, an evident variation in the overall shape and amplitude of the transmitted signals was observed for the same transducer separation in all the specimens. For this discussion, the results of the concrete slab are presented in Figure 57. The potential cause for varying signal characteristics is the inherently different contact conditions at the test points. Furthermore, the test points are in different vicinities to rebars, which may affect the strength of the signal transmission. In field tests, it is impractical to even attempt to isolate the effect of such factors, given the structural complexity and the time efficiency required in field tests. Hence, it is not recommended to use an amplitude or signal shape baseline for the pristine condition of the specimens. It is more appropriate to make point-based comparisons when analyzing the effects of crack repair.

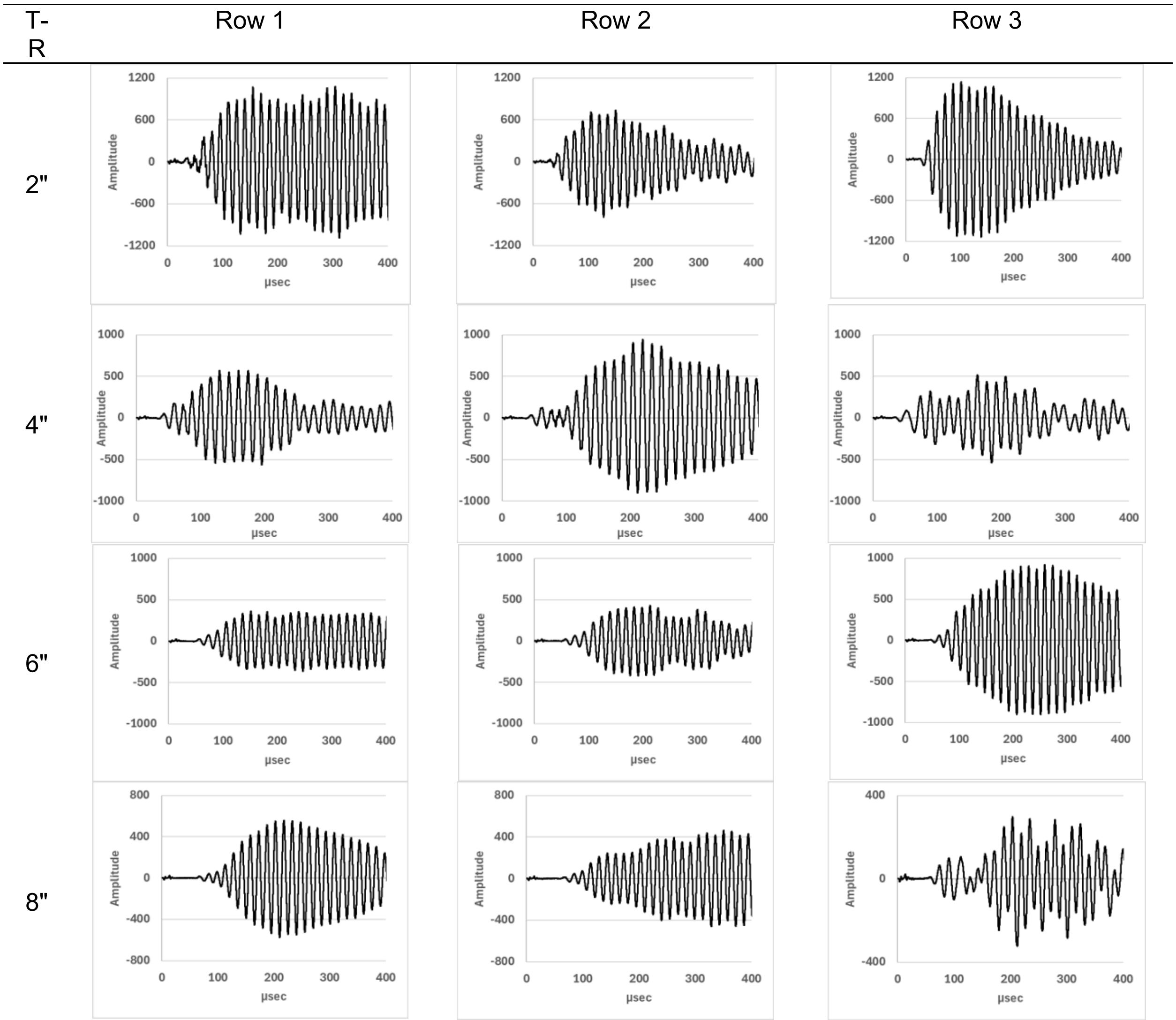

Figure 57. Trends of amplitudes across three different rows in pristine conditions for different transmitter-receiver separations

In conclusion, it is established that irrespective of the test locations, the time of flight of the surface wave remains relatively comparable in pristine conditions. Therefore, the time of arrival is selected as a conclusive baseline parameter for the pristine conditions.

It is desirable to compare the time of arrival in the cracked scenario to evaluate the effect of crack depth on the transmitted signal.

Effect of cracks on time of arrival of surface wave

Concrete Beams: Figure 58 shows the variation in the size of the tensile cracks developed in the concrete beams and the corresponding signal transmission between transducers separated by 2". For beam 1 with 1.5" rebar depth, and beam 2 with 2" rebar depth, the crack on the top and the side of the cylinder reached up to a measurable crack with of 0.10 mm. Both the cracks reached a minimum depth of up to the rebar position and expanded slightly beyond it, but significantly narrower in width (below 0.1 mm). For such small-width cracks, it can be anticipated that the crack faces were still in contact at multiple locations once the tensile load was removed. On the contrary, the crack width on the top surface reached up to 0.5 mm for beam 3, which has a rebar depth of 2.5", and the crack on the side surface reached up to 0.2 mm.

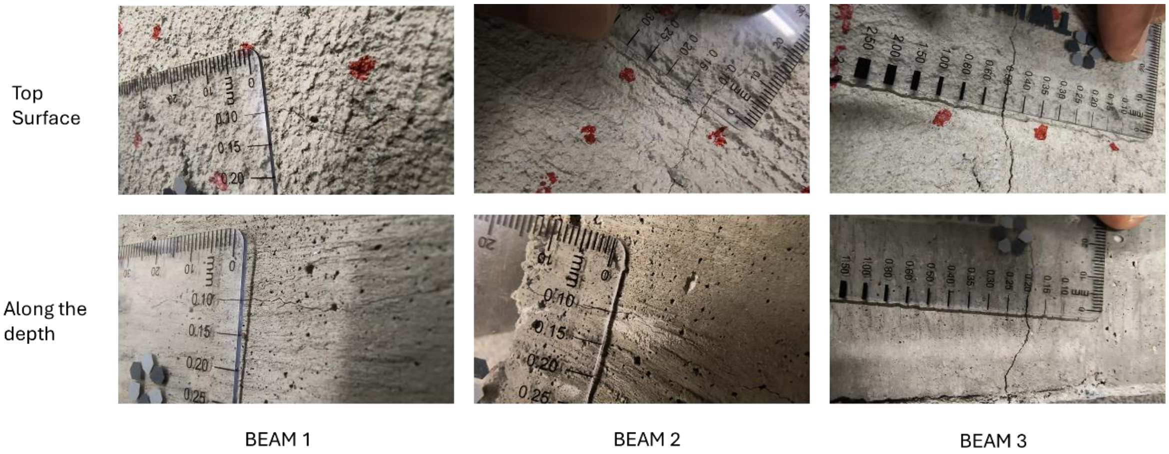

Figure 58. Crack size measurements on the top and the side surface of concrete beams

The signal transmission for 2" transducer separation (one transducer on either side of the crack) for beam 1 and beam 2 shows a noticeable shift in the arrival time of the surface wave (Figure 59). Compared to the pristine condition, where the time of arrival of the surface wave was between 30–40 µs, the new arrival of 40–50 µs was observed and is more prominent in beam 2, as the cracks are relatively deeper. Furthermore, the wave delay pattern remained unchanged between beam 2 and beam 3, potentially marking the limitation of the 50 kHz surface waves. At 50 kHz, the penetration depth of the surface wave in concrete is approximately 1.75", assuming a typical surface wave velocity of about 2000 m/s.

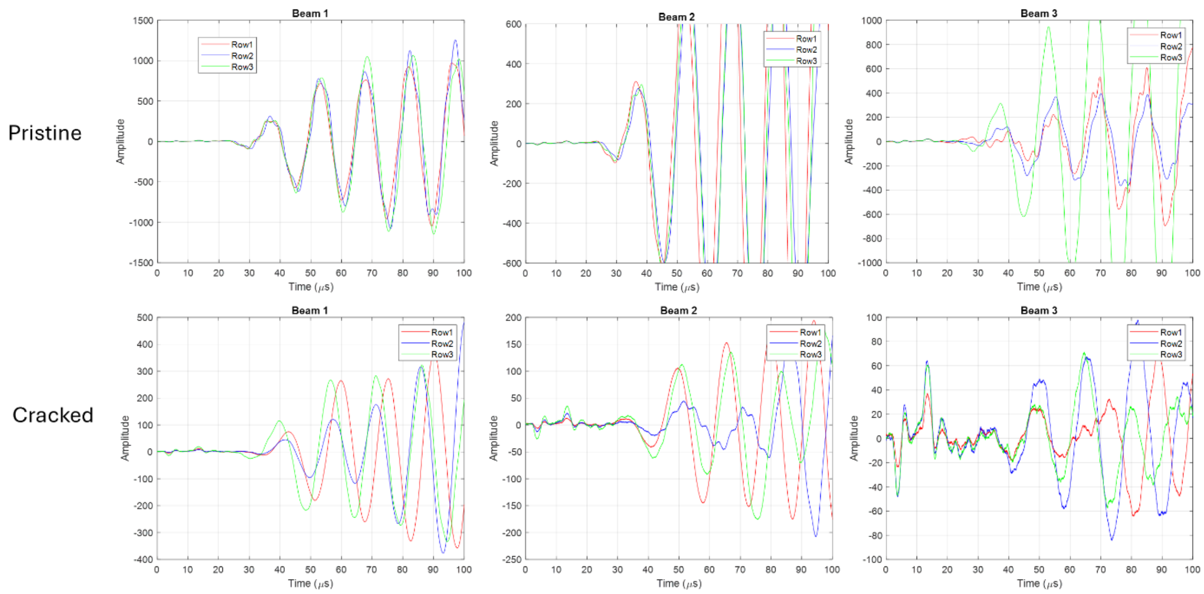

(a) (b) (c)

Figure 59. Signal transmission across (a) Beam 1, (b) Beam 2, and (c) Beam 3 in their pristine and cracked state

Concrete slab: The cracks in the concrete slab offer a more controlled view of the effects of the crack depth on the signal transmission. Figure 60 shows the signal transmission results of the straight crack across two different rows of the same crack length. It can be observed that the time of arrival of the surface wave for 0.5" crack depth remained relatively similar to the pristine conditions i.e. within 30-40 µs. The potential reason for the 0.5" crack depth not affecting the signal transmission is its limited interaction with the surface wave, as it is significantly less than the wavelength of 50 kHz surface wave (approximately 1.75"). However, there is an evident delay in the arrival time of the surface with increasing crack depth. For 1" crack depth, the surface arrival time is between 40-50 µs, whereas for 1.5" crack depth, the arrival time is between 50-60 µs. At 2" crack depth, the signal didn’t show significant change in the arrival time, as sufficient contribution from the first peak remained within the window of 50-60 µs highlighting the penetration limitation of the surface wave.

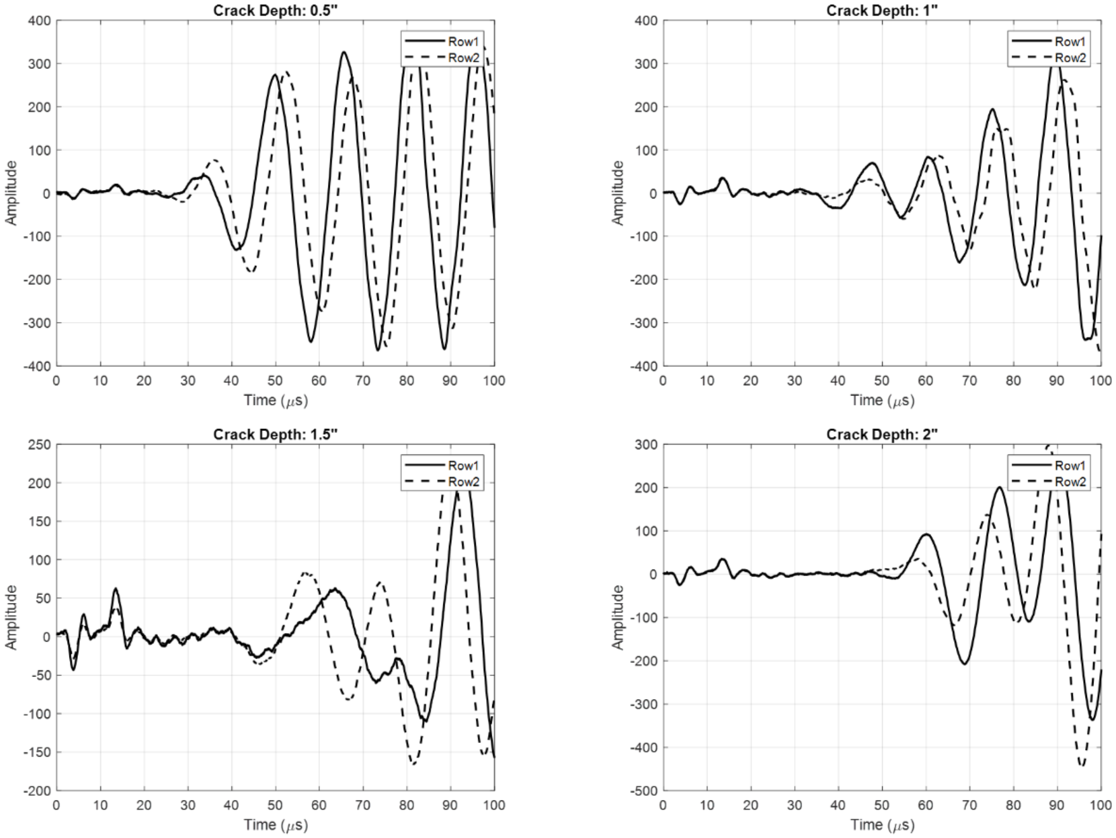

Figure 60. Time of arrival trend with different crack depths for a straight crack

Figure 61 shows the signal transmission for the inclined crack at different crack depths. Noticeably, the results are reasonably similar to the straight crack, where 0.5" crack depth did not affect the time of arrival significantly, whereas 1" and 1.5" crack depth showed measurable delays in the arrival time of the surface wave to 40-50 μs and 50-60 μs. Furthermore, the 2" crack did not show any change in the arrival time as it continued to stay within 50-60 μs window, marking the limitation of the penetration depth the surface wave.

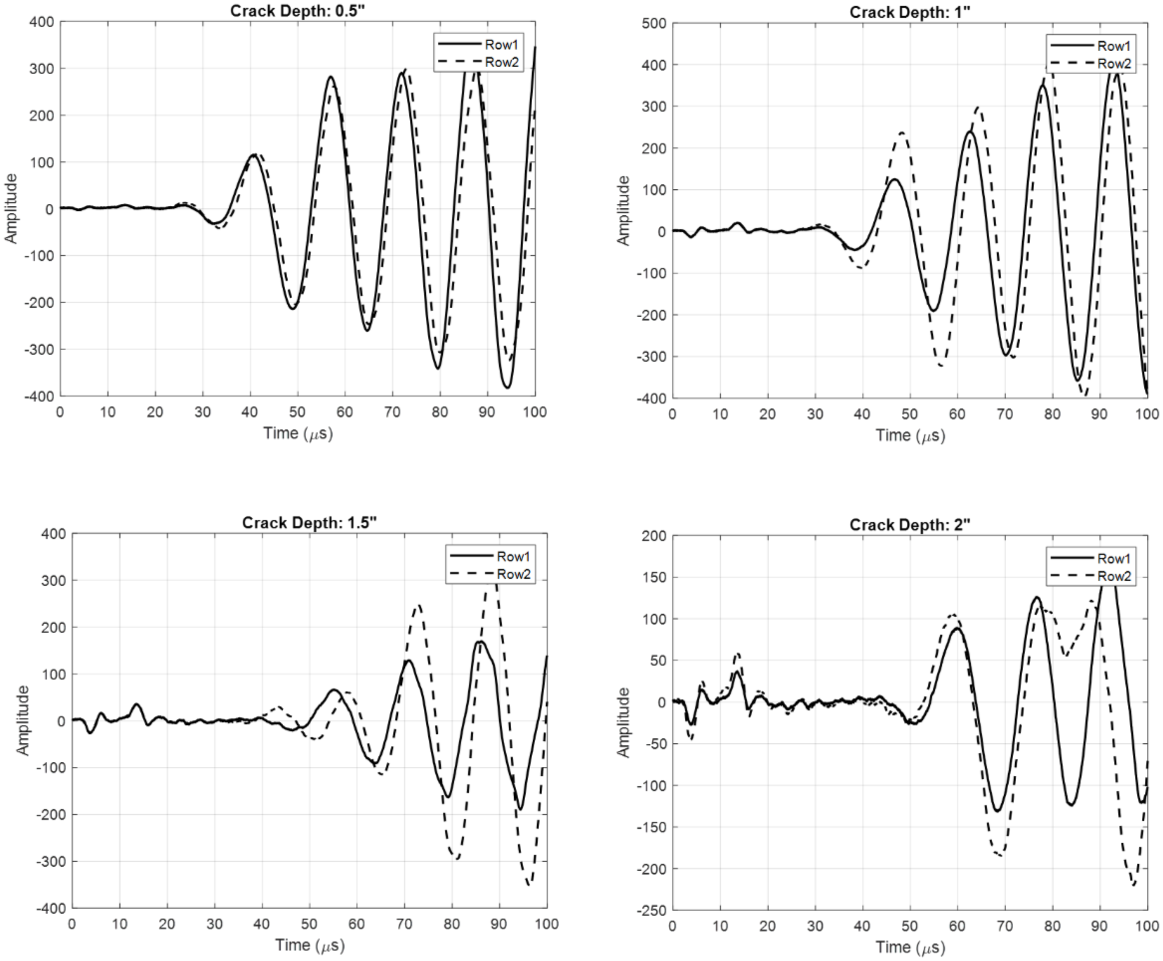

Figure 61. Time of arrival trend with different crack depths for a 30˚ inclined crack

Figure 62 shows the variation trend of the time of arrival window with increasing crack depth for both the straight and the inclined crack. Here, the y-axis is the average time of the upper and lower bounds of the considered time window, i.e., 30-40 μs for pristine and 0.5" crack depth, 40-50 μs for 1” crack depth, 50-60 μs for 1.5" and 2" crack depths. The figure highlights that the limited interaction of the 50 kHz surface wave occurs with crack depths beyond 1.5". In general, no substantial change in the arrival time signature of the surface wave was observed for the 30˚ inclined crack.

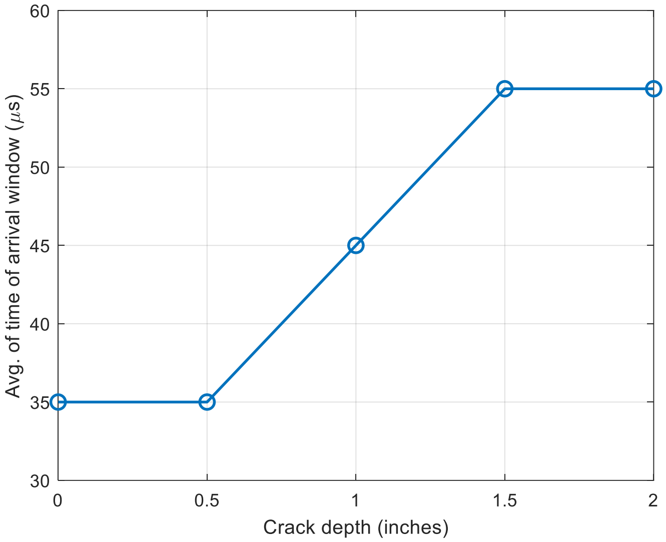

Figure 62. Variation in the average time of arrival with crack depth for both the straight and inclined cracks.

Effect of crack repair on time of arrival of surface wave

The crack width on the concrete beams was in the range of 0.5 mm to 0.1 mm and could not be repaired with the available repair setup in the laboratory. Therefore, beam results are not discussed in the context of crack repair.

Concrete slab: The cracks on the slab were filled with the repair mix, which comprises fast-setting concrete. The signal transmission was recorded at the exact same points as for the cracked specimens, and the new gains applied during the repaired state of the data acquisition were recorded and converted to make comparisons at the same scale. The data collection on the repaired state was performed 3 hours and 24 hours after the repair.

Figure 63 shows the change in the time of arrival for a straight crack when repaired. As anticipated from earlier discussions, the crack depth of 0.5" didn't affect the time of arrival substantially, as the time of arrival remained relatively unchanged between 30-40 μs. A slight shift to a relatively earlier window, i.e., 20-30 μs, was observed for the 3-hour repair in Row 1-2 results; however, the shift to 30-40 μs at the 24th hour makes the result a little inconclusive. This slight shift could be a result of either relatively closer inspection points due to manual adjustments or the improved strength of the crack material due to different material properties of the slab concrete mix and the repair mix. In contrast, the results of 1", 1.5", and 2" crack depths are more conclusive about the crack repair, as the time of arrival of the surface wave moved back to 30-40 μs or earlier after the repair. In most cases, the arrival time between 20-30 μs was observed for the 3-hour post-repair tests. The earlier arrival time observed at 3 hours post-repair is likely due to the freshly placed fast-setting concrete forming a continuous and relatively stiff path across the crack. In the early stage, the filler may have a higher apparent stiffness than the surrounding cracked zone, allowing the surface wave to traverse the repair zone more directly with less scattering and delay. By 24 hours, the repair material's properties and moisture distribution have stabilized, making its acoustic response more like the surrounding concrete and resulting in arrival times consistent with pristine regions. Overall, the improvement in the time of arrival of the surface wave was evident across different row inspections. This serves as the first measurable property in the ultrasonic inspection of the crack repair. To reiterate, it is to be noted that signals were not normalized on the same signal gain scale for the time of arrival comparisons.

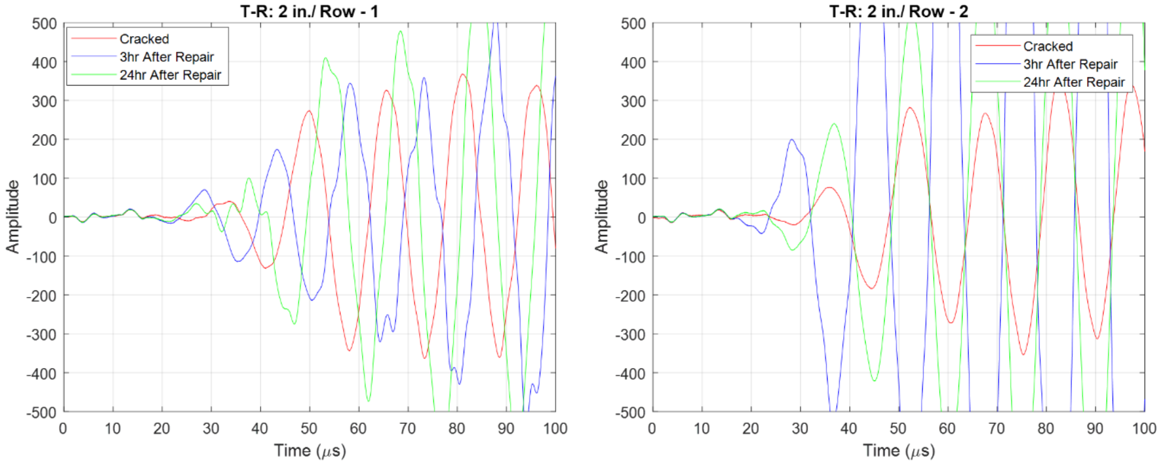

(a)

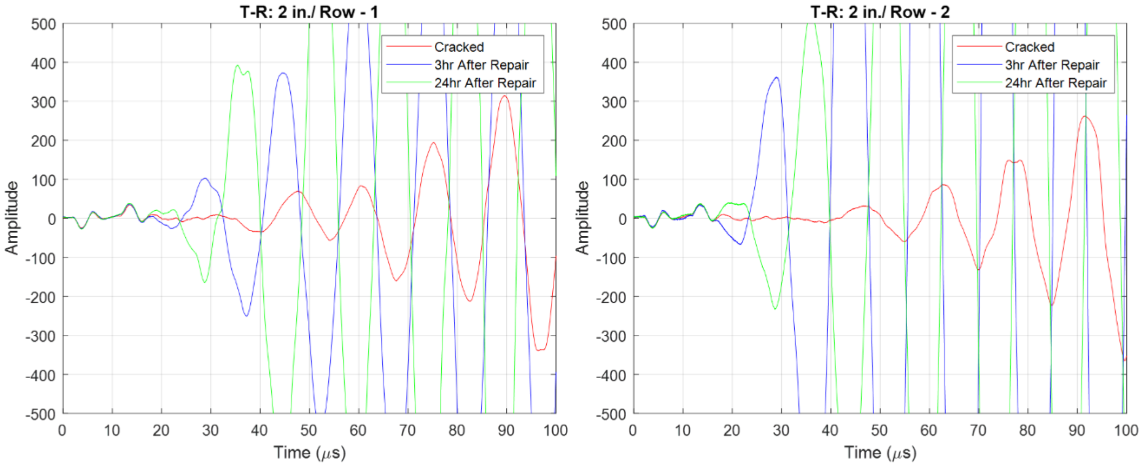

(b)

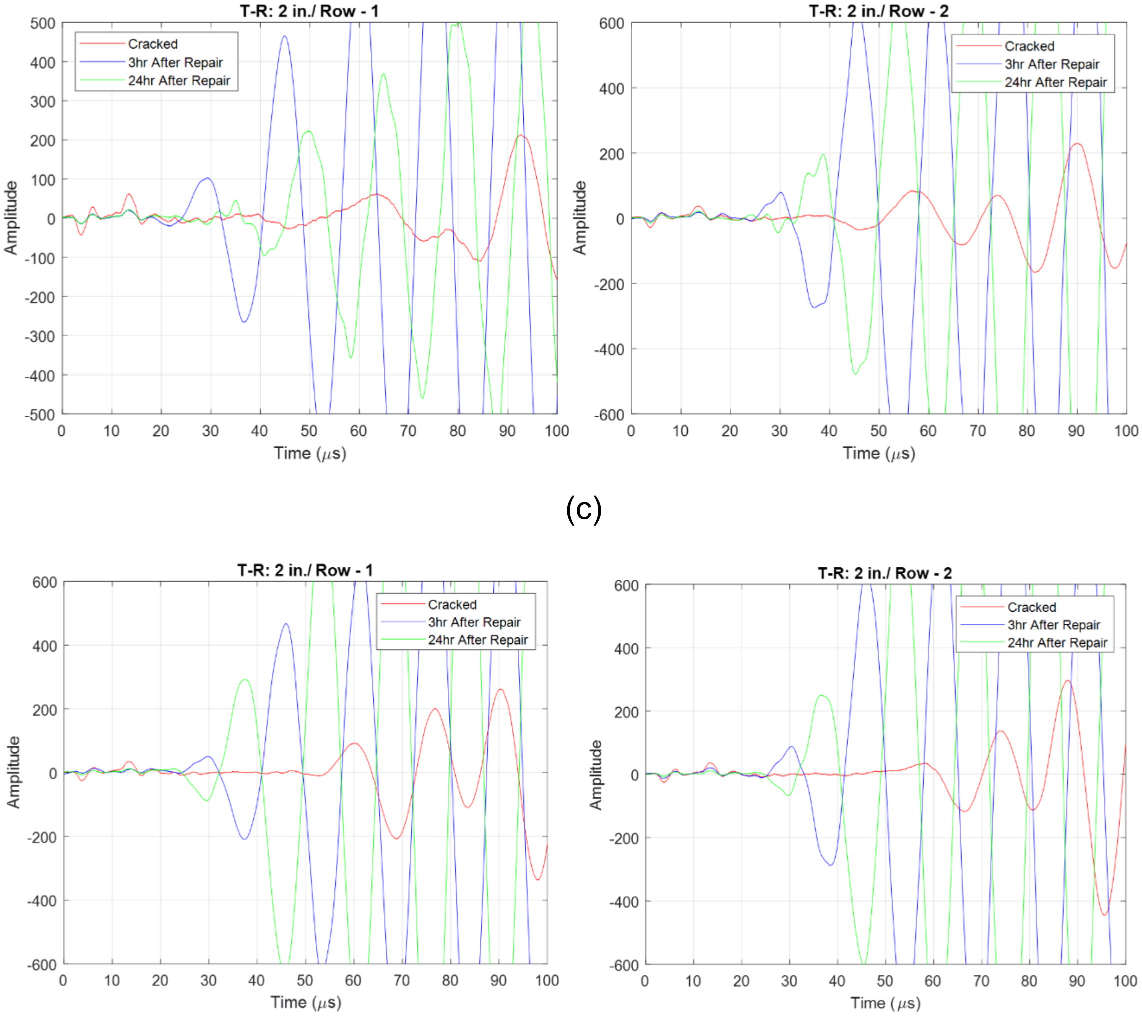

(c)

(d)

Figure 63. Time of arrival trend obtained at different time intervals post-repair of the straight crack regions with crack depth of (a) 0.5", (b) 1", (c) 1.5", and (d) 2"

Similar to the straight crack, the overall improvement in the time of arrival was observed across all the repaired sections of the inclined crack (Figure 64). As expected, the crack with 0.5" depth showed minimal changes in the signal arrival time, whereas the time shifts to a 30-40 μs window are evident across all the cracks from 1" depth and above. Moreover, early arrival in 20-30 μs for 3-hour post-repair results reestablishes the above discussion concept that in the early stage, the filler may have a higher apparent stiffness than the surrounding cracked zone, allowing fast transmission of the surface wave. However, 24 hours post-repair, the repair material’s properties and moisture distribution stabilized, which makes the time of arrival similar to the pristine state observations.

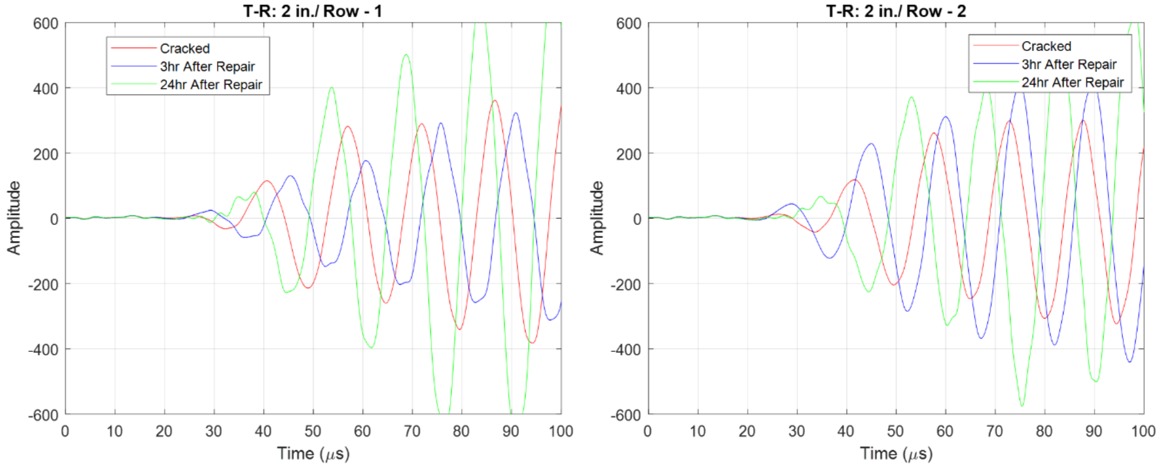
T-R: 2 in./ Row - 1
T-R: 2 in./ Row - 2
Cracked
3hr After Repair
24hr After Repair
Amplitude
Time (μs)
600
400
200
0
-200
-400
-600
0
10
20
30
40
50
60
70
80
90
100

(a)

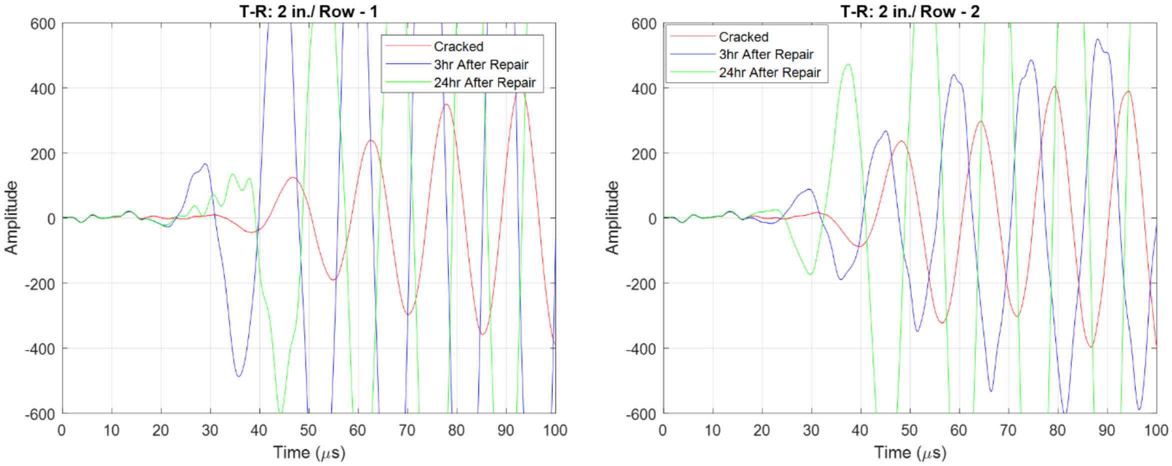
T-R: 2 in./ Row - 1
T-R: 2 in./ Row - 2
Cracked
3hr After Repair
24hr After Repair
Amplitude
Time (μs)
600
400
200
0
-200
-400
-600
0
10
20
30
40
50
60
70
80
90
100

(b)

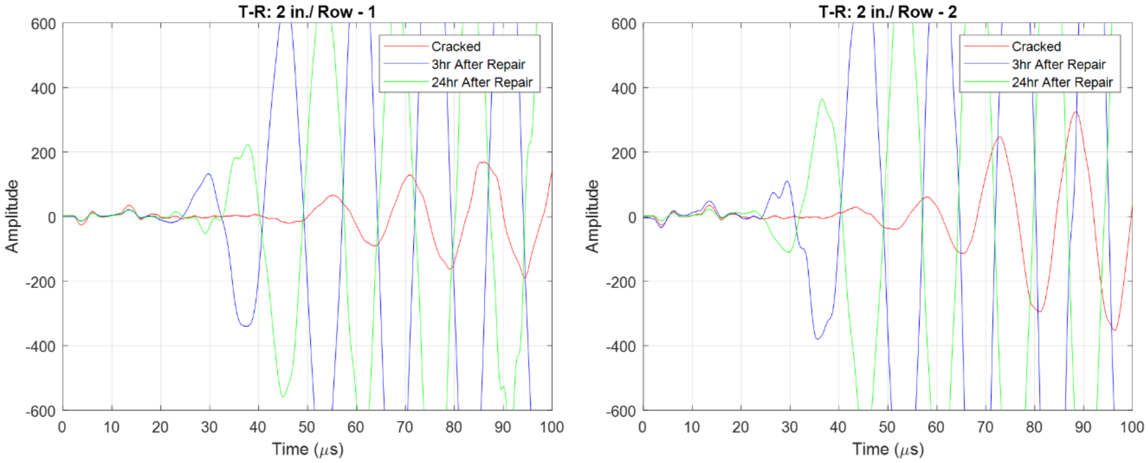
T-R: 2 in./ Row - 1
T-R: 2 in./ Row - 2
Cracked
3hr After Repair
24hr After Repair
Amplitude
Time (μs)
600
400
200
0
-200
-400
-600
0
10
20
30
40
50
60
70
80
90
100

(c)

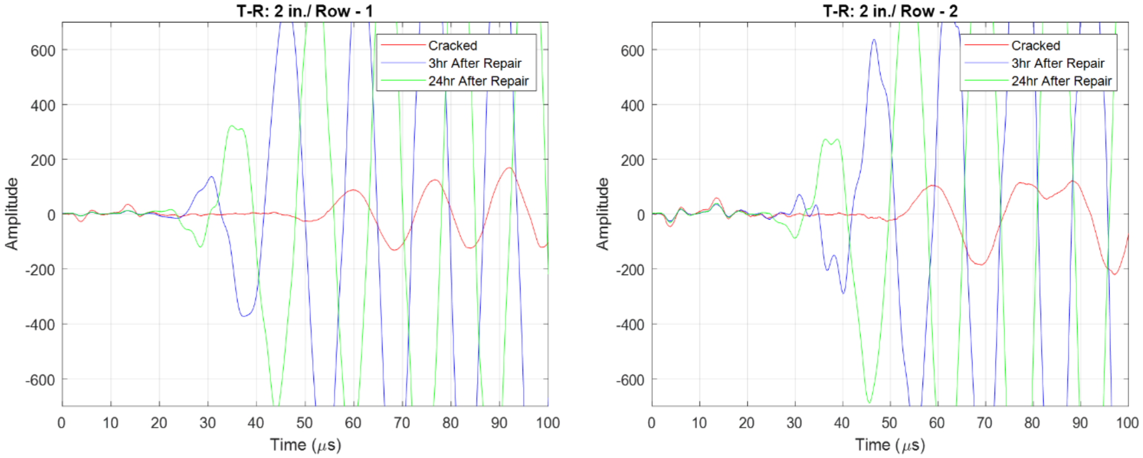

(d)

Figure 64. Time of arrival trend obtained at different time intervals post-repair of the inclined crack regions with crack depth of (a) 0.5", (b) 1", (c) 1.5", and (d) 2"

Effect of crack repair on signal amplitudes

This section discusses the observation made in the amplitude of the transmitted signal for different crack depths. All the signals were postprocessed to a similar data acquisition gain whenever needed. Figure 65 shows the results for the repaired state comparisons of the straight crack. For the 0.5" crack depth, the amplitude showed a measurable increase in the amplitude of the initial peaks of the transmitted signal, demonstrating effective transfer between the transmitter and the receiver. It is to be noted that no specific peak was investigated to arrive at this conclusion. The overall shape of the signal in the first 200 µs was compared, as this will contain most of the surface wave before other modes, including boundary reflections, reflection from the rebar, or converted modes, start appearing at later times, which are not of interest. The amplitude increment was consistent across both inspection rows. A noticeable decrease in the signal amplitudes was observed from 3-hour to 24-hour post-repair windows, which aligns with the previously discussed hypothesis that an initial increase in the amplitude is a result of filler material having a higher apparent stiffness than the regions in the initial phase of hardening, and a slightly relaxed stiffness once fully cured. This trend was observed over many instances except the inspection at Row 2 of 2" crack depth, where the signal transmission in the 24th hour period was significantly higher than the 3-hour inspection. Despite one such outlier, overall, the amplitudes in the repaired state remained consistently higher than the cracked state of the cracks with depths of 1", 1.5", and 2" across both rows. Therefore, it can be stated that the amplitude change serves as a secondary factor to observe to establish the efficacy of the crack repair.

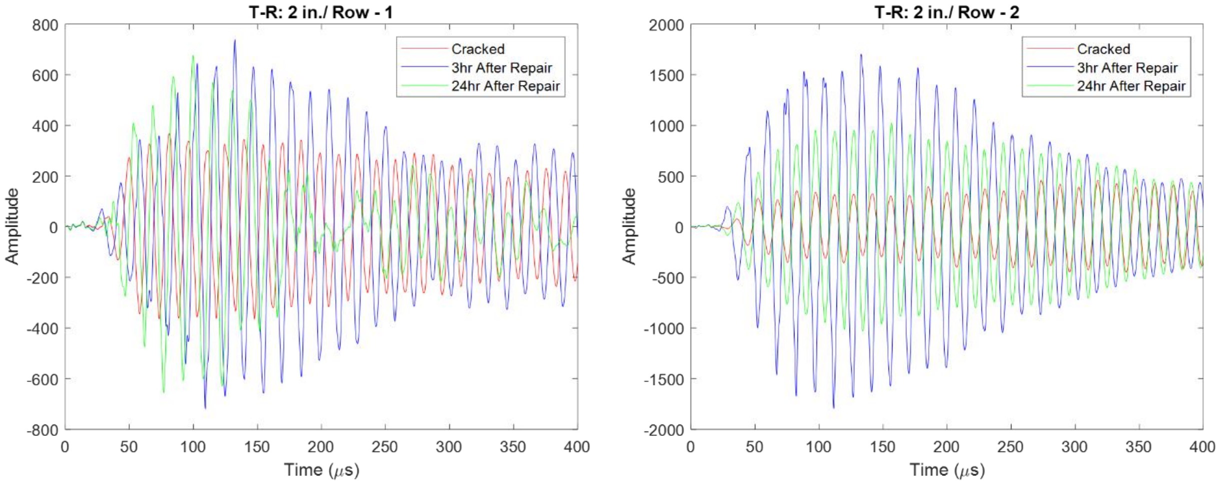
T-R: 2 in./ Row - 1
T-R: 2 in./ Row - 2
Cracked
3hr After Repair
24hr After Repair
Amplitude
Time (μs)
800
600
400
200
0
-200
-400
-600
-800
2000
1500
1000
500
0
-500
-1000
-1500
-2000
0
50
100
150
200
250
300
350
400

(a)

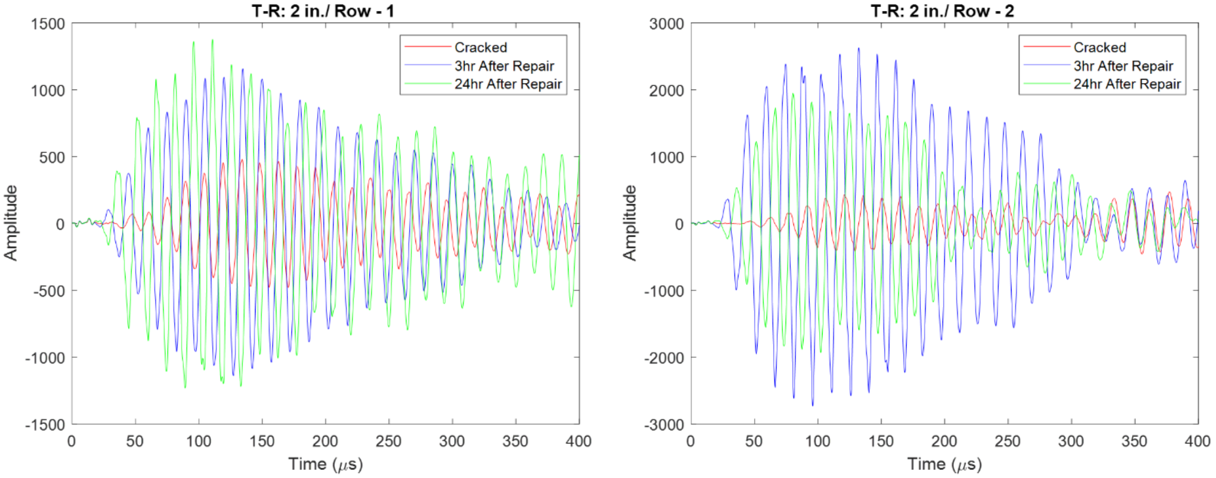
T-R: 2 in./ Row - 1
T-R: 2 in./ Row - 2
Cracked
3hr After Repair
24hr After Repair
Amplitude
Time (μs)
1500
1000
500
0
-500
-1000
-1500
3000
2000
1000
0
-1000
-2000
-3000
0
50
100
150
200
250
300
350
400

(b)

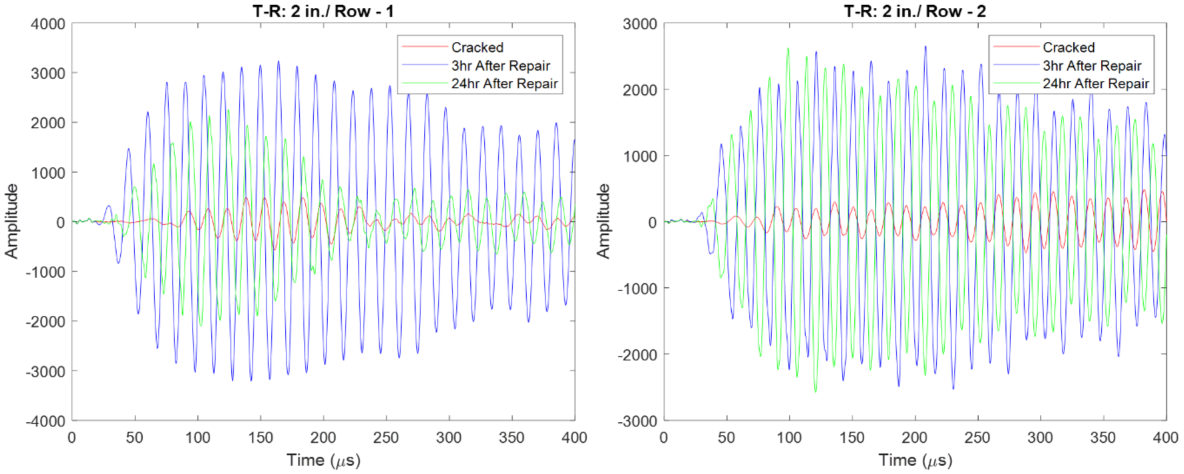
T-R: 2 in./ Row - 1
T-R: 2 in./ Row - 2
Cracked
3hr After Repair
24hr After Repair
Amplitude
Time (μs)
4000
3000
2000
1000
0
-1000
-2000
-3000
-4000
3000
2000
1000
0
-1000
-2000
-3000
0
50
100
150
200
250
300
350
400

(c)

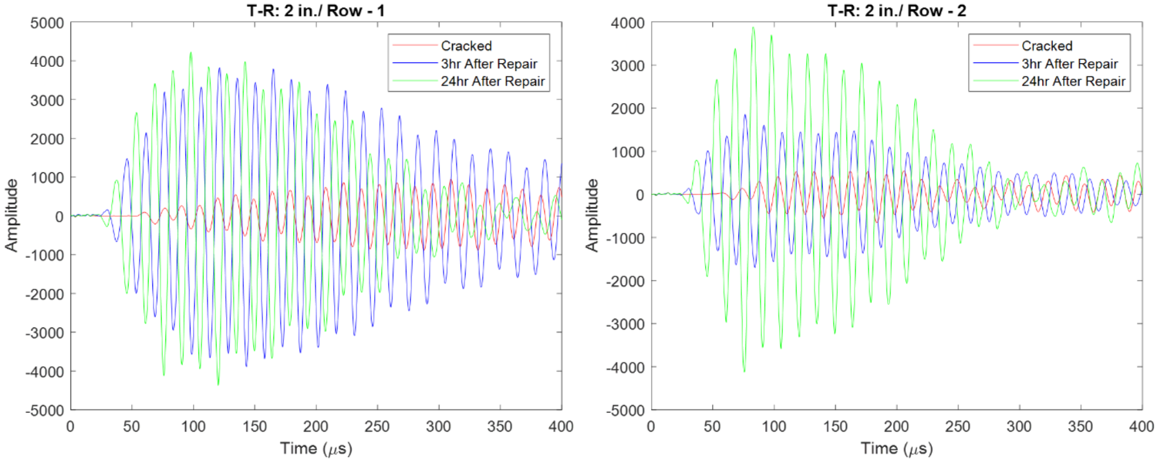

(d)

Figure 65. Transmitted signal amplitudes obtained at different time intervals post-repair of straight crack regions with crack depth of (a) 0.5", (b) 1", (c) 1.5", and (d) 2"

Similarly conclusive yet slightly different observations were made regarding the repaired state of the inclined crack (Figure 66). For a 0.5" crack depth, the amplitude of the 24th-hour signal was overall the highest in both inspection rows, with 3-hour results relatively similar to the crack. Although a 0.5" crack depth will have relatively less interaction with the 50 kHz surface wave, its repair still showed a measurable increase in the signal amplitude. Unlike for the straight crack, where the amplitudes of the 3rd hour results were relatively higher than those of the 24th hour, inclined crack results were either similar in their strength to those of the 24th hour results, or 24th hour results were higher in most instances. Despite such anomalies, the conclusion remains the same that within 3 hours after the crack repair, signal strength showed a reasonable increase in the amplitude of the transmitted signal.

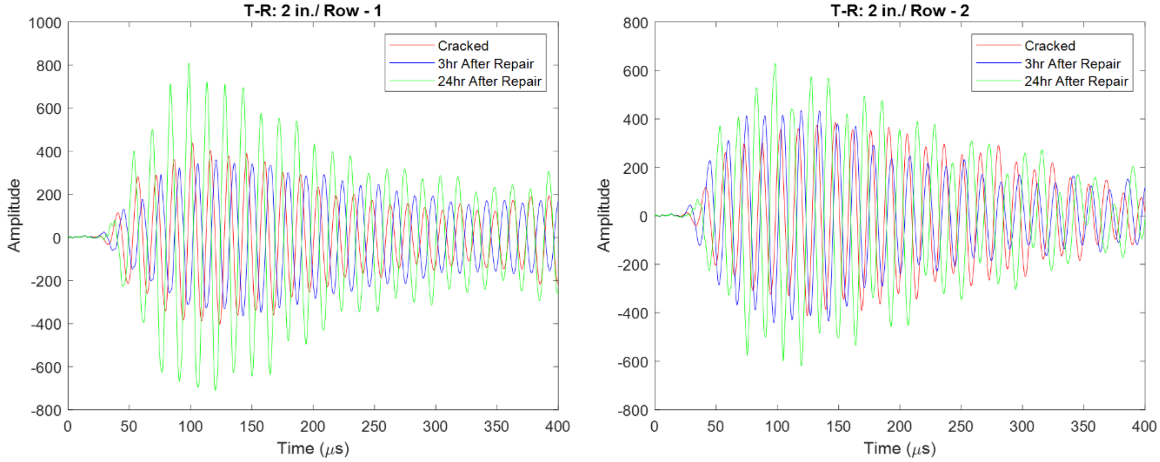

(a)

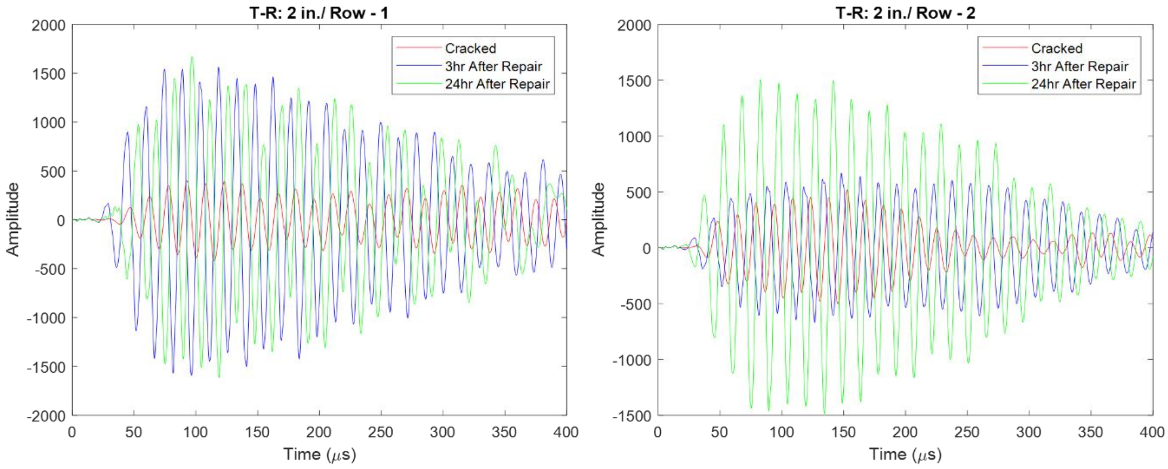

(b)

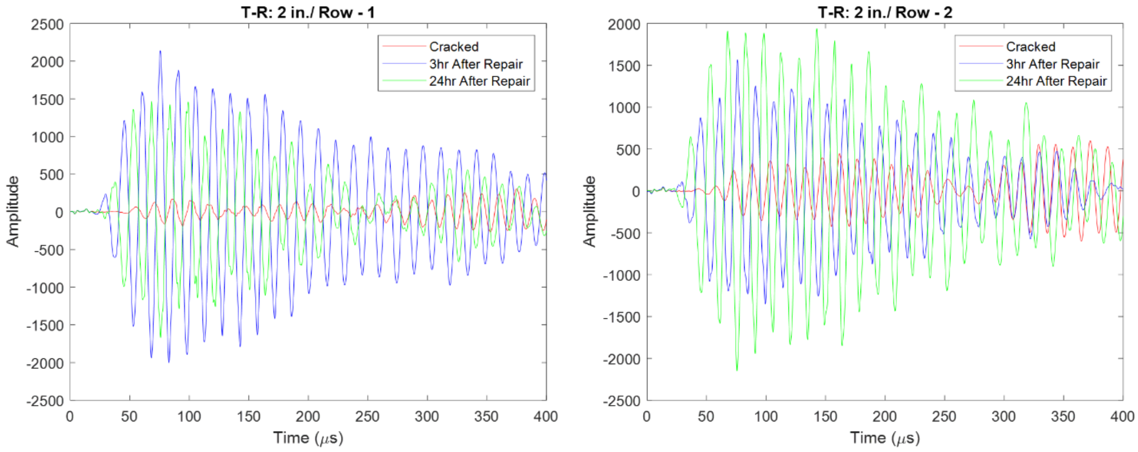

(c)

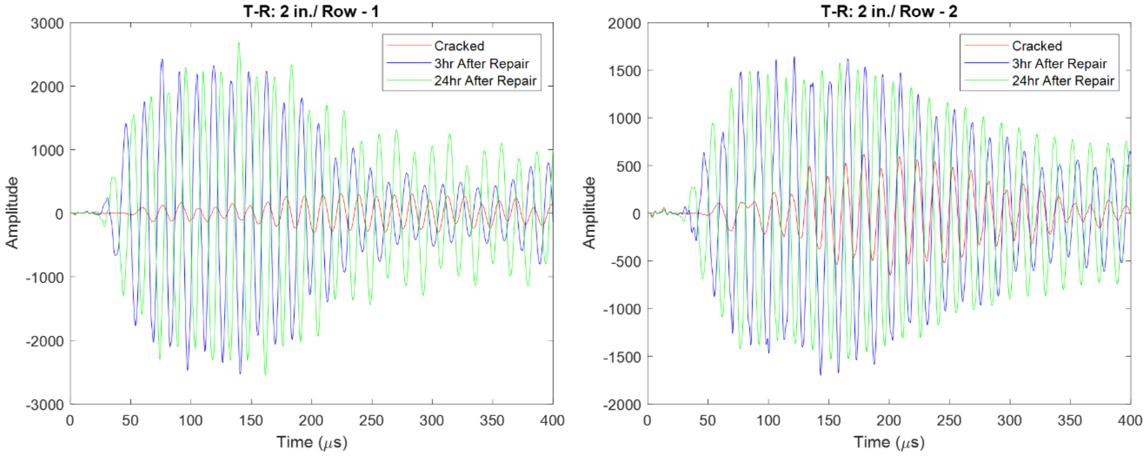

(d)

Figure 66. Trend of transmitted signal amplitude obtained at different time intervals post-repair of the inclined crack regions with crack depth of (a) 0.5", (b) 1", (c) 1.5", and (d) 2"

It is to be noted that no attempt was made to quantify the amplitude gain in the above comparisons, unlike the time of arrival window, where the aim was to observe the time shifts to fall in the same range as the pristine state signals. This was done to develop a solution that acknowledges the time constraints on testing field conditions. As long as the amplitudes of the transmitted signals are visibly higher than the amplitudes of the cracked state, it indicates effective repair.

Special case of a crack touching steel rebar

This section focuses on the crack that touches the rebar. It simulates a scenario where the crack originates from rebar while propagating to the surface, such as in the case of rebar corrosion, where the developed rust volume generates an outward pressure on the concrete, resulting in the crack formation from inside. When investigated for the time of arrival of the transmitted signal, an evident absence of substantial surface wave is observed, as shown in Figure 67. It is marked by the loss of the shape of a smooth harmonic variation as observed in various earlier discussed pristine state signals.

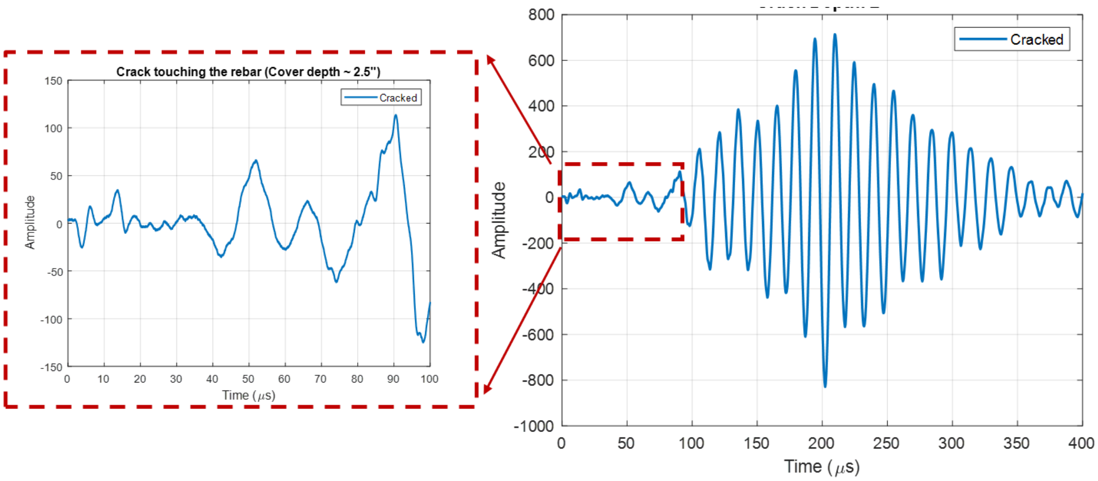

Figure 67. Time of arrival of the surface wave for the crack touching the rebar

Post crack repair, significant restoration in the time of arrival of the surface wave was observed as per Figure 68. The first noticeable change is the arrival of harmonic features of the surface wave components. However, the time of arrival was not consistently between 30-40 µs or earlier as observed for all the repaired states of cracks up to 2". This could potentially be due to subpar bond development between the rebar and the filler material, introducing a slight delay in the time of arrival. In contrast, the amplitudes in the repaired state of the crack showed evident restoration of the signal strength. This scenario reestablishes the benefits of utilizing both the time of arrival and the amplitude of the transmitted signal as a measure to evaluate the efficacy of crack repair.

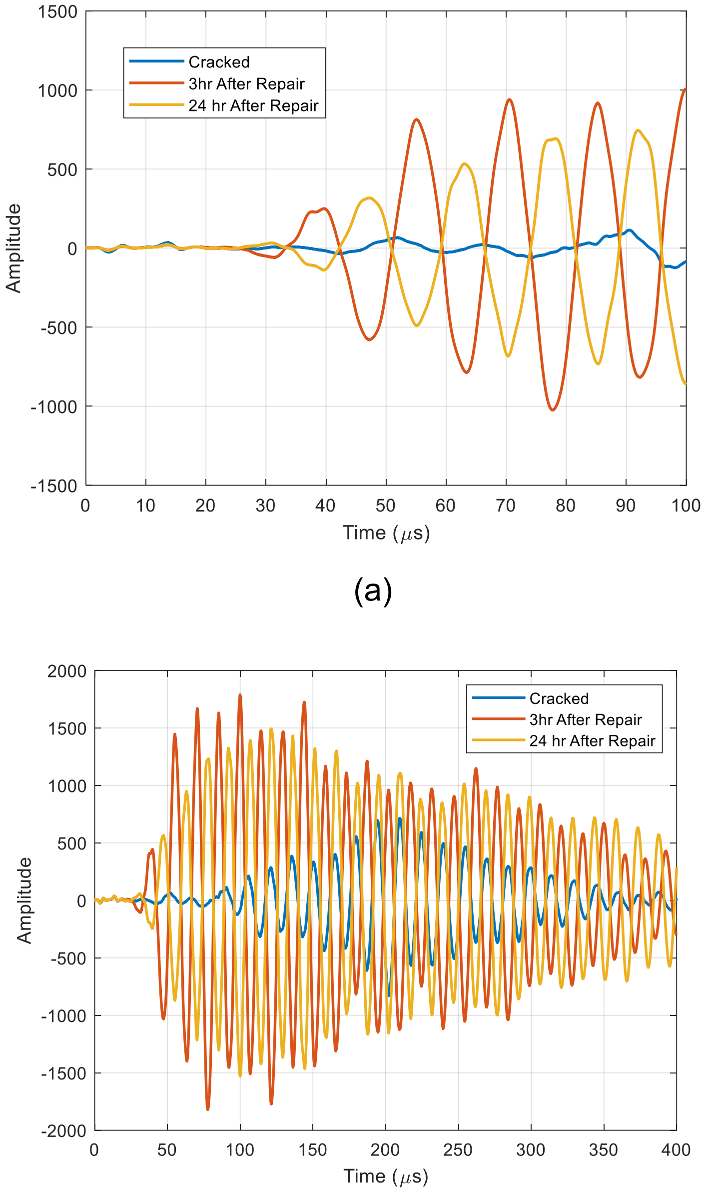

(a)

(b)

Figure 68. Changes in the (a) time of arrival (not normalized to the same scale) and (b) signal amplitude (normalized to the same scale) of the transmitted signal for a repaired crack extending up to the rebar depth.

Schmidt Hammer Tests

Schmidt hammer testing is a nondestructive method of obtaining the compressive strength of concrete. This method of non-destructive testing can be useful for crack repair operations due to the limited time available for the construction crew to test the strength of the repaired locations. Additionally, the compressive strength estimated by the hammer can also be useful in deciding the opening of lane to traffic. The Schmidt hammer needs to be pressed against the surface to be tested for measuring compressive strength. Pressing the hammer completely in a particular orientation makes the spring inside the hammer recoil to a certain distance on the graduated scale along the hammer. This scale reads the rebound number (RN) for the material that corresponds to compressive strength of the material.

The manufacturer of the hammer provides plots that correlate the RN generated from the hammer test to a specific compressive strength. However, the rebound number from the hammer depends on the elastic modulus of the surface being hit. Thus, the compressive strength from the manufacturer supplied graphs also depends on relationship between compressive strength and elastic modulus for the type of material being hit by the hammer. This relation is not the same for any other type of concrete as normal concrete. Hence, for a different class of materials like rapid setting patch repairs, the relation between the RN and the compressive strength needs to be established if it is desired to use the hammer for compressive strength testing of such materials. The research team performed a preliminary investigation to evaluate the feasibility of using the Schmidt hammer for patch repair materials developed in this investigation.

The procedure for the hammer testing followed ASTM C805 standard. The standard requires the hammer to be hit at a location with minimum of 2-inches of the edge distance. Additionally, each hit should be one inch apart. Moreover, when testing using the Schmidt hammer, the orientation of hammer and the angle at which it hits the concrete surface affects the RN value.

The Schmidt Hammer reports a compressive strength of the material based on the rebound number and the manufacturer provided strength curves as shown in Figure 69.

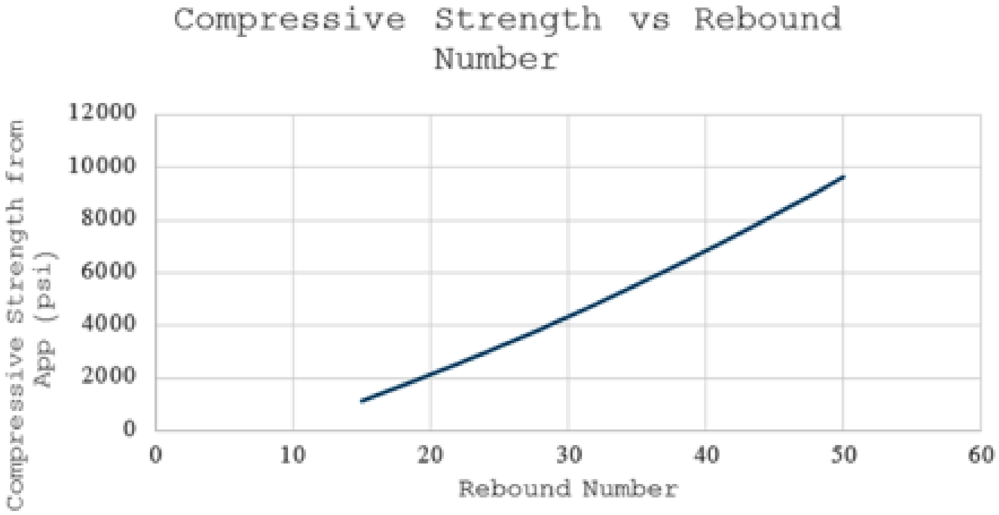

Figure 69. Correlate the RN number generated from the hammer test to a specific compressive strength for normal concrete.

In this research a 26 in. x 26 in. x 8 in. concrete slab with two 0.25 in. pre-placed cracks was constructed as shown in Figure 21. One crack was vertical and has depths of 0.5 in., 1.0 in., 1.5 in., and 2.0 in. The other crack was inclined at 30 degrees measured from the vertical line and has the same depths. Reading taken from the sound concrete in the slab are shown in Table 21. The table shows an average compressive strength of the concrete equal to 5332 psi. This strength was consistent with the compressive strength measured in the lab from concrete cylinders.

Table 21. Measured RN numbers and the corresponding compressive strength

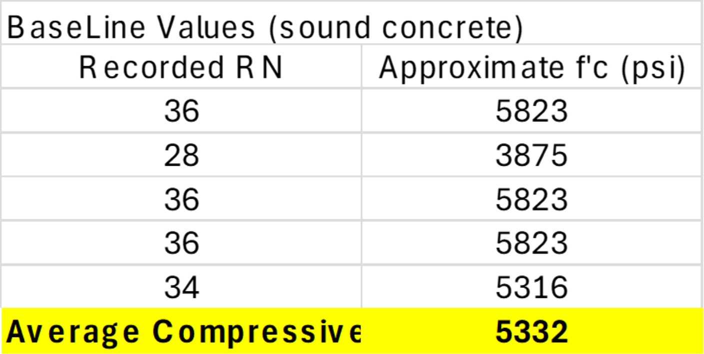

BaseLine Values (sound concrete)	
Recorded RN	Approximate f'c (psi)
36	5823
28	3875
36	5823
36	5823
34	5316
Average Compressive	**5332**

In addition to taking readings from the sound concrete location, readings were also taken at crack locations and near crack locations. Figure 70 shows the crack locations and the markings on the slab. The readings were taken at 1 in. and 2 in. to the left of the crack and at 1 in. and 2 in. to the right of the crack as well on the crack itself. Figure 71 shows markings of the locations where the readings were taken. These readings (or RN numbers) are shown in Tables 22 for the vertical crack and Table 23 for the inclined crack. The tables show the Schmidt hammer recorded RN numbers as well as the corresponding compressive strength using the correlation curve in Figure 20.

The average compressive strength from all data taken near the vertical location is approximately 4800 psi. The average compressive strength from all data taken near the inclined crack location is approximately 5100 psi. These values show that the compressive strength of vertically repaired crack location is about 9.4% lower than the normal compressive strength of the parent concrete material. For inclined crack location, the compressive strength at crack location was about 5100 psi which is approximately 4% less than that of the parent concrete material.

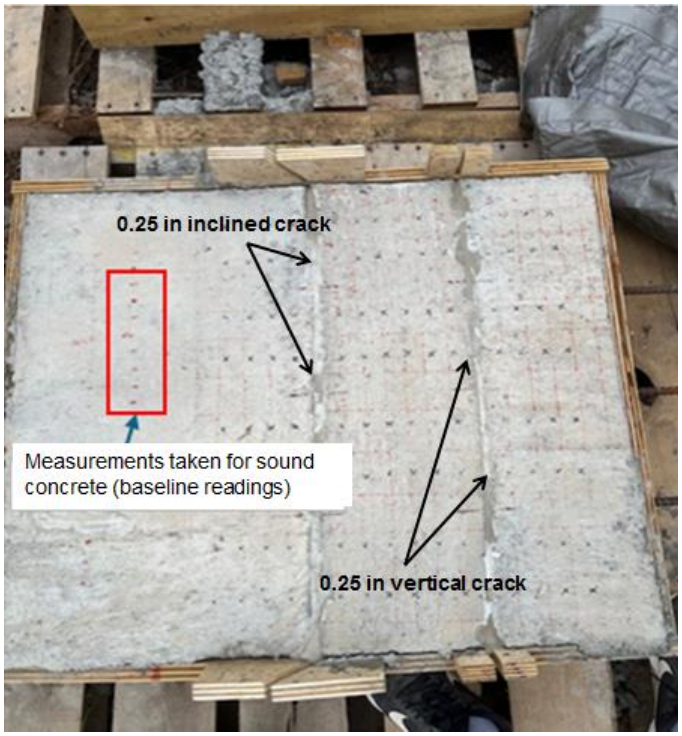

Figure 70. Crack locations in concrete slab specimens and the location of sound concrete where baseline readings were taken

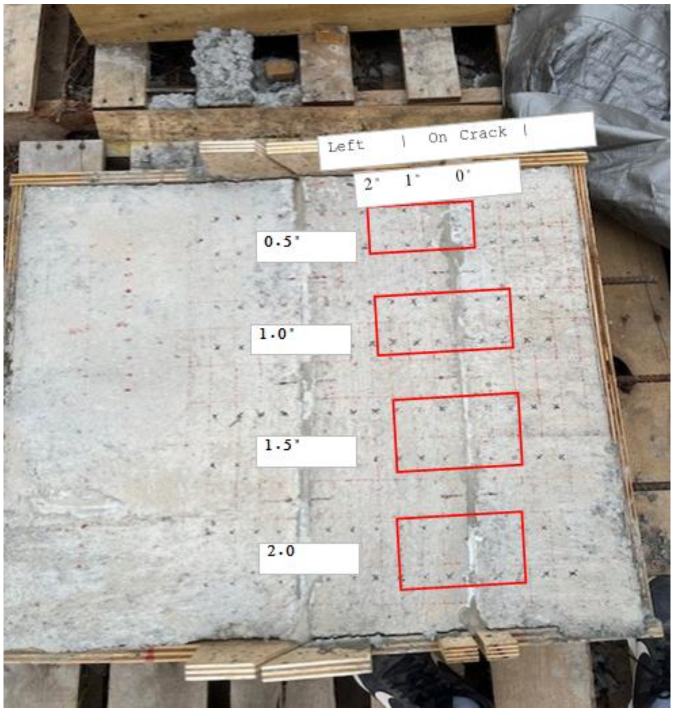

Figure 71. Markings showing locations where readings were taken for each crack.

Table 22. Measured RN numbers and the corresponding compressive strength for vertical crack location

Vertical Crack						
		Rebound Number				
		Distance from the left of the crack (in)		On the crack	Distance to the right of the crack (in)	
Depth of Crack (in)		2"	1"	0"	1"	2"
	0.5	32	14	14	26	35
	0.5	32	33	33	30	26
	1	37	43	43	36	28
	1	34	26	26	32	30
	1.5	32	30	30	26	36
	1.5	28	30	30	32	34
	2	40	35	35	30	26
	2	38	26	26	26	28

Vertical Crack						
		Compressive Strength (psi) from hammer curve				
		Distance from the left of the crack (in)		On the crack	Distance to the right of the crack (in)	
Depth of Crack (in)		2"	1"	0"	1"	2"
	0.5	4820	no conversion	no conversion	3425	5565
	0.5	4820	5073	5073	4342	3425
	1	6067	7662	7662	5823	3875
	1	5316	3425	3425	4820	4342
	1.5	4820	4342	4342	3425	5823
	1.5	3875	4342	4342	4820	5316
	2	6849	5565	5565	4342	3425
	2	6329	3425	3425	3425	3875

Table 23. Measured RN numbers and the corresponding compressive strength for inclined crack location

Inclined Crack						
		Rebound Number				
		Distance from the left of the crack (in)		On the crack	Distance to the right of the crack (in)	
Depth of Crack (in)		2"	1"	0"	1"	2"
	0.5	38	26	19	22	30
	0.5	38	45	31	36	32
	1	42	32	25	28	34
	1	40	32	40	28	32
	1.5	32	28	34	32	36
	1.5	33	28	33	35	36
	2	42	42	34	36	36
	2	31	23	33	42	34

Inclined Crack						
		Compressive Strength (psi) from hammer curve				
		Distance from the left of the crack (in)		On the crack	Distance to the right of the crack (in)	
Depth of Crack (in)		2"	1"	0"	1"	2"
	0.5	6329	3425	1947	2562	4342
	0.5	6329	8214	4580	5823	4820
	1	7385	4820	3212	3875	5316
	1	6849	4820	6849	3875	4820
	1.5	4820	3875	5316	4820	5823
	1.5	5073	3875	5073	5565	5823
	2	7385	7385	5316	5823	5823
	2	4580	2787	5073	7385	5316

The Schmidt Hammer is a simple non-destructive test that can provide an approximate value for the compressive strength for repaired crack locations. More tests on repaired crack locations in the lab and in the filed using the Schmidt Hammer can provide very good database that can be used to get better accuracy from Schmidt Hammer tests.

Conclusions and Recommendations

Summary of findings from laboratory testing

Laboratory investigations were conducted on brick specimens using 70 kHz and 140 kHz ultrasonic signals to examine the relationship between crack depth and ultrasonic signal transmission. Signal propagation was recorded over a fixed distance, and the collected data were analyzed in terms of time of arrival, amplitude, and similarity index. When compared with each specimen's pristine baseline, increasing crack depth was found to cause a progressive delay in signal arrival, a reduction in amplitude, and a decline in similarity relative to the undamaged state. In the repaired state, the signals demonstrated a gradual recovery in amplitude, approaching their original pristine condition. However, due to the limited specimen dimensions, significant boundary interference was observed, making it challenging to isolate distinct peaks for direct correlation between time delay and crack depth.

To quantify these effects, the dB-drop method based on amplitude comparison was employed and found effective in representing both the influence of crack depth and the repair efficiency for partial and complete crack filling. Conversely, correlation coefficient–based analysis yielded inconsistent trends during progressive monitoring of the repair process. Furthermore, results obtained from both 70 kHz and 140 kHz frequencies were inconclusive in establishing a definitive relationship between the repair condition and the corresponding signal changes. Given the dependence of such insights on the pristine baseline, substantial variations in the pristine signal profiles across different specimens were noted, which highlights the need for enhanced signal interpretation algorithms, particularly for field applications where a pristine baseline may not be available.

Making a groove near the entry port helped in allowing the repair material to flow deeper into the crack and minimize the pressure near the entry port. Having a groove along the whole crack can be helpful in the injection process and in holding the repair material in place. The repair material is compatible with the concrete parent material which provides very good adhesion between the two materials and better durability. The repair material is expected to be compatible with ultra-high-performance concrete (UHPC) which is being used more in bridge deck overlays.

Summary of findings from field testing

For the successful use of 50 kHz UT for evaluating the effects of cracks in field settings, followed by the quality of their repair, the following recommendations are made based on the learnings of this study. It is assumed that at the time of inspections, inspectors are familiar and prepared with their UT setup, in the context of timely system setup, possessing shear transducers specific to their needs, a data acquisition (DAQ) unit, a laptop with relevant DAQ software, and data processing tools such as MS Excel. These recommendations are focused on scenarios where the inspectors do not have limited or no prior knowledge of the structure in terms of material properties and design. At no stage will it be desired to have the baseline of signal transmission in undamaged or newly installed infrastructure.

- Firstly, inspectors will aim to identify regions that they would pass as pristine regions through visual inspections. These regions should be marked for their later identification if required. Sufficient attempts should be made to identify such regions in diverse sections of the structure to include the effects of boundaries, rebar positions, and orientations. These sections will be utilized to develop the signature features of the signal transmission in the pristine regions. The main parameter to observe in such sections is the time of arrival of the surface at the receiver.

- Once the pristine regions are identified, signal transmission with 2" separation between the transducers will be recorded at multiple locations. Given the variability of contact conditions, it is desirable to achieve sufficient SNR, which can be controlled by applying sufficient gain to the signal (a common feature in most UT setups). Furthermore, an average of at least three signals at the same inspection points will be used for comparison. It will reduce the effects of manual factors in DAQ, such as varying contact pressure and contact conditions. These signals will then be postprocessed to extract the time of arrival signature of the surface wave. For this analysis, sufficient resolution should be available to zoom to specific time windows (within the first 100 μs) to identify the arrival of the surface wave. Furthermore, it is desirable that the inspectors can synchronize the zeroth second of the A-scans while making these comparisons. In most modern UT-based DAQ systems, it is either pre-calibrated or done using a synchronized trigger between the signal generation and the signal reception. It is not required to convert the signals to the same scale, as it may affect the peak strengths. This step should provide a reasonable range for time of arrival window, which demonstrates signal transmission in visually pristine conditions. The inspectors should aim for sufficient such comparisons between different pristine zones, which will allow them to exclude outliers that may occur due to deteriorating subsurface conditions.

- Next, the inspectors will identify the cracked regions they aim to repair. It is expected to keep a record of the crack width wherever possible, as it may indicate the crack depths. For instance, wider surface cracks can be relatively deeper than finer cracks. The inspectors will then mark 2" separate marks for transducer position, with the points on either side of the crack. It is desired to keep a detailed record during this signal transmission, in terms of the position of the transmitter and the receiver, and the gain applied to the signal during DAQ. It is to be noted that interchanging the transmitter and receiver position may change the signal generation patterns due to inherent differences in the transducer performance and the surface contact condition. For this step, it is desired to maintain sufficient resolution that enough length of the A-scan is recorded (at least up to 400 μs), which will allow for comparison of the time of arrival and amplitude of the transmitted signal.

- Once the cracks are filled with the repair material, the desirable inspection should commence within a 3-hour window, as it will allow sufficient time for the post-processing of the pristine and cracked signals (provided the relevant analysis algorithms are pre-optimized), and the hardening of the repair material. The time of inspection can vary based on the mixed quality of the repair material. It is desirable to have some prior knowledge about this, identified from previously done tests in controlled settings. The signal transmission at the exact same points after the crack repair will be performed, and the signal features will be compared to the pristine and the cracked state, as discussed next.

- For estimation of the effects of crack depths, the cracked state results will be studied to extract the changes in the time of arrival of the surface wave. The delays in the time of arrival of the first measurable peak of the surface wave, when compared with the pristine regions of the structures, serve as the first indicator of the crack-related structural deterioration. However, the ability to measure this time delay may be subject to the crack geometry, as fine cracks may not introduce sufficient time delay to draw any conclusions. In such scenarios, crack faces might still be in contact, which allows reasonable transmission of the surface wave.

- To evaluate the effectiveness of the crack repair, the time of arrival of the surface wave will be compared against the cracked state and the relevant pristine benchmark. It is desirable to observe some gains in the arrival time of the surface wave after the repair. Again, it is not required to perform a scale conversion if the signals were recorded with different initial gains.

- Next is to draw comparisons between the amplitude of the transmitted signals in cracked and repaired states. This step requires the signals to be converted to the same scale wherever needed. Once, compared to the same positions of transducer and receiver, inspectors should be able to make conclusive decisions about the repair quality of the crack. It is desirable to see an increase in the signal transmission strength as an indicator of the crack repair.

- At all times, inspectors are required to make conclusions about the crack repair quality based on the improvements in the time of arrival of the surface wave and the amplitude increase of the overall A-scan.

FEASIBILITY OF AUTOMATED REPAIR AND INSPECTION OF POTHOLE

Introduction

Among all pavement distresses, the pothole is one of the most common, particularly in cold and rainy regions. Potholes form deteriorated sections of pavement, and their growth is accelerated by the penetration of water and freeze-thaw cycles (62). The continued growth of potholes poses a significant hazard to traffic and public safety, making their immediate inspection and repair essential.

Potholes are bowl-shaped depressions that form on roadway pavements due to surface cracking, moisture infiltration, and repeated traffic loading (43). These defects can significantly degrade pavement performance, compromise driving comfort, and cause damage to vehicle components. Pothole repair has become one of the most frequent and critical highway maintenance activities undertaken by transportation agencies. Given that traditional cement concrete typically requires a 28-day curing period, rapid patching materials have become the preferred solution for the expedited repair of concrete pavements. Currently, most state departments of transportation (DOTs) rely on commercially available rapid repair mortars and concrete products, which are listed on their approved materials lists after satisfying performance-based acceptance criteria. Typical repair materials include cement-based materials, epoxy resin repair mortars or epoxy concrete (44). These materials are typically required to reach a certain mechanical strength within a few hours to allow early opening to traffic (45). However, despite their accelerated strength development, rapid repair materials continue to present a number of practical and technical challenges. During pothole repair, manual dumping and overfilling practices frequently lead to excessive material usage (46). Additionally, even with rapid-setting materials, traffic lanes are typically disrupted for 2 to 4 hours, depending on the type of material used and ambient temperature conditions (47,48). This still imposes a measurable level of traffic delay and user cost. Beyond these, studies have reported issues related to poor bond performance at the interface with existing concrete, significant early-age shrinkage, and variability in long-term durability, particularly under thermal cycling and repeated heavy vehicular loads (49,50). These deficiencies often lead to premature repair failures, necessitating frequent reapplication and contributing to elevated life cycle costs and recurring traffic disruptions. A successful rapid repair should be durable, minimize traffic disruptions, and reduce user costs (51).

In recent years, additive manufacturing, particularly 3D printing, has emerged as a promising innovation in infrastructure maintenance due to its advantages in efficiency, precision, and cost-effectiveness. Unlike traditional repair methods, 3D printing allows for precise control of material volume, significantly reducing material waste and overall repair costs. Repair materials can either be printed directly in situ at the damaged location or prefabricated off-site into modular components using 3D printers and subsequently installed. The integration of advanced digital technologies such as 3D laser scanning for damage detection, 3D digital model construction, and autonomous robotic or vehicle platforms enhances the level of automation in pavement maintenance. These integrated systems reduce manpower requirements, minimize exposure to hazardous working conditions, and shorten traffic closure durations, thereby improving operational safety and efficiency, especially under adverse weather conditions or in high-traffic areas (52). As a result, more and more researchers have begun exploring the use of 3D printing equipment and concrete materials for pavement crack and porthole repair, further expanding the potential of this technology in highway infrastructure applications.

Literature Review on 3D Printing for Pavement Crack and Pothole Repair

In 2018, Jackson et al. (53) adapted the RepRap Mendel 90 3D printer by modifying its motion and control system to enable 3D printing of asphalt materials, using a platform gantry three-axis robot, as shown in Figure 72. Unlike traditional 3D printers with moving beds, this design allowed for fixed sample positioning and precise material placement. The system integrated screw extrusion with components including a stepper motor, hopper, and an internally heated jacket to ensure material flow. After extensive empirical optimization, the suitable temperature was identified as 125–135 °C, and extrusion parameters were determined for consistent printing. The experiments showed that 3D printed asphalt exhibits up to nine times higher ductility than cast asphalt while maintaining similar fracture strength, due to microstructural changes such as the formation of crack-bridging fibrous phases. However, the detection device for potential distress such as cracking was not incorporated into this system, which required manual operation for the repair.

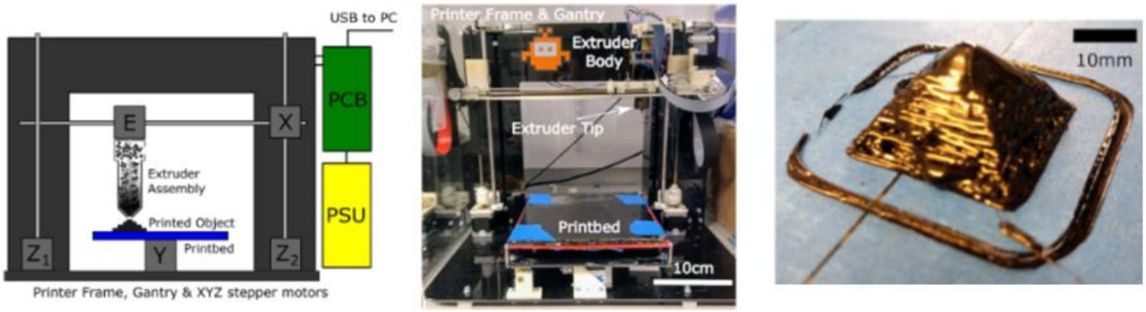

Figure 72. Automated 3D printing system without detection system (53)

Further, Liu et al. (54) developed an automated pavement crack sealing system by modifying a fused deposition modeling (FDM) 3D printer, as shown in Figure 73. This advanced platform combines an image acquisition module, image processing algorithms, and path planning strategies to detect and seal pavement cracks using asphalt emulsion. The procedure begins with capturing images of pavement samples placed on the system platform, after which the detected crack information is converted into G-code instructions for precise printer operation. While the system effectively identifies crack locations, it faces limitations in accurately estimating the volume or depth of the sealant required. This challenge arises from the reliance on traditional 2D image processing methods, such as edge detection, which depend on intensity gradients to outline crack features. These methods are often hindered by factors like inconsistent lighting, shadowing, and low contrast between the crack and surrounding surface, all of which degrade detection accuracy. To overcome such limitations in volume quantification, more advanced scanning approaches such as laser range imaging combined with deep learning can be adopted in the future.

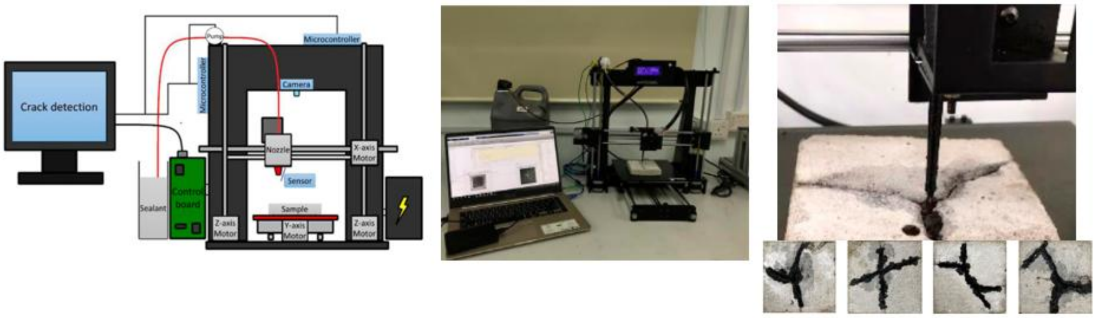

Figure 73. Automated pavement crack sealing system based on 2D image (54)

Recently, Phan et al. (55) customized a 3D asphalt printing system by incorporating a laser scanner, while retaining components similar to those used in previous designs. The system deployed a hot-end extruder mounted on the frame to deposit a mixture of asphalt binder and waste glass into cracks and potholes, as shown in Figure 74. Other components of the system included a stainless-steel binder container, an aluminum extrusion nozzle with integrated heating, a thermistor for real-time temperature monitoring, and a reduction-geared DC motor delivering 60 Nm of torque to drive the screw mechanism. The extrusion speed was finely controlled via a speed controller to ensure consistent flow. An integrated scanning unit, equipped with a commercial laser scanner capable of 0.1 mm precision, was used to generate high-resolution point cloud data of the distressed surface. MATLAB-based image processing converted this data into 3D surface meshes, which were used for slicing and G-code generation.

Overall, despite advanced functionality, the systems above still have several limitations. First, their lack of mobility and flexibility make it poorly suited for the scattered and variable nature of asphalt pavement repair sites. Second, the restricted printing range imposed by the three-axis gantry limits its ability to continuously repair elongated or irregular cracks. While the equipment may not be ideal for in-situ repair applications, it holds promises to prefabricate asphalt repair elements that can be embedded into pavement cracks or shallow potholes.

Figure 74. Automated pavement crack sealing system based on laser scanning (55)

To enhance the mobility and flexibility of 3D asphalt printing, Hebei University of Technology developed a mobile 3D asphalt printing robot, which integrates a lithium battery-powered crawler vehicle, a multi-joint robotic arm, an image acquisition system, a screw feed component, and a central control system (56). Figure 75 illustrates the movable 3D printing robot. The crawler vehicle enables flexible movement on asphalt pavement surfaces, while the robotic arm, with multiple degrees of freedom, ensures precise maneuvering of the extrusion nozzle even in constrained environments. An image acquisition system collects data on surface distress, which is used to construct 3D digital models of early cracks and light potholes. The system is equipped with a 3D printing head capable of extruding rubber-modified asphalt heated to over 140 °C. Based on these models, slicing and path planning are carried out to guide the robotic arm and control the extrusion process.

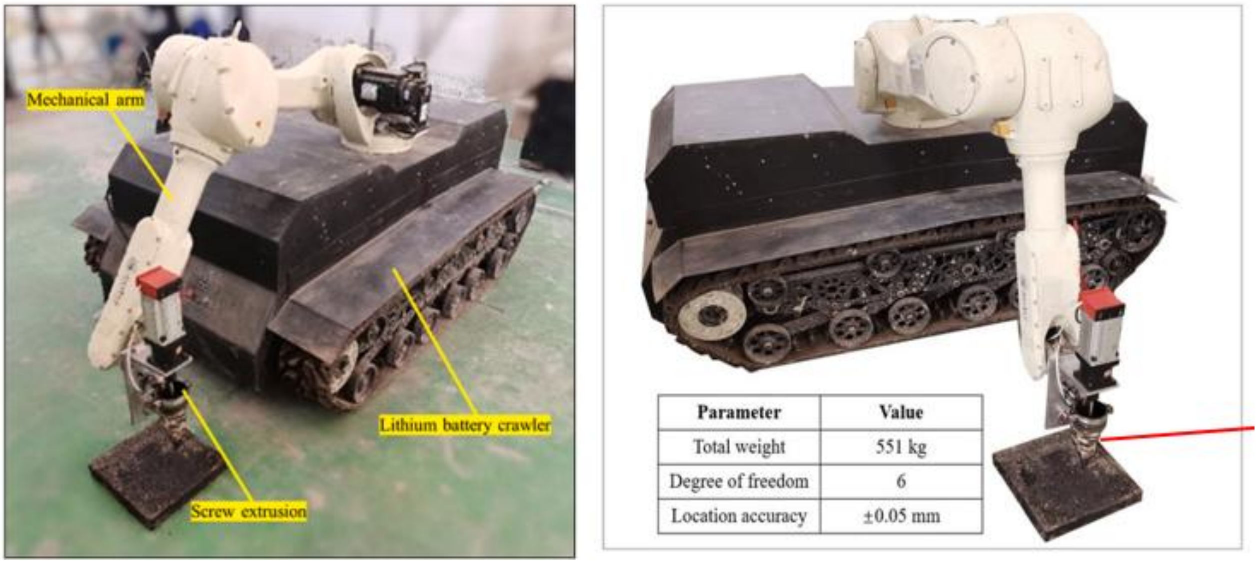

Parameter	Value
Total weight	551 kg
Degree of freedom	6
Location accuracy	±0.05 mm

Figure 75. Movable 3D printing robot (56)

Figure 76 shows the detailed structure of the asphalt 3D printer, which was designed with three primary components: a mobile gantry platform for controlling movement and printing precision, a strip heating device capable of maintaining temperatures between 0–200 °C with a control accuracy of 0.2 °C, and a screw extrusion system equipped with a 3 mm nozzle. The printability was highly sensitive to temperature and extrusion speed. At approximately 140 °C, the high viscosity of rubber modified 3D printed asphalt caused uneven droplet-like extrusion due to insufficient flowability. Optimal printability was observed between 150 °C and 160 °C, where the material extruded uniformly in continuous strips. However, temperatures above 160 °C led to cohesion loss and filament salivation. A printing speed of 1 cm/s yielded the most uniform filament, with a width closely matching the nozzle diameter, indicating optimal material balance for continuous and buildable asphalt filament formation.

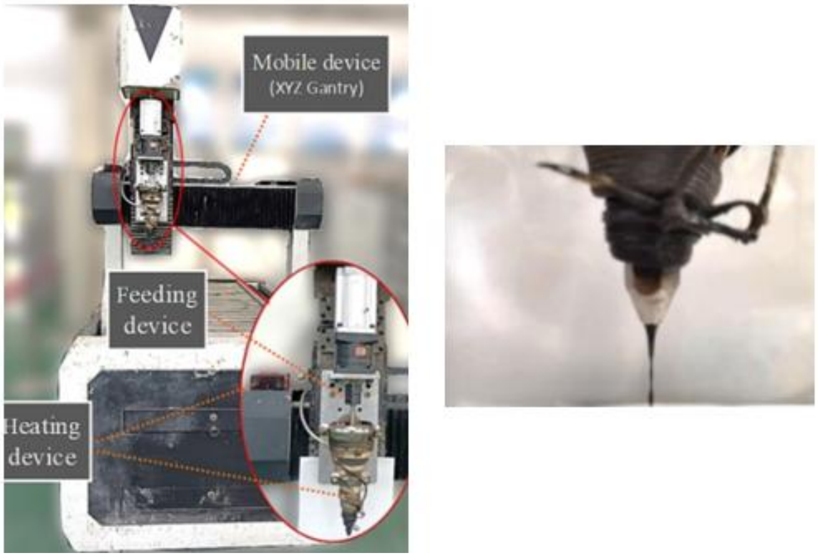

Figure 76. Asphalt 3D printer (Gong et al. 2022)

In 2019, Dr. Jackson's research team, in collaboration with Leeds University, developed a UAV-based 3D asphalt printing robot (58), as illustrated in Figure 77. The system integrates a 3D asphalt printing device onto a UAV platform, enabling flexible, large-area mobility. Asphalt material is sprayed directly onto damaged pavement surfaces based on real-time pavement condition detection, aiming to prevent further deterioration. This approach enhances the flexibility of asphalt pavement maintenance. However, the system has certain limitations: (1) it is not suitable for repairing deep cracks or potholes; and (2) the UAV's endurance and payload capacity require further improvement. As such, this technology is best suited for the treatment of fine, dense surface cracks.

Figure 77. UAV equipped with 3D asphalt printing device (58)

In 2018, Yeon et al. (59) proposed and demonstrated a novel method for repairing spall damage on concrete roads using 3D printing technology. Instead of traditional cast-in-place concrete repair, which requires road closure for at least seven days, they developed a prefabricated concrete patch that can be installed in just 2 hours. The process involves capturing images of the damaged area using a smartphone, generating a 3D model via photogrammetry, and printing a plastic formwork using a 3D printer, as shown in Figure 78. Fresh concrete is cast into the formwork and cured under control conditions for 28 days. The hardened patch is then glued to the damaged surface using a high-strength adhesive. This method significantly reduces road closure time and associated indirect costs, while maintaining sufficient shear strength. However, this delayed readiness (28 days curing) remains a practical concern that could affect the real-world adoption of the technique.

Figure 78. In-situ concrete pothole repair (Yeon et al. 2018)

Literature Review on 3D Scanning of Pothole

The development of computer vision has facilitated 2D imaging-based pothole detection. Early approaches relied on traditional image processing, such as pattern recognition with hand-crafted features (67,77) or edge-detection based on greyscale distribution (72). Machine learning methods, like using Support Vector Machines (SVM) to differentiate textures (68), were also deployed. However, all these 2D methods are highly susceptible to environmental noise, such as uneven illumination, shadows, and water stains. The advance of deep learning, particularly Convolutional Neural Networks (CNNs), significantly improved the precision of 2D pothole detection by overcoming these background noise issues. Nonetheless, CNNs introduce their own challenge: they require large-scale, manually annotated datasets for training, which is extremely time-consuming and detracts from their overall efficiency and practicality (73,63).

To overcome the limitations of 2D methods, 3D-based methods were developed to acquire the actual geometric information of potholes.

- Low-Cost Sensors: Early systems used sensors like the Microsoft Kinect to detect and measure potholes (66,71), but their accuracy was found to be limited by illumination conditions.
- Mobile Laser Systems (LiDAR): Mobile laser scanning is widely used to obtain detailed, high accuracy point clouds for detecting pavement distress (61,63). While these systems provide promising performance, their high cost is a significant barrier to widespread adoption.

- Stereo Imaging: Lately, advances in stereo imaging systems, particularly Structure from Motion (SfM), have made 3D reconstruction more accessible. SfM can reconstruct a 3D model from a series of overlapping 2D images without prior knowledge of the camera positions (78). This low-cost approach has been successfully implemented using UAVs (75,76) and mobile phone-based systems (74).

Building on these low-cost stereo vision approaches, Guan et al. (65) proposed a GoPro-equipped stereo imaging system to obtain pothole depth information. They then incorporated this collected depth information to train a U-Net-based neural network for pothole segmentation and subsequently calculated the volume from the resulting binary map. While effective, this method still relies on a deep learning model and its associated needs for a large training dataset. More recently, Pan et al. (73) proposed a 3D profile-based solution using a similar GoPro system but replaced the deep learning segmentation with a pure geometric algorithm (RANSAC plane estimation and region growth).

This study details the methodology of a custom-developed, three-camera 3D scanning system designed for pavement pothole reconstruction. Our methodology aims to provide a robust alternative that avoids the data-dependency of deep learning models and potential geometric instabilities.

Experimental Trials on Pothole Repair with 3D Printing

3D scanning on artificial potholes

To investigate the feasibility of applying 3D printing technology for pothole repair, the first critical step is to accurately reconstruct the geometry of the pothole. This can be achieved through various techniques such as photogrammetry using cameras, laser scanning, and structured light scanning. Among these, laser scanning offers superior precision and reliability, making it well-suited for applications where geometric accuracy is essential.

In this study, laser scanning was selected to capture the detailed 3D geometry of artificial potholes created under controlled laboratory conditions. Two representative potholes with varying depths were fabricated in concrete slabs, as illustrated in Figure 79. To ensure high fidelity in geometric reconstruction, a high-resolution laser scanner with an accuracy of 0.02 mm was employed, as shown in Figure 80. The fine resolution of the scanner enabled the generation of accurate point clouds and surface meshes, which are essential for designing a customized 3D-printed patch that fits the pothole contour precisely. The small markers around the potholes serve as known reference points for 3D laser scanners to accurately determine the spatial orientation and position of the scanned objects.

Figure 79. Artificial concrete potholes

Figure 80. Laser scanner

The scanned 3D models for shallow and deep potholes are shown in Figure 81(a) and (b), respectively. The resolution was 1920 × 1080 pixels. The total number of vertices captured in the mesh were 3,242,527 and 4,444,393 for shallow and deep potholes, respectively. The deep pothole exhibits greater vertical variation, sharper edges, and more pronounced depressions, indicating significant material loss and surface roughness. In contrast, the shallow pothole presents a relatively smoother profile with smaller depth gradients and fewer abrupt changes, suggesting that the damage is more superficial and confined to the surface layer.

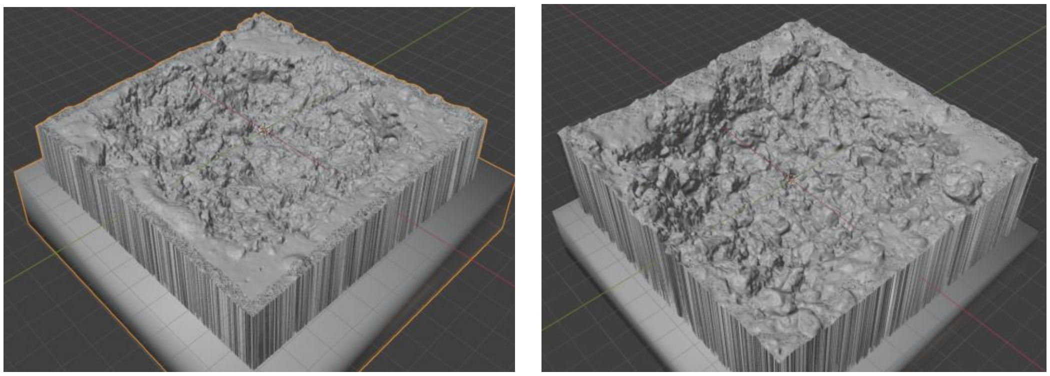

(a) (b)

Figure 81. 3D model of: (a) Shallow pothole, (b) Deep pothole

3D printing of pothole frame

The 3D printing of scanned pothole models can be implemented in two primary forms: printing a hollow frame that matches the pothole geometry or fabricating a solid patch material. Currently, various 3D printing technologies are available, such as stereolithography (SLA), selective laser sintering (SLS), digital light processing (DLP) and so on. In this study, SLA was selected due to its high resolution and geometric accuracy, which are critical for capturing the fine details of pothole contours. The printing was performed using the Form 4L machine from Formlabs, a commercially available high-resolution SLA printer. During the printing process, multiple errors occurred within the 3D printing software platform, despite the scanned models functioning correctly in the modeling software associated with the laser scanner. This issue led to additional processing time and troubleshooting, likely due to incompatibilities between different 3D modeling software environments.

Figure 82 illustrates the 3D-printed frame for a shallow artificial pothole. The printing material used was Rigid 10K Resin, which, according to Formlabs specifications, possesses an ultimate tensile strength of 88 MPa, a tensile modulus of 11 GPa, and a flexural strength of 158 MPa. While these values are significantly lower than those of traditional pavement materials such as concrete or asphalt, Rigid 10K is among the stiffest resins available for SLA printing. During printing the pothole frame, a key challenge was that the scanned model typically represents only a surface shell without defined thickness, requiring converting the surface mesh into a volumetric object. This conversion can introduce geometric inconsistencies, particularly between the inner and outer surfaces, as seen in Figure 82 (a) and (b). Such discrepancies may be less critical when the shell is thickened outward from the inner surface, as the inner surface of the printed frame, which is responsible for shaping the patch material, retains the accurate geometry of the pothole.

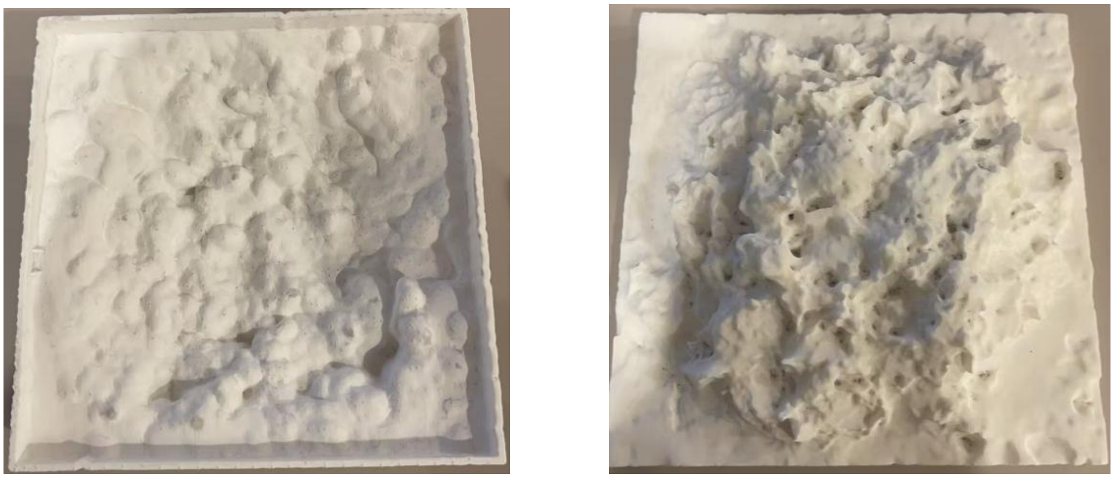

(a) (b)

Figure 82. 3D-printed frame for shallow artificial pothole: (a) inner surface, (b) outer surface

In order to evaluate the fitness between the printed sample and the artificial pothole, the extended direction of pothole frame in Figure 82 was from outer to inner surface. In this case, the printed frame can be used for evaluation without filling repair material. Figure 83 shows the fitting conditions, and it can be seen that the printed frames do not fit the pothole. Although the printed frame in Figure 82(b) demonstrates high dimensional precision, the limiting factor lies in the geometry of the surface features rather than the printing accuracy itself. Specifically, features with a wide base and narrow tip allow insertion, while features with undercuts or reverse-tapered shapes, such as protrusions with a narrow base and wide tip, cannot be physically inserted into the matching cavity, even if the geometry is accurate.

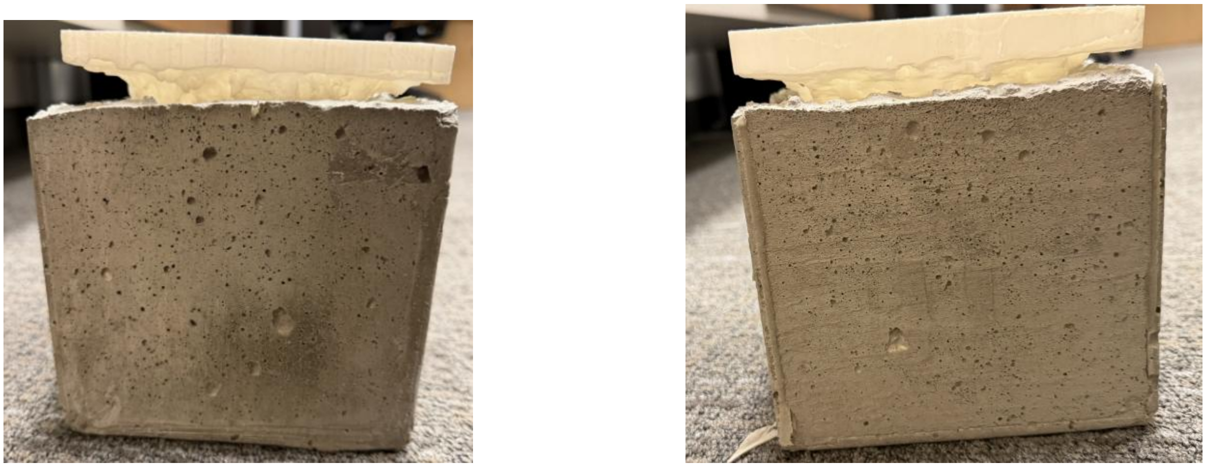

(a) (b)

Figure 83. Fitting conditions of the frame: (a) for shallow pothole, (b) for deep pothole

Grinding and re-scanning of artificial potholes

To address the geometric fitting issues observed during the initial trial of 3D printing, the artificial potholes were mechanically refined using a portable concrete surfacing grinder. The goal of this process was to remove irregularities, such as sharp protrusions, jagged edges, and undercut or reverse-tapered shapes, which made it difficult or impossible to physically insert the printed patch or frame into the cavity, despite accurate scanning and high-resolution printing. By grinding the surface, the potholes were reshaped to have smoother contours and more uniform vertical profiles, thereby ensuring that the scanned geometry could be more effectively reproduced and physically compatible with printed components. Figure 84 (a) and (b) show the shallow and deep artificial potholes after the grinding process, respectively. It can be observed that the overall surfaces are smoother, and abrupt topographic transitions have been minimized. Following the grinding process, laser scanning was performed again to capture the updated geometries of both potholes. As shown in Figure 85, the post-grinding scans exhibited reduced geometric complexity.

(b) (b)

Figure 84. Artificial potholes after grinding: (a) shallow pothole, (b) deep pothole

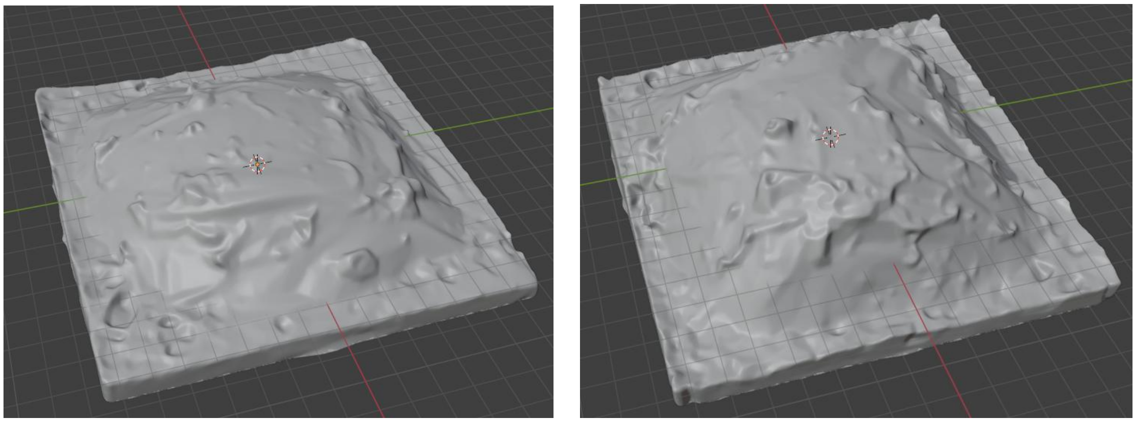

(a) (b)

Figure 85. Scanned model of artificial potholes after grinding: (a) shallow pothole, (b) deep pothole

3D printing of solid patch materials

With the scanned shell models of artificial potholes after grinding, solidified patching materials were printed directly. Different from previous trial of printing pothole frame, directly printing patch materials help save some time and effort on filling and demolding. Figure 86 shows the printed solid patch samples corresponding to the shallow and deep artificial potholes. The printing was performed using the Formlabs Form 4L machine, and Fast Model Resin was selected as the printing material due to its ease of availability. According to manufacturer specifications, Fast Model Resin exhibits an ultimate tensile strength of 62 MPa and a tensile modulus of 2.67 GPa. It should be noted that mechanical performance evaluation is not in the scope of this study, and the selection of materials is only to ensure sufficient physical property for demonstrating shape replication and physical fit in this experimental setup.


(a) (b)

Figure 86. 3D-printed solid patching material: (a) for shallow pothole, (b) for deep pothole

Figure 87 shows the compatibility between the solid patching materials and artificial potholes. It can be seen that for both shallow and deep potholes, after surface smoothing and re-scanning, the solid 3D-printed patches exhibit a close geometric match with the cavity contours. The patches fit well with the potholes, with minimal visible gaps or misalignments along the edges, indicating high fidelity in the reproduction of surface features. This demonstrates that, when combined with appropriate surface preparation, solid patch printing offers a promising method for prefabricating customized repair materials with good physical compatibility.


(a) (b)

Figure 87. Fitting conditions of solid patching materials: (a) for shallow pothole, (b) for deep pothole

To further evaluate the fitness, the outer surfaces of the solid patch materials were scanned again and compared with the original models used for 3D printing. Figure 88 presents the comparison results between the scanned models of the printed materials and the actual potholes for both shallow and deep cases. As shown in Figure 88(a), the printed patch closely replicates the geometric features and surface texture of the shallow pothole, demonstrating a high level of dimensional fidelity and surface conformity. Minor deviations observed near the edges are likely attributed to printing resolution limitations and surface finishing imperfections. Similarly, in the case of the deep pothole shown in Figure 88(b), the reconstructed patch maintains a consistent shape and depth profile compared with the original geometry, suggesting effective volumetric matching and surface adherence.

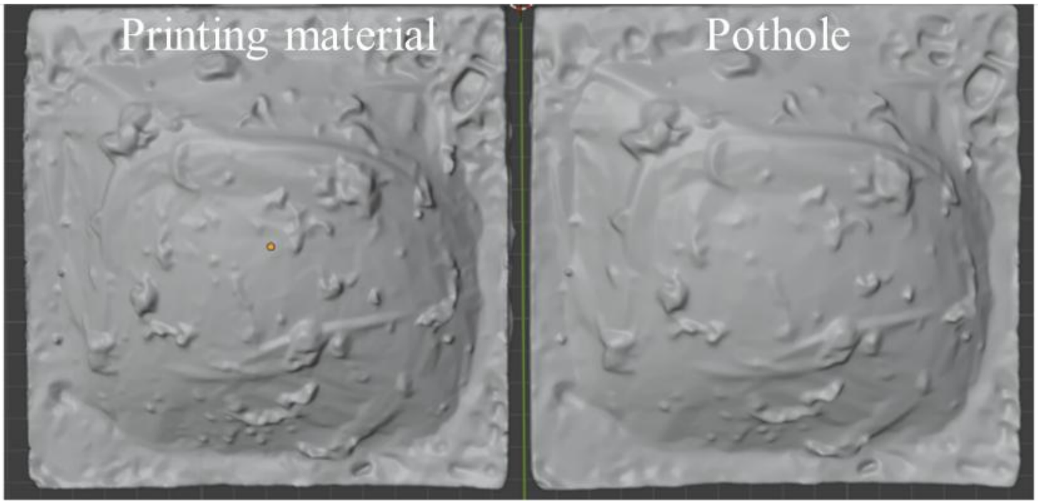

(a)

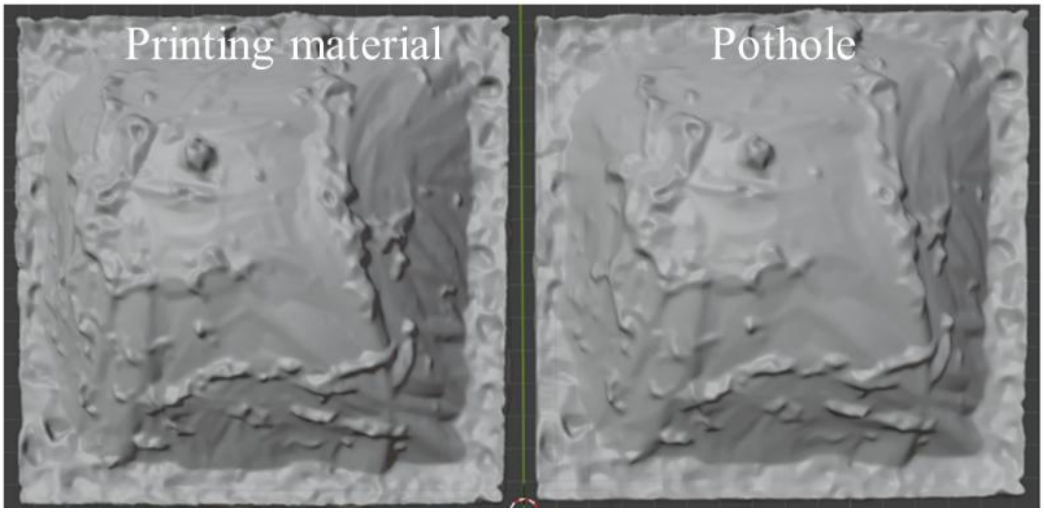

(b)

Figure 88. Comparison of scanned models between 3D printed materials and potholes: (a) for shallow pothole, (b) for deep pothole

In addition to the visual comparison, a quantitative evaluation of the scanned models was conducted, as summarized in Table 24. The results further validate the high geometric fidelity of the 3D-printed patches. For both shallow and deep potholes, the differences in the number of vertices, edges, and faces between the printed models and the original potholes are all below 2%, indicating a close match in surface complexity and topology. These small deviations confirm that the 3D printing method can reliably reconstruct the original pothole geometry.

Table 24 Statistics comparison of scanned models between 3D printed materials and potholes

Pothole geometry		Vertices		Edges		Faces	
		Number	Difference	Number	Difference	Number	Difference
Shallow	3D-printed material	184807	1.1%	553640	1.1%	368830	1.1%
	Pothole	182822		547563		364742	
Deep	3D-printed material	219160	0.2%	656582	0.2%	437421	0.2%
	Pothole	218692		655159		436468	

Low-Cost Imaging Scanning of Pothole Specimens

The specific aims of the current methodology are:

1. To calibrate a fixed, three-camera imaging system's intrinsic and extrinsic parameters.
2. To acquire synchronized images and perform robust feature matching between the middle-left (M-L) and middle-right (M-R) stereo pairs.
3. To generate a dense 3D point cloud of the pavement surface, unified in the middle camera's coordinate system.
4. To segment the pothole geometry from the point cloud, calculate its precise features, and compare with results from a high-resolution laser scanner.

Our approach to 3D reconstruction is built upon the geometric principles of stereo vision, which define the relationship between 2D images and 3D space. The methodology is structured to first establish these geometric principles, then detail the practical steps of calibration and feature matching required to achieve reconstruction.

As detailed in Figure 89, a 3D point (P) in space is projected onto two different camera image planes, creating a pair (P_1, P_2) of corresponding pixels (65). Triangulation is the process of reversing this: calculating the 3D coordinate of the point by using the 2D coordinates of its projections.

This reconstruction is governed by the camera's parameters and their relative positions.

1. Camera Intrinsics (*K*): First, the relationship between a 3D point $[X, Y, Z]^T$ in the camera's coordinate system and its 2D pixel projection $[x, y, 1]^T$ is defined by the camera's internal intrinsic matrix *K*. This matrix contains the focal lengths (f_x, f_y) and the principal point (c_x, c_y). The projection is described by the equation:

$$0_1 - xyz\ camera\ cordinate\colon\ d_1\begin{bmatrix} x_1 \\ y_1 \\ 1 \end{bmatrix} = K\begin{bmatrix} X \\ Y \\ Z \end{bmatrix}$$

$$0_2 - xyz\ camera\ cordinate\colon\ d_2\begin{bmatrix} x_1 \\ y_1 \\ 1 \end{bmatrix} = K\begin{bmatrix} X' \\ Y' \\ Z' \end{bmatrix} \qquad (31)$$

$$where\ K = \begin{bmatrix} f_x & 0 & c_x \\ 0 & f_y & c_y \\ 0 & 0 & 1 \end{bmatrix}$$

where $[X, Y, Z]^T$ is the spatial coordinate of the target point P in O$_1$-xyz camera coordinate system; $[X', Y', Z']^T$ is the spatial coordinate of the target point P in the O2-xyz camera coordinate system; d$_1$ and d$_2$ are the vertical distances from the target point to the camera optical center.

2. Camera Extrinsic (*R*, *T*): When a second camera is introduced, its position and orientation relative to the first are defined by the extrinsic parameters: a 3x3 Rotation matrix (R) and a 3x1 Translation vector (*T*). The relationship between the 3D point's coordinates in the O$_1$-xyz camera's system ($[X, Y, Z]^T$) and the O2-xyz camera ($[X', Y', Z']^T$) is given by:

$$\begin{bmatrix} X' \\ Y' \\ Z' \end{bmatrix} = R\begin{bmatrix} X \\ Y \\ Z \end{bmatrix} + T \qquad (32)$$

3. Triangulation: By combining these equations, a relationship between the two 2D camera coordinates ($p_1\ and\ p_2$) is formed. This geometric constraint is encapsulated by the Essential Matrix (E), which is defined as $E = [T]_\times R$. The Essential Matrix can be solved by using a set of matched feature points from the two images. Once E is known, R and T can be extracted from it using Singular Value Decomposition (SVD).

$$d_2\begin{bmatrix} x_2 \\ y_2 \\ 1 \end{bmatrix} = K\left(R\begin{bmatrix} X \\ Y \\ Z \end{bmatrix} + T \right) \qquad (33)$$

With all known parameters (*K*, *R*, and *T*), the 3D space coordinate $[X, Y, Z]^T$ for any matched pair of points can be calculated by solving the system of projection equations, a process known as triangulation.

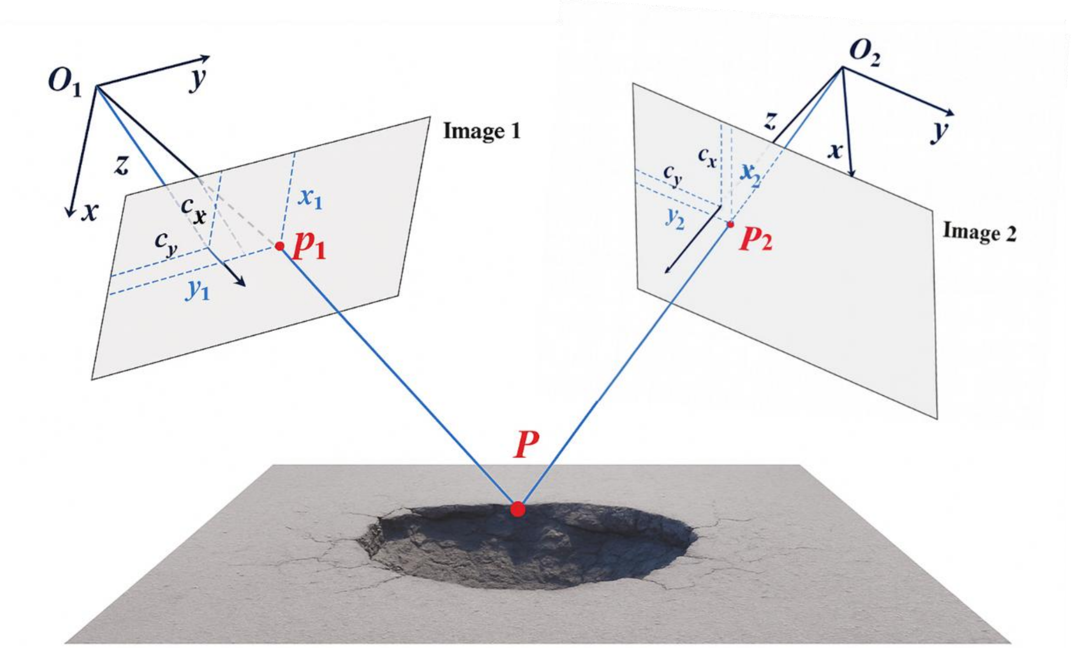

Figure 89. Triangulation principle between 2 cameras and the 3D world

To successfully apply this principle, two tasks must be accomplished: (a) Geometric Calibration: Find the parameters *K*, *R*, and *T* for the three-camera system (for each stereo pair); (b) Feature Matching: Find a large and accurate set of corresponding 2D points between the images for 3D points generation.

System calibration

To find the intrinsic (*K*) and extrinsic (*R*, *T*) parameters for our system, a robust calibration is performed using the OpenCV toolbox. A set of 20-30 images of a known chessboard pattern (as seen in Figure 90) were used to ensure a precise and stable solution.

Figure 90. Chessboard images from different angles

1. Single Camera Calibration: First, each camera (Left, Middle, Right) is calibrated individually to solve its intrinsic matrix (K).

2. Stereo Pair Calibration: The system then calibrates the two stereo pairs ("Middle-Left" and "Middle-Right"). This step uses the matched chessboard corners to solve for the

Essential Matrix (E), from which the Rotation (R) and Translation (T) vectors for each pair are extracted.

Image feature enhancement and matching

To achieve robust 3D reconstruction, a large and accurate set of corresponding points between images must be extracted. The performance of feature matching algorithms is, however, highly dependent on image quality. Pavement surfaces, particularly concrete, often exhibit low local contrast, which can hinder feature detection.

To address this challenge, a two-stage image preprocessing pipeline is applied to enhance feature distinctiveness:

1. CLAHE (Contrast Limited Adaptive Histogram Equalization): This algorithm is applied to enhance local contrast, making subtle textures and aggregates on the pavement surface more prominent.

2. Image Sharpening: A sharpening filter is subsequently applied to further define the edges of these enhanced features.

Following preprocessing, feature matching is conducted using the Scale-Invariant Feature Transform (SIFT) algorithm, selected for its robustness in scale and rotation invariance (Lowe, 2004). This process involves:

1. Detection & Description: SIFT detects scale-invariant key points by identifying local extrema in scale-space. A unique 128-dimensional descriptor is then generated for each key point.

2. Matching & Filtering: A Brute-Force (BF) matcher is employed to find potential nearest-neighbor matches between the descriptor sets from a stereo image pair. Lowe's Ratio Test is then applied to filter out ambiguous matches. Finally, to ensure geometric consistency, the Random Sample Consensus (RANSAC) algorithm is utilized with the previously calibrated Essential Matrix (E) to discard any remaining outliers.

The final filtered sets of 2D matched points serve as the input for the subsequent 3D triangulation step.

Data acquisition system

The core of the system is a custom-built, low-cost scanning system (Figure 91). It consists of three GoPro Hero 11 cameras mounted at fixed, differing angles on a rigid frame. This multi-camera setup provides a wide baseline for accurate triangulation and mitigates potential occlusion zones that can occur with a standard two-camera setup. The camera parameters are listed in Table 25.

A remote control is used to trigger all three cameras simultaneously. This synchronization is critical: it ensures the relative pose (*R, T*) between cameras remains fixed and consistent with the calibration parameters. The GoPro's built-in stabilization, combined with simultaneous capture, makes the system robust against vibrations, allowing it to be mounted on a vehicle for mobile data collection.

Figure 91. 3-camera system and remote control

Table 25 Camera Parameters

Image size	5568px*4872px
Aperture	f2.5
ISO	598
Exposure time	1/143
Lens mode	Linear
Focal length	15mm

Data processing workflow

To apply the theoretical methodology, a practical workflow involving a custom hardware setup and a sequential processing pipeline was established. The practical processing workflow is as follows:

1. Calibration: A one-time calibration is performed to acquire the complete geometric model of the system.

2. Image Acquisition: Simultaneous images of the target pothole (left, middle, right) are captured.

3. Preprocessing: The captured images are processed using CLAHE and sharpening to produce high-contrast images suitable for feature detection, as shown in Figure 92.

(a) left (b) middle (c) right

(d) left (e) middle (f) right

Figure 92. Image processing results

4. Feature Matching: SIFT feature matching and RANSAC filtering are performed on the M-L and M-R image pairs to find geometrically valid corresponding points. Due to the system's geometry, the M-L pair primarily captures points on the right side of the target, while the M-R pair captures the left side (Figure 93). This three-camera configuration effectively mitigates occlusion zones and provides a denser set of geometrically valid corresponding points for the final reconstruction.

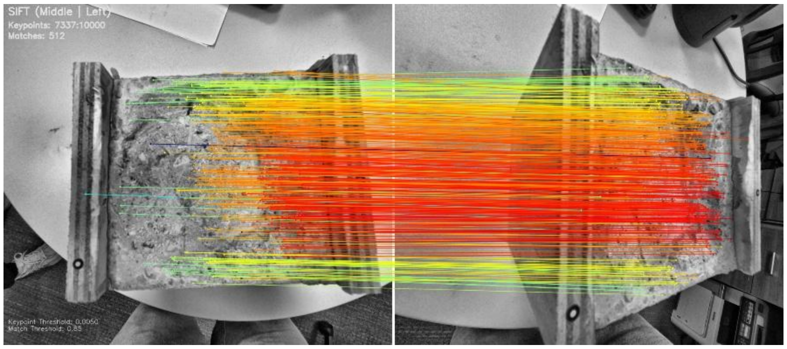

(a) Middle-left corresponding points (512)

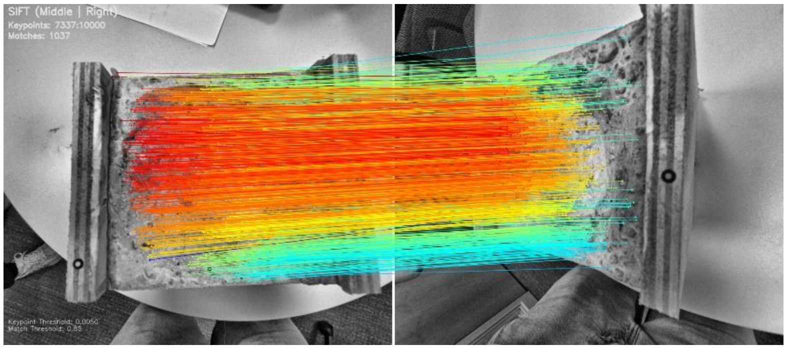

(b) Middle-right corresponding points (1037)

Figure 93. Corresponding points of two stereo pairs

5. Triangulation & Merging: Using the known calibration parameters, these 2D matches are triangulated into 3D coordinates. The two resulting point clouds (from M-L and M-R) are then merged into a single, dense 3D point cloud representing the pothole's geometry (Figure 94).

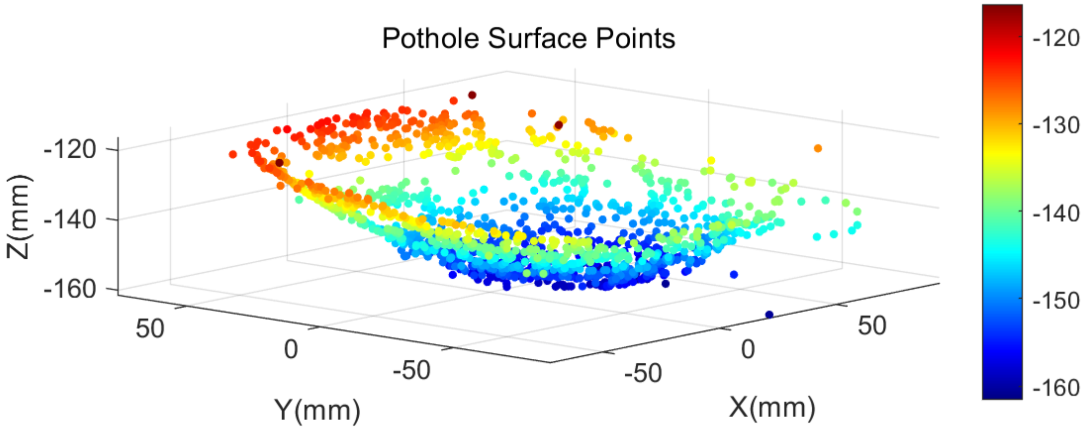

Figure 94. 3D point cloud of the pothole

Pothole segmentation and feature extraction

The output of the workflow is a raw point cloud that suffers from two issues: 1) sparse outliers from matching errors, and 2) arbitrary tilt from the camera's pose. A post-processing workflow is required to clean the data and extract metric features.

First, a statistical outlier removal filter is employed. This algorithm calculates the average distance of each point to its k-nearest neighbors (KNN). For a given N-point cloud P.

$$P=\{p_i=(x_i,y_i,z_i)\}_{i=1}^{N} \tag{34}$$

For each point pi, we define its nearest neighbors (excluding itself) as Nki. The Euclidean distance between pi and a neighbor is:

$$d_{i,j}=|p_i-p_j|_2 \tag{35}$$

The average neighborhood distances for point p_i is then computed as:

$$\bar{d}_i=\frac{1}{k-1}\sum_{j=1}^{k-1}d_{i,j} \tag{36}$$

Across all points, we calculate the global mean and standard deviation of the average distances as:

$$\mu_d=\frac{1}{N}\sum_{i=1}^{N}\bar{d}_i,\sigma_d=\sqrt{\frac{1}{N}\sum_{i=1}^{N}\left(\bar{d}_i-\mu_d\right)^2} \tag{37}$$

Points whose mean neighbor distance exceeds the threshold $T=\mu_d+2.5\sigma_d$ are regarded as outliers and removed, the results are shown in Figure 95.

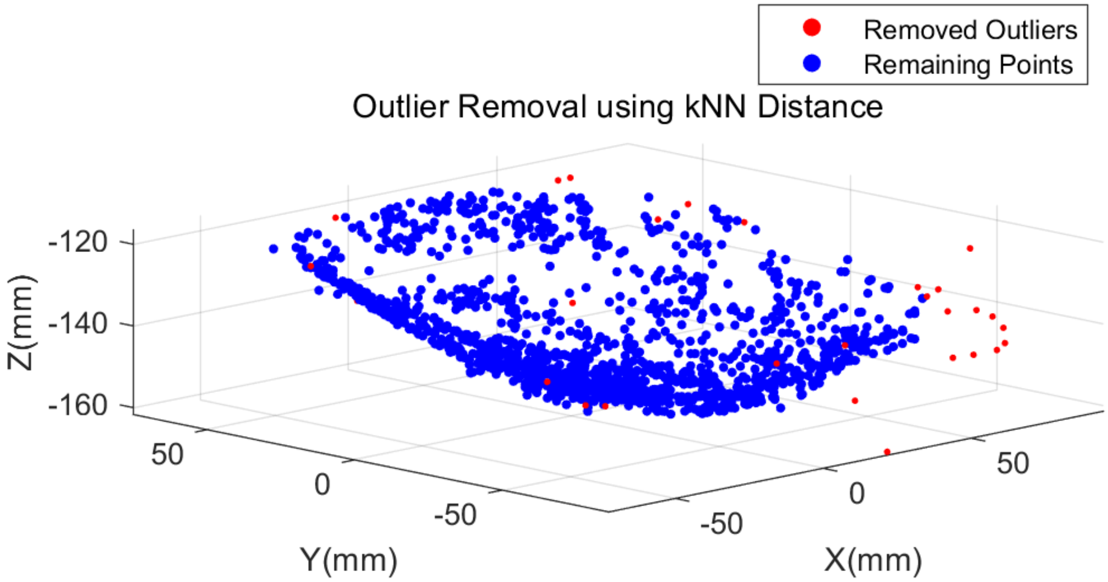

Figure 95. The outliers to be removed

Next, the cleaned point cloud is aligned to be level with the pavement surface. We use Principal Component Analysis (PCA) to estimate the three principal directions of the point cloud. The eigenvector corresponding to the minimum eigenvalue represents the normal vector of the pavement plane. The point cloud is then rotated so that this normal vector aligns with the Z-axis, effectively "flattening" the surface (Figure 96).

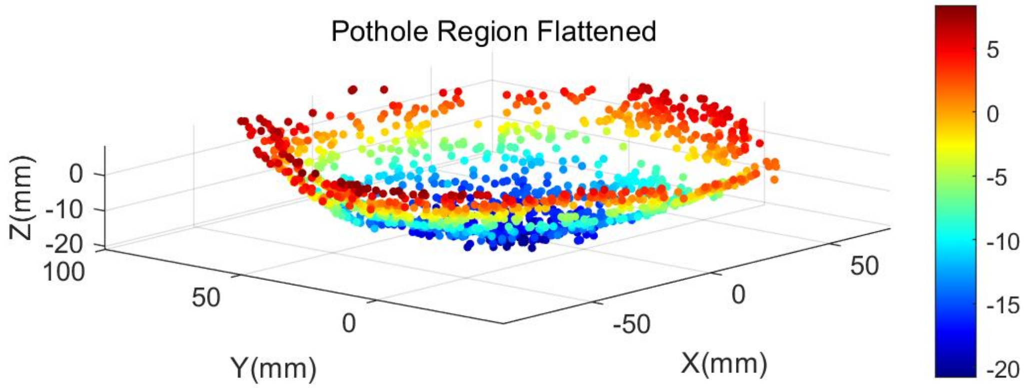

Figure 96. The flattened pothole region

The aligned, discrete point cloud is converted into a continuous surface grid using MATLAB interpolation. To calculate volume, a top reference plane representing the healthy pavement surface must be defined.

Given a flattened pothole surface $P = \{(x_i, y_i, z_i) \mid i = 1, 2, ..., N\}$, where z_i denotes the elevation (with the bottom of the pothole being negative), the goal is to estimate a reference top plane representing the undamaged road surface.

We assume that the top rim of the pothole corresponds to the highest portion of the surface, that is, points with the largest z_i values. The upper rim (edge) points are defined as those with heights above the 80th percentile:

$$\mathcal{E} = \{(x_i, y_i, z_i) \in P \mid z_i > z_{(80)}\}. \tag{38}$$

A reference top plane (Figure 97) is fitted to the edge points by least squares:

$$z_{\text{top}}(x,y) = ax + by + c, \qquad \begin{bmatrix} a \\ b \\ c \end{bmatrix} = (\mathbf{A}^{\mathrm{T}}\mathbf{A})^{-1}\mathbf{A}^{\mathrm{T}}\mathbf{z}, \tag{39}$$

where $\mathbf{A} = [x_i \ y_i \ 1]$, $\mathbf{z} = [z_i]$.

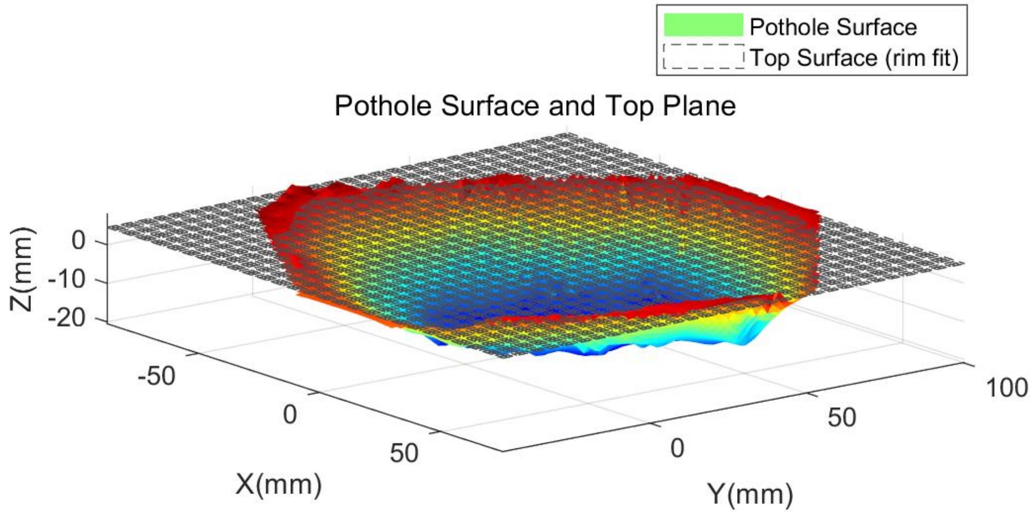

Figure 97. The pothole region surface and top plane

The local depth distribution is then:

$$d(x,y) = \max(0, z_{\text{top}}(x,y) - z(x,y)) \tag{40}$$

From which key geometric quantities are obtained:

$$V = \sum_{i,j} d_{ij} \, \Delta x \, \Delta y \tag{41}$$

$$A_{\text{top}} = \text{Area}\{\{(x_i, y_i) \mid d_{ij} > 0\}\} \tag{42}$$

$$d_{\max} = \max_{i,j} d_{ij} \tag{43}$$

Laboratory Scanning Results and Discussion

To validate the accuracy of the proposed system, a laboratory experiment was conducted on a concrete pothole sample. The geometric measurements derived from our system were compared against a ground truth dataset.

A ground truth model was established by scanning the same pothole sample using a high-precision, industrial-grade 3D scanner (SimScan42, as shown in Figure 98). This produced a high-density point cloud with accuracy up to 0.02 mm, serving as the baseline for comparison.

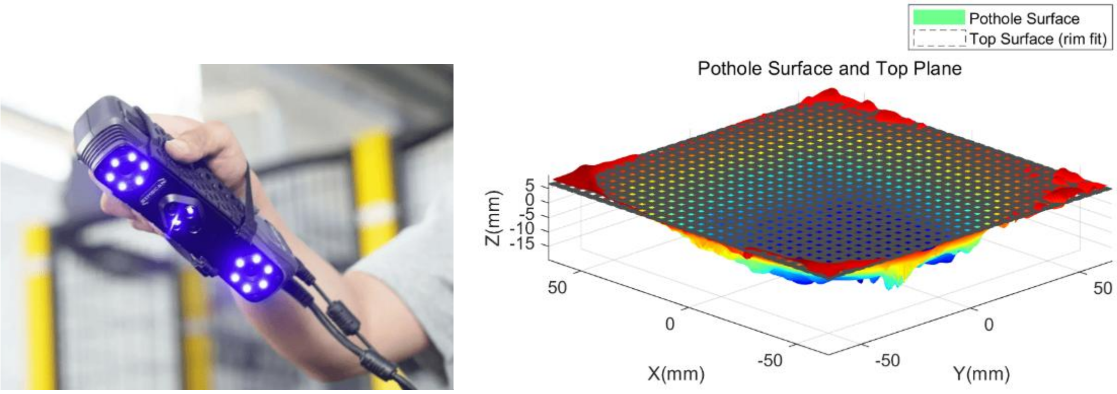

Figure 98. SimScan42 and the scan result for the same pothole

A challenge in comparing the two datasets arose from the significant difference in point cloud density. Applying a fixed percentile to define the top reference plane on both the sparse (our system) and dense (SimScan) point clouds would not result in a geometrically equivalent plane.

To address this, a calibration approach based on maximum depth was adopted.

1. First, the maximum depth of the pothole was calculated using our proposed three-camera system, yielding a value of 25.25 mm.
2. This maximum depth was then used as a fixed control parameter.
3. For the high-density SimScan data, the "top percentile" used to define the reference plane was iteratively adjusted until the resulting maximum depth converged to the reference value of 25.25 mm.

This convergence occurred when 77.8% of the highest points (closely approximating the top 80th percentile) from the SimScan data were used to fit the reference plane. This calibrated SimScan model was then used as the ground truth for volume and area comparison.

The geometric features extracted by the proposed system were compared against the calibrated ground truth measurements. The results are summarized in Table 26. (Note: Units are assumed to be millimeters based on the depth).

Table 26 Comparison of Proposed System vs. Ground Truth

Geometric Feature	Proposed System	Ground Truth (SimScan42)	Relative Error
Volume (mm³)	188,560.76	188,275.63	0.15%
Proj. Area (mm²)	835.76	886.33	5.70%
Max. Depth (mm)	25.25	25.26	0.04%

The quantitative results validate the core hypothesis of this study: a low-cost, purely geometric stereo vision system can achieve a high degree of accuracy for pothole volume quantification. The relative volume error of 0.15% is exceptionally low and confirms that the SIFT-based reconstruction, when properly calibrated, is highly effective.

The slightly larger 5.70% error observed in the projected area is likely attributable to the differences in point cloud density between the two systems. The proposed system generates a sparser point cloud than the industrial-grade SimScan. Consequently, defining the exact pothole rim, which is crucial for the area calculation, requires more interpolation. The dense ground truth model can capture this boundary with higher fidelity, and this slight variation in the interpolated rim definition is the most probable source of discrepancy.

Conclusions and Recommendations

The feasibility and challenges of applying additive manufacturing, particularly 3D printing, for emergency pothole repair in concrete pavements was investigated. By integrating high-resolution laser scanning with SLA-based 3D printing, customized patch geometries were successfully generated from artificial pothole models. However, the process revealed several technical and practical barriers, including scanning efficiency under various environments, software compatibility issues, and the influence of complex surface geometries on fit accuracy. Surface grinding was found to improve geometric compatibility, yet its applicability in real-world practice requires careful evaluation due to the additional time and labor involved. While prefabricated repair components showed good fit with the smoothed pothole surfaces, unresolved challenges remain, particularly regarding the limited mechanical performance of printable materials and potential mismatch from pothole evolution over time.

To enable real-world implementation, further research is needed to address these limitations, such as the development of automated 3D geometry reconstruction methods using AI, exploration of in-situ 3D printing integrated with robotic construction systems, optimization of fast-curing repair materials compatible with printing processes, and long-term durability evaluation of printed patches. These efforts will be essential to support the practical deployment of 3D printing technologies in pavement maintenance.

Based on the experimental trials conducted in this study, several technical and practical challenges were identified in the application of 3D printing technology for pothole repair. These issues represent certain barriers to the broader adoption and field implementation of this approach. Broadly, the use of 3D printing in pothole repair can follow two primary strategies: (1) in-situ repair, and (2) prefabrication of repair materials. The in-situ 3D printing, although not explored in this study, requires a highly integrated system that can link surface scanning, geometry reconstruction, robotic printing, and on-site material curing. While this concept has shown early potential, few real-world implementations have been reported, primarily due to limitations in current robotic systems, printing hardware, and material technologies. Prefabricated repair material, which is the method investigated in this study, involves scanning the pothole geometry and printing customized repair components off-site. While this method simplifies on-site curing and installation, it introduces a different set of technical constraints:

1. Efficiency of scanning

   Laser scanning requires the placement of optical markers and typically takes several minutes to complete, depending on the pothole size and complexity. Accurate scans also necessitate cleaning the pothole surface, which can disrupt traffic and expose maintenance workers to potential hazards, especially on high-volume roadways. Environmental conditions such as precipitation or snow can also degrade scanning accuracy.

2. 3D modeling software compatibility

   Even when the scanned models appear accurate in the scanning software, minor geometric or mesh inconsistencies may arise when the model was imported to the printing software platforms. These compatibility issues require additional time to process the models for 3D printing.

3. Poor fit due to surface irregularities

   Due to the complex geometry of real-world potholes, which often have irregular angles, jagged edges, and rough surfaces, it is difficult for the printed repair pieces to achieve a perfect fit. Without post-processing such as grinding or surface smoothing, the printed materials are unlikely to well-fit the potholes in field. However, the in-situ grinding or surface smoothing of potholes will incur additional time and labor costs.

4. Limited material options for printing

   Current 3D printing systems are constrained to specific types of materials (e.g., all kinds of resin) that may not offer mechanical properties comparable to conventional pavement materials. This performance gap limits the applicability of 3D-printed solutions for high-traffic pavement repairs in the long-term.

5. Time lag between scanning and installation

   In the prefabrication approach, there is often a time delay between scanning the pothole and installing the printed repair component. During this period, the pothole may deteriorate further due to traffic loads and environmental exposure.

As a result, the pre-printed patch may no longer match the updated geometry, necessitating re-scanning or manual adjustment on site.

Given the challenges discussed above, further research is essential to support real-world implementation. First, more efficient and automated methods for 3D geometry reconstruction should be explored. Image-based reconstruction with artificial intelligence could offer a promising solution. Second, to minimize the time lag between scanning and installation, in-situ 3D printing techniques should be investigated, potentially in combination with robotic construction systems. In addition, the selection and optimization of fast-curing repair materials compatible with 3D printing processes require systematic investigation. Finally, the sealing and bonding agent between the pre-printed patch need be to ensure durability and reliable field performance. In the field, a standard square cut on the job site is usually conducted for concrete patches. Therefore, 3D printing is more suitable for the case of emergency repair.

In addition, a low-cost, vehicle-mountable 3D scanning system was developed for pavement pothole quantification. The system utilizes a calibrated three-camera rig and a purely geometric processing pipeline, avoiding the high costs associated with LiDAR and the data-dependency of deep learning models. The primary contribution is validation of this low-cost approach against a high-precision, industrial-grade 3D scanner. Experimental results on a sample pothole demonstrate that the proposed system can achieve exceptionally high accuracy. The volume estimation yielded a relative error of only 0.15% compared to the ground truth, confirming the system's capacity for precise geometric measurement.

While the low-cost image scanning in a controlled laboratory setting has been proved feasible, future work must address the challenges of real-world deployment. Future research will focus on 1) integrating the system into a vehicle to test its performance under dynamic (moving) conditions, 2) evaluating the system's robustness to varying environmental factors such as direct sunlight, shadows, and wet surfaces, and 3) optimizing the processing pipeline to achieve real-time (or near real-time) results suitable for rapid pavement assessment. This study demonstrates that a low-cost, stereo-vision-based geometric approach is a highly viable and practical alternative for automated pavement maintenance tasks.

REFERENCES

1. Elbatanouny, M.K. Hawkins, K.A., Abdelrahman, M.A., Lawler, J.S., Nelson, T.D., and Krauss, P.D. *Guide To Remediate Bridge Deck Cracking',* The Iowa Highway Research Board (TR-782) by Wiss, Janney, Elstner Associates, Inc. (2022)
2. ACI www.concrete.org/topicsinconcrete
3. Oman, M., 'Concrete Bridge Deck Cracks Sealant Evaluation and Implementation', Braun Intertec Corp, MnDOT, Research Report 2014.
4. Florida Department of Transportation. Accessed March 2024.https://www.fdot.gov/docs/default-source/programmanagement/Implemented/SpecBooks/2014/Files/400-114.pdf
5. Rettner, D.L., Fiegen, M.S., Snyder, M.B., MacDonald, K.A., *Analysis of Bridge* Deck Cracking Data: A Review of Mechanisms, Analysis of MnDOT Bridge Construction Data, and Recommendations for Treatment and Prevention, Minnesota Department of Transportation, St. Paul,MN.(2014)
6. Ni et al., 'Crack sealers for the preservation of concrete bridge decks: a synthesis of a national survey and literature review', Journal of Infrastructure Preservation and Resilience, (2023) https://doi.org/10.1186/s43065-023-00091-8
7. Johnson, K. A., *Crack and Concrete Deck Performance*, MS Thesis, University of Minnesota (2013)
8. NJDOT *Standard Specifications for Road and Bridge Construction,* New Jersey Department of Transportation, Trenton, NJ.(2019)
9. NYSDOT *Crack Sealing by Epoxy Injection*, New York State Department of Transportation, Special Specifications Part 8.(1999)
10. Issa, M. et al*., Concrete Bridge Deck Crack Sealing*, IDOT, FHWA-ICT-2024-007. (2024)
11. AASHTO Manual for Bridge Element Inspection (MBEI), second edition (2019).
12. NJ Turn Pike Authority, Standard Specifications, 7th edition, 2016.
13. ACI 224.1R-93 *Causes, Evaluation and Repair of Cracks in Concrete Structures*, American Concrete Institute (1998)
14. Tecvac, Inc,, https://www.tecvacinc.net/untitled-sitepage_9
15. Balfour Beatty, Inc. https://www.balfourbeatty.com/what-we-do/expertise/specialist-services/specialist-structural-repair-and-maintenance/
16. ASTM D4541-17, Standard Test Method for Pull-Off Strength of Coatings Using Portable Adhesion Testers. ASTM D4541-17
17. British Standards Institution. (1986). *BS 1881: Part 203 - Recommendations for measurement of velocity of ultrasonic pulses in concrete*.
18. Bungey, J. H., & Grantham, M. G. (2006). *Testing of concrete in structures*. CRC Press.
19. Pinto, R. C., Medeiros, A., Padaratz, I. J., et al. (2010). Use of ultrasound to estimate depth of surface opening cracks in concrete structures. *e-Journal of Nondestructive Testing and Ultrasonics, 8*, 1–11.
    Shin, S. W., Zhu, J., Min, J., et al. (2008). Crack depth estimation in concrete using energy transmission of surface waves. *ACI Materials Journal, 105*(5), 510.
20. Hevin, G., Abraham, O., Pedersen, H., et al. (1998). Characterization of surface cracks with Rayleigh waves: A numerical model. *NDT & E International, 31*(4), 289–297.

21. Ahn, E., Kim, H., Sim, S.-H., et al. (2018). Surface-wave-based model for estimation of discontinuity depth in concrete. *Sensors, 18*(9), 2793.
22. Kee, S.-H., Fernández-Gómez, E., & Zhu, J. (2011). Evaluating surface-breaking cracks in concrete using air-coupled sensors. *ACI Materials Journal, 108*(5), 558.
23. Matsuyama, K., Yamada, M., & Ohtsu, M. (2010). On-site measurement of delamination and surface crack in concrete structure by visualized NDT. *Construction and Building Materials, 24*(12), 2381–2387.
24. Payan, C., Quiviger, A., Garnier, V., et al. (2013). Applying diffuse ultrasound under dynamic loading to improve closed crack characterization in concrete. *The Journal of the Acoustical Society of America, 134*(2), EL211–EL216.
25. Anugonda, P., Wiehn, J. S., & Turner, J. A. (2001). Diffusion of ultrasound in concrete. *Ultrasonics, 39*(6), 429–435.
26. Quiviger, A., Payan, C., Chaix, J.-F., et al. (2012). Effect of the presence and size of a real macro-crack on diffuse ultrasound in concrete. *NDT & E International, 45*(1), 128–132.
27. Quiviger, A., Payan, C., Chaix, J.-F., et al. (2012). Macro-crack characterization in concrete by diffuse ultrasound under low-frequency dynamic loading. In *Proceedings of Meetings on Acoustics*. AIP Publishing.
28. Ramamoorthy, S. K., Kane, Y., & Turner, J. A. (2004). Ultrasound diffusion for crack depth determination in concrete. *The Journal of the Acoustical Society of America, 115*(2), 523–529.
29. Kaur, N. P., Shah, J. K., Majhi, S., et al. (2019). Healing and simultaneous ultrasonic monitoring of cracks in concrete. *Materials Today Communications, 18*, 87–99.
30. Kaur, N. P., Majhi, S., Dhami, N. K., et al. (2020). Healing fine cracks in concrete with bacterial cement for an advanced non-destructive monitoring. *Construction and Building Materials, 242*, 118151.
31. Schickert, M. (2005). Progress in ultrasonic imaging of concrete. *Materials and Structures, 38*, 807–815.
32. Shah, J. K., Majhi, S., & Mukherjee, A. (2018). Ultrasonic-based crack imaging in concrete. In *Proceedings of the 11th International Conference on Structural Integrity and Failure*.
33. In, C. W., Kim, J.-Y., Jacobs, L. L., et al. (2012). Crack depth measurement in concrete using diffuse ultrasound. In *AIP Conference Proceedings*. American Institute of Physics.
34. Cowan, M. L., Beaty, K., Page, J. H., et al. (1998). Group velocity of acoustic waves in strongly scattering media: Dependence on the volume fraction of scatterers. *Physical Review E, 58*(5), 6626.
35. Lin, S., & Wang, Y. (2020). Crack-depth estimation in concrete elements using ultrasonic shear-horizontal waves. *Journal of Performance of Constructed Facilities, 34*(4), 04020064.
36. Chang, Y.-F., & Wang, C.-Y. (1997). A 3-D image detection method of a surface opening crack in concrete using ultrasonic transducer arrays. *Journal of Nondestructive Evaluation, 16*, 193–203.

37. Kimoto, K., Ueno, S., & Hirose, S. (2006). Image-based sizing of surface-breaking cracks by SH-wave array ultrasonic testing. *Ultrasonics, 45*(1–4), 152–164.
38. Kuchipudi, S. T., Pudovikov, S., Wiggenhauser, H., et al. (2023). Imaging of vertical surface-breaking cracks in concrete members using ultrasonic shear wave tomography. *Scientific Reports, 13*(1), 21744.
39. Saini, A., Felice, M. V., Fan, Z., et al. (2020). Optimisation of the half-skip total focusing method (HSTFM) parameters for sizing surface-breaking cracks. *NDT & E International, 116*, 102365.
40. Ohtsu, M., & Watanabe, T. (2002). Stack imaging of spectral amplitudes based on impact-echo for flaw detection. *NDT & E International, 35*(3), 189–196.
41. Watanabe, T., Morita, T., Hashimoto, C., et al. (2004). Detecting voids in reinforced concrete slab by SIBIE. *Construction and Building Materials, 18*(3), 225–231.
42. Chen, X., Wang, H., & Venkiteela, G. (2023). Asphalt pavement pothole repair using the pre-heating method: An integrated experiment and modeling study. *Transportation Research Record, 2677*(11), 1–12.
43. Federal Highway Administration. (2009). *TechBrief: Concrete pavement rehabilitation—Guide for partial-depth repairs*. U.S. Department of Transportation. https://www.fhwa.dot.gov/pavement/concrete/repair09.cfm
44. National Concrete Consortium. (2021). *NCC Spring 2021 state reports on fast-setting patching materials* [Report]. National Concrete Consortium.
45. Blaha, J. R. (1993). *Fabrication and testing of automated pothole patching machine* (No. SHRP-H-674). Strategic Highway Research Program, National Research Council.
46. Peiris, A., & Harik, I. E. (2022). *Rapid pothole repair in concrete bridge decks* (No. KTC-23-02/SPR21-607-1F). Kentucky Transportation Cabinet.
47. Delatte, N., Weiss, W. J., & Taylor, P. (2023). *Optimizing concrete pavement opening to traffic*.
48. Yang, Z., Brown, H., Huddleston, J., & Seger, W. (2016). Performance evaluation of rapid-set prepackaged cementitious materials for rehabilitation of surface distress of concrete transportation structures. *PCI Journal, 61*(2).
49. Gholami, S., Hu, J., & Kim, Y. R. (2019). *Development of high-performance rapid patching materials for pavement repair* (No. SPR-P1 (18) M 071). Nebraska Department of Transportation.
50. Sprinkle, M. (2009). *Rapid repair materials and construction* [Report]. Virginia Transportation Research Council.
51. Gong, F., Cheng, X., Fang, B., Cheng, C., Liu, Y., & You, Z. (2023a). Prospect of 3D printing technologies in maintenance of asphalt pavement cracks and potholes. *Journal of Cleaner Production, 397*, 136551.
52. Jackson, R. J., Wojcik, A., & Miodownik, M. (2018). 3D printing of asphalt and its effect on mechanical properties. *Materials & Design, 160*, 468–474.
53. Liu, J., Yang, X., Wang, X., & Yam, J. W. (2022). A laboratory prototype of automatic pavement crack sealing based on a modified 3D printer. *International Journal of Pavement Engineering, 23*(9), 2969–2980.

54. Phan, T. M., Kim, J. H., Kim, H. J., & Park, D. W. (2024). Automated repair of asphalt pavement cracks and potholes utilizing 3D printing and LiDAR scanning. *Construction and Building Materials, 450*, 138748.
55. Gong, F., Cheng, X., Wang, Q., Chen, Y., You, Z., & Liu, Y. (2023b). A review on the application of 3D printing technology in pavement maintenance. *Sustainability, 15*(7), 6237.
56. Gong, F., Cheng, X., Chen, Y., Liu, Y., & You, Z. (2022). 3D-printed rubber-modified asphalt as sustainable material in pavement maintenance. *Construction and Building Materials, 354*, 129160.
57. World Highways. (2019). *Researchers trial 3D printing for both concrete and asphalt roads*. https://www.worldhighways.com/wh6/feature/researchers-trial-3d-printing-both-concrete-and-asphalt-roads
58. Yeon, J., Kang, J., & Yan, W. (2018). Spall damage repair using 3D printing technology. *Automation in Construction, 89*, 266–274.
59. Akagic, A., Buza, E., & Omanovic, S. (2017). Pothole detection: An efficient vision-based method using RGB color-space image segmentation. In *2017 40th International Convention on Information and Communication Technology, Electronics and Microelectronics (MIPRO)* (pp. 1104–1109).
60. De Blasiis, M. R., Di Benedetto, A., & Fiani, M. (2020). Mobile laser scanning data for the evaluation of pavement surface distress. *Remote Sensing, 12*(6), 942.
61. Dong, Q., Huang, B., & Zhao, S. (2014). Field and laboratory evaluation of winter season pavement pothole patching materials. *International Journal of Pavement Engineering, 15*(4), 279–289.
62. Feng, Z., El Issaoui, A., Lehtomäki, M., Ingman, M., Kaartinen, H., Kukko, A., Savela, J., Hyyppä, H., & Hyyppä, J. (2022). Pavement distress detection using terrestrial laser scanning point clouds: Accuracy evaluation and algorithm comparison. *ISPRS Open Journal of Photogrammetry and Remote Sensing, 3*, 100010.
63. Gao, M., Wang, X., Zhu, S., & Guan, P. (2020). Detection and segmentation of cement concrete pavement pothole based on image processing technology. *Mathematical Problems in Engineering, 2020*, 1360832.
64. Guan, J., Yang, X., Ding, L., Cheng, X., Lee, V. C. S., & Jin, C. (2021). Automated pixel-level pavement distress detection based on stereo vision and deep learning. *Automation in Construction, 129*, 103788.
65. Jahanshahi, M. R., Jazizadeh, F., Masri, S. F., & Becerik-Gerber, B. (2013). Unsupervised approach for autonomous pavement-defect detection and quantification using an inexpensive depth sensor. *Journal of Computing in Civil Engineering, 27*(6), 743–754.
66. Koch, C., & Brilakis, I. (2011). Pothole detection in asphalt pavement images. *Advanced Engineering Informatics, 25*(3), 507–515.
67. Lin, J., & Liu, Y. (2010). Potholes detection based on SVM in the pavement distress image. In *2010 Ninth International Symposium on Distributed Computing and Applications to Business, Engineering and Science* (pp. 544–547).
68. Lowe, G. (2004). SIFT—The scale invariant feature transform. *International Journal of Computer Vision, 2*, 91–110.

69. Mathavan, S., Kamal, K., & Rahman, M. (2015). A review of three-dimensional imaging technologies for pavement distress detection and measurements. *IEEE Transactions on Intelligent Transportation Systems, 16*(5), 2353–2362.
70. Moazzam, I., Kamal, K., Mathavan, S., Usman, S., & Rahman, M. (2013). Metrology and visualization of potholes using the Microsoft Kinect sensor. In *2013 16th International IEEE Conference on Intelligent Transportation Systems (ITSC)* (pp. 1284–1291).
71. Nienaber, S., Booysen, M. J., & Kroon, R. S. (2015). Detecting potholes using simple image processing techniques and real-world footage. In *34th Annual Southern African Transport Conference (SATC 2015)* (pp. 153–164).
72. Pan, Z., Guan, J., Yang, X., Guo, A., & Wang, X. (2024). 3D profile-based pothole segmentation and quantification. *International Journal of Hydromechatronics, 7*(1), 16–30.
73. Roberts, R., Inzerillo, L., & Di Mino, G. (2020). Exploiting low-cost 3D imagery for the purposes of detecting and analyzing pavement distresses. *Infrastructures, 5*(1), 6.
74. Saad, A. M., & Tahar, K. N. (2019). Identification of rut and pothole by using multirotor unmanned aerial vehicle (UAV). *Measurement, 137*, 647–654.
75. Tan, Y., & Li, Y. (2019). UAV photogrammetry-based 3D road distress detection. *ISPRS International Journal of Geo-Information, 8*(9), 409.
76. Tedeschi, A., & Benedetto, F. (2017). A real-time automatic pavement crack and pothole recognition system for mobile Android-based devices. *Advanced Engineering Informatics, 32*, 11–25.
77. Ullman, S. (1979). The interpretation of structure from motion. *Proceedings of the Royal Society of London. Series B, Biological Sciences, 203*(1153), 405–426.